INSTITUTO
UNIVERSITÁRIO
DE LISBOA

Reconfigurable Intelligent Surfaces based System Design for Future 6G Wireless Networks

Ana Rita Betencourt da Costa Rodrigues dos Santos

Master in Telecommunications and Computer Engineering

Supervisor:
Phd, Nuno Manuel Branco Souto, Associate Professor
Iscte - Instituto Universitário de Lisboa

Co-Supervisor:
Phd, Marco Alexandre dos Santos Ribeiro, Assistant Professor
Iscte - Instituto Universitário de Lisboa

November, 2022

TECNOLOGIAS
E ARQUITETURA

Department of Information Science and Technology

Reconfigurable Intelligent Surfaces based System Design for Future 6G Wireless Networks

Ana Rita Betencourt da Costa Rodrigues dos Santos

Master in Telecommunications and Computer Engineering

Supervisor:
Phd, Nuno Manuel Branco Souto, Associate Professor
Iscte - Instituto Universitário de Lisboa

Co-Supervisor:
Phd, Marco Alexandre dos Santos Ribeiro, Assistant Professor
Iscte - Instituto Universitário de Lisboa

Acknowledgment

In this section I would like to express my deepest gratitude to everyone who contributed to the making of this dissertation.

I would like to convey my utmost gratitude to my supervisor and co-supervisor, Professor Nuno Souto and Professor Marco Ribeiro for their constant assistance, orientation, tolerance and expertise that made this research project come to fruition.

I would like to acknowledge and thank Iscte-Instituto Universitário de Lisboa for all of the knowledge and expertise that was provided throughout my academic education. I would also like to extend my deep gratitude to all the staff, professors and colleagues who were always there and willing to help.

Special thanks to the Instituto de Telecomunicações (IT) for providing support and all the tools to execute this work.

Finally, I would like to express thankfulness towards my family and friends for their continued support, encouragement and friendship over the course of this project.

Resumo

As futuras redes sem fios da sexta geração (6G) consideram a frequência Terahertz fundamental para suportar o elevado número de tráfego gerado na rede, permitindo assim elevadas taxas de transmissão de dados. Todavia, o comportamento do espectro de frequências THz condiciona a propagação que ocorre no sistema de comunicação pela sua elevada atenuação, originando graves perdas de propagação.

Superfícies inteligentes reconfiguráveis (RIS) são uma tecnologia promissora para ultrapassar as limitações existentes na faixa dos THz ao moldarem a direção da onda, permitindo que o sinal se propague para o destinatário. Os RIS dispõem de inúmeras aplicações nos sistemas sem fios, especificamente na otimização do desempenho da rede de comunicações ao utilizarem antenas ultra massivas de múltipla entradas e saídas. Os sistemas UM-MIMO são fundamentais para implementar frequências THz pelo elevado número de antenas, facilitando a propagação de dados desde o emissor e recetor. A fim de alcançar uma complexidade reduzida nos sistemas UM-MIMO, é necessário implementar pré-codificadores híbridos.

Esta dissertação pretende conceber um sistema de comunicação para redes sem fios ultra massivo MIMO assistido por RIS para melhorar a eficiência energética das comunicações 6G e do espectro e o alcance da cobertura. De modo a maximizar a taxa alcançável do modelo, será desenvolvido um algoritmo para calcular a quantização das mudanças de fase dos elementos RIS sendo implementado várias estruturas híbridas de pré-codificação.

Os resultados numéricos serão analisados a fim de revelar qual a configuração ideal para o sistema de comunicação THz assistido por RIS mediante as taxas alcançáveis obtidas.

Palavras-chave: 6G; comunicações Terahertz (THz); modelação de canais; superfícies inteligentes reconfiguráveis (RIS); taxa alcançável; ultra-massivo múltiplas-entradas múltiplas-saídas (UM-MIMO).

Abstract

Future sixth generation (6G) wireless networks perceive the THz band as essential to support the high volume of wireless traffic data being generated in the network, thus enabling ultra high transmission rates. However, the behaviour of the THz frequency spectrum affects the propagation occurring in the wireless communication system due to high attenuation, leading to severe propagation losses.

Reconfigurable intelligent surfaces (RIS) are a promising technology to overcome the limitations present in the THz waveband by reshaping the wave direction, thus enabling the signal to propagate towards its intended target. RIS have many applications in wireless systems, specifically in the optimization of the communication network performance when combined with ultra-massive multiple-input multiple-output antennas (UM-MIMO). UM-MIMO systems are critical for implementing THz frequencies as the large number of antennas provides high directivity pencil like beams, thereby enabling easy data spread from the transmitter towards the receiver. To achieve low complexity whilst deploying UM-MIMO systems, hybrid precoders must be implemented.

This dissertation aims to design and evaluate a RIS-assisted communication model for ultra-massive MIMO systems to extend coverage range and to improve the energy and spectral efficiency of 6G communications. To maximize the achievable rate of the structure, an algorithm will be developed to calculate the phase shifts of the individual RIS elements, and the implementation of various hybrid precoding structures.

Several numerical results will be obtained through various simulations and analysed to give insight into which design is best suited for RIS-assisted THz communication system through the achievable rates obtained.

Keywords: 6G; Terahertz (THz) communications; channel modeling; reconfigurable intelligent surfaces (RIS); achievable rate; ultra-massive multiple-input multiple-output (UM-MIMO).

Contents

Acknowledgment iii

Resumo v

Abstract vii

List of Figures xiii

List of Acronyms xvii

Chapter 1. Introduction 1
1.1. Motivation and Context 1
1.2. Research Questions 1
1.3. Goals 1
1.4. Design Science Research 2
1.5. Structure 2
1.6. Contributions 3
1.7. Notation 3

Chapter 2. Literature Review 5
2.1. 6G Wireless Networks 5
2.2. Millimeter Wave 6
2.3. Terahertz Communications 6
2.3.1. THz Channel Behaviour 6
2.4. HyperSurfaces 7
2.4.1. Metasurfaces 7
2.5. Reconfigurable Intelligent Surfaces 8
2.5.1. RIS Structure 9
2.6. MIMO 10
2.6.1. UM-MIMO 10
2.6.2. THz UM-MIMO System 10
2.7. Beamforming 11
2.7.1. Digital Beamforming Architecture 12
2.7.2. Analog Beamforming Architecture 12
2.7.3. Hybrid Beamforming Architecture 12
2.7.4. Hybrid Beamforming Scheme for RIS 13

Chapter 3. Hybrid Precoder and RIS Optimization 15

3.1. Channel Modeling 15
3.2. Channel Modeling for RIS Systems 16
3.2.1. Indirect Link Channel Matrix 17
3.2.2. Direct Link Channel Matrix 19
3.3. System Model 19
3.3.1. Hybrid precoder 20
3.4. Analog Precoder 24
3.4.1. Fully and Partially Connected Hybrid Design 24
3.4.2. Unquantized Phase Shifters (UPS) 25
3.4.3. Quantized Phase Shifters (QPS) 25
3.4.4. Double Phase Shifters (DPS) 25
3.4.5. Switches 25
3.4.6. Antenna Selection 26
3.4.7. Array of Subarrays (AoSA) 26
3.4.8. Dynamic Array of Subarrays (DAoSA) 27

Chapter 4. Analysis and Discussion of Results 29
4.1. Simulator 29
4.2. Study of Achievable Rate with variable Distance for 28 GHz 29
4.2.1. Hybrid Precoders 31
4.2.2. Dynamic Array of Subarray 33
4.3. Study of Achievable Rate with variable Transmitter Power for 28 GHz 37
4.3.1. Direct + RIS link activated 41
4.4. Study of Achievable Rate with variable Distance for 300 GHz 43
4.4.1. Phase Shifters - RIS Quantization Bits: 45
4.4.2. Phase Shifter - Precoder Quantization Bits: 46
4.4.3. Switches 46
4.4.4. Antenna Selection 48
4.4.5. Dynamic Array of Subarrays 49
4.4.6. All Hybrid architectures 51

Chapter 5. Conclusion and Future Works 55
5.1. Conclusion 55
5.2. Future Work 56

Bibliography 59

Appendix A. Article: Hybrid Precoder Algorithm Optimization in Reconfigurable Intelligent Surface-Assisted THz Ultra Massive MIMO Systems 63

Appendix B. 28 GHz Scenario 81
B.1. Simple Reflectarray 81
B.2. Hybrid Precoder - Phase Shifter 81

B.3. Hybrid Precoder - DAoSA 84
B.4. Hybrid Architectures - Only RIS activated 84

Appendix C. Transmitter Power 87
C.1. Unquantized Phase Shifter 87
C.2. Free Dynamic Array of Subarrays 88

Appendix D. 300 GHz Scenario 91
D.1. Simple Reflectarrays 91
D.2. AM-APG 91
D.3. Hybrid Achitectures 92
D.3.1. Switches 92
D.3.2. Antenna Selection 93

List of Figures

Figure 2.1 Electromagnetic spectrum for the mmWave and THz region 6
Figure 2.2 Incident radio wave at an angle θ_i with a rough surface creates a reflected wave, θ_r reflected angle, and a scattered wave with a θ_s angle. 7
Figure 2.3 Example of a RIS application in a wireless environment with the LoS between the BS and the user obstructed 8
Figure 2.4 RIS architecture - RIS with N elements and a controller 9
Figure 2.5 UM-MIMO System Scheme 11
Figure 2.6 Hybrid Beamforming scheme 12

Figure 3.1 RIS-assisted communications with LoS and NLoS links between base station and user. 16
Figure 3.2 General architecture of a hybrid precoder. 19
Figure 3.3 General architecture of a hybrid combiner. 20
Figure 3.4 Hybrid Designs: Fully Connected structure 3.4a and Partially Connected structure 3.4b 24
Figure 3.5 Double Phase Shifter configuration 25
Figure 3.6 Structure employing switches 26
Figure 3.7 Antenna Selection scheme 26
Figure 3.8 AoSA Hybrid Designs: (3.8a) Switches, (3.8b) Antenna Selection 27
Figure 3.9 Hybrid architecture dynamic array of subarrays based on phase shifters 27

Figure 4.1 Study of Achievable rate (Gbps) using simple reflectarrays and AM-APG for $N_{RIS} = 256$, whilst increasing the distance between Tx and Rx. 30
Figure 4.2 Study of Achievable rate (Gbps) for different hybrid precoders for $N_{RIS} = 256$, direct + RIS link in use. 32
Figure 4.3 Study of Achievable rate (Gbps) for different fully connected hybrid precoders for $N_{RIS} = 256$, with only RIS link in use. 32
Figure 4.4 Study of Achievable rate (Gbps) for different partially connected hybrid precoders for $N_{RIS} = 256$, with only RIS link in use. 33
Figure 4.5 Study of Achievable rate (Gbps) for free dynamic AoSA using different RIS elements, with only RIS link in use. 34
Figure 4.6 Study of Achievable rate (Gbps) for free dynamic AoSA using different Tx and Rx antennas for $N_{RIS} = 144$, with only RIS link in use. 35
Figure 4.7 Study of Achievable rate (Gbps) for free dynamic AoSA using different Tx and Rx antennas for $N_{RIS} = 256$, with only RIS link in use. 35

Figure 4.8 Study of Achievable rate (Gbps) for free dynamic AoSA using different Tx and Rx antennas for $N_{RIS} = 144$, with both the RIS and direct link in use. 36
Figure 4.9 Study of Achievable rate (Gbps) for free dynamic AoSA using different Tx and Rx antennas for $N_{RIS} = 144$, and for different links in use..... 37
Figure 4.10 Study of Achievable rate (Gbps) for Unquantized Phase Shifters fully connected whilst increasing the transmitter power between Tx and Rx, for Tx-Rx=10 m and RIS 1 m from Tx, only RIS link in use..... 38
Figure 4.11 Study of Achievable rate (Gbps) for free dynamic AoSA whilst increasing the transmitter power between Tx and Rx, for Tx-Rx=10 m and RIS 1 m from Tx, only RIS link in use..... 38
Figure 4.12 Study of Achievable rate (Gbps) for Unquantized Phase Shifters whilst increasing the transmitter power between Tx and Rx, for Tx-Rx=10 m and RIS 5 m from Tx, only the RIS link activated. 39
Figure 4.13 Study of Achievable rate (Gbps) for free dynamic AoSA whilst increasing the transmitter power between Tx and Rx, for Tx-Rx=10 m and RIS 5 m from Tx, only the RIS link activated. 39
Figure 4.14 Study of Achievable rate (Gbps) for Unquantized Phase Shifters fully connected, for Tx-Rx=10 m and RIS 1 meter from Rx, only the RIS link activated. 40
Figure 4.15 Study of Achievable rate (Gbps) for free dynamic AoSA for Tx-Rx=10 m and RIS 1 meter from Rx, only the RIS link activated. 40
Figure 4.16 Study of Achievable rate (Gbps) for Unquantized Phase Shifters fully connected, for Tx-Rx=10 m and RIS 1 m from Tx, comparing only RIS link and direct + RIS link. 42
Figure 4.17 Study of Achievable rate (Gbps) for free dynamic AoSA using 1 subarray per RF chain, for Tx-Rx=10 m and RIS 1 m from Tx, comparing only RIS link with direct + RIS link. 42
Figure 4.18 Study of Achievable rate (Gbps) for free dynamic AoSA using 2 subarrays per RF chain, whilst increasing the transmitter power between Tx and Rx, for Tx-Rx=10 and RIS 1 m from Tx, comparing direct and direct + RIS link. 43
Figure 4.19 Achievable rate versus distance between Transmitter and Receiver for APG, AM-APG and Static Reflectarray algorithms. 44
Figure 4.20 Achievable rate vs distance between Tx-Rx for fully connected precoders using quantized phase shifters, in comparison with UPS, using $N_{RIS} = 512$. 45
Figure 4.21 Achievable rate vs distance between Tx-Rx for partially connected precoders using quantized phase shifters, in comparison with UPS, considering $N_{RIS} = 512$. 46

Figure 4.22 Achievable rate versus distance between Tx-Rx for fully connected quantized RF precoders, in comparison with unquantized phase shifter, considering $N_{RIS} = 512$. 47
Figure 4.23 Achievable rate versus distance between Tx-Rx for partially connected quantized RF precoders, in comparison with unquantized phase shifter, considering $N_{RIS} = 512$. 47
Figure 4.24 Study of Achievable rate (Gbps) comparing fully and partially connected switches, for different RIS elements whilst increasing the distance between Tx-Rx. 48
Figure 4.25 Study of Achievable rate (Gbps) using antenna selection fully connected for hybrid beamforming architecture, for different RIS elements whilst increasing the distance between Tx and Rx. 49
Figure 4.26 Study of Achievable rate (Gbps) comparing fully and partially connected antenna selection for hybrid beamforming architecture, for different RIS elements whilst increasing the distance between Tx and Rx. 50
Figure 4.27 Study of Achievable rate (Gbps) using adjacent dynamic array of subarrays for hybrid beamforming architecture, with different number of subarrays per RF chain, as well as single or double phase shifter whilst increasing the distance between Tx and Rx. 50
Figure 4.28 Study of Achievable rate (Gbps) using free dynamic array of subarrays with different number of subarrays per RF chain, as well as SPS or DPS, whilst increasing the distance between Tx and Rx. 51
Figure 4.29 Study of Achievable rate (Gbps) using dynamic AoSA architecture with different number of subarrays per RF chain, whilst increasing the distance between Tx and Rx. 52
Figure 4.30 Study of Achievable rate (Gbps) on all fully connected hybrid designs with $N_{RIS} = 512$, whilst increasing the distance between Tx and Rx. 52
Figure 4.31 Study of Achievable rate (Gbps) for partially connected hybrid designs with $N_{RIS} = 512$, whilst increasing the distance between Tx-Rx. 53

Figure B.1 Study of Achievable rate (Gbps) using simple reflectarrays for $N_{RIS} = 256$, whilst increasing the distance between Tx and Rx. 81
Figure B.2 Study of Achievable rate (Gbps) for different RIS elements using unquantized phase shifters partially connected, whilst increasing the distance between Tx and Rx,with RIS and direct link in use. 82
Figure B.3 Study of Achievable rate (Gbps) for different RIS elements comparing unquantized phase shifters partially and fully connected, whilst increasing the distance between Tx and Rx, with RIS and direct link in use. 82
Figure B.4 Study of Achievable rate (Gbps) for unquantized phase shifters partially and fully connected with $N_{RIS} = 256$, whilst increasing the distance between Tx and Rx. 83

Figure B.5 Study of Achievable rate (Gbps) for quantized phase shifters partially and fully connected with $N_{RIS} = 256$, whilst increasing the distance between Tx and Rx. 83
Figure B.6 Study of Achievable rate (Gbps) for adjacent dynamic array of sub-arrays for $N_{RIS} = 512$, whilst increasing the distance between Tx and Rx. 84
Figure B.7 Study of Achievable rate (Gbps) for different hybrid precoders for $N_{RIS} = 256$, whilst increasing the distance between Tx and Rx, with only RIS link in use. 85

Figure C.1 Study of Achievable rate (Gbps) for Unquantized Phase Shifters fully connected, whilst increasing the transmitter power between Tx and Rx, for Tx-Rx=10 m and RIS 5 meters from Tx, direct + RIS link activated. 87
Figure C.2 Study of Achievable rate (Gbps) for Unquantized Phase Shifters fully connected, whilst increasing the transmitter power between Tx and Rx, for Tx-Rx=10 m and RIS 1 meter from Rx, direct + RIS link activated. 88
Figure C.3 Study of Achievable rate (Gbps) for free dynamic AoSA with 1 sub-aray per RF chain whilst increasing the transmitter power between Tx and Rx, for Tx-Rx=10 m and RIS 5 meters from Tx, direct + RIS link activated. 88
Figure C.4 Study of Achievable rate (Gbps) for free dynamic AoSA with 2 sub-arrays per RF chain whilst increasing the transmitter power between Tx and Rx, for Tx-Rx=10 m and RIS 5 meters from Tx, direct + RIS link activated. 89

Figure D.1 Achievable rate (Gbps) vs distance between Tx-Rx using Simple Reflectors for different RIS elements. 91
Figure D.2 Study of Achievable rate (Gbps) for fully digital RIS algorithm, AM-APG, for different RIS elements whilst increasing the distance between Tx and Rx. 92
Figure D.3 Study of Achievable rate (Gbps) using fully connected switches, for different RIS elements whilst increasing the distance between Tx and Rx. 92
Figure D.4 Study of Achievable rate (Gbps) using partially connected switches, for different RIS elements whilst increasing the distance between Tx and Rx. 93
Figure D.5 Study of Achievable rate (Gbps) using antenna selection partially connected, for different RIS elements whilst increasing the distance between Tx and Rx. 93

List of Acronyms

- **5G** Fifth Generation
- **6G** Sixth Generation
- **ADC** Analog-to-Digital Conversion
- **AM** Alternated Minimization
- **AM-APG** Alternating Minimization Accelerated Proximal Gradient
- **APG** Accelerated Proximal Gradient
- **AoA** Angle of Arrival
- **AoD** Angle of Departure
- **AoSA** Array of Subarray
- **BB** Baseband
- **BF** Beamforming
- **BS** Base Station
- **DAC** Digital-to-Analog Conversion
- **DAoSA** Dynamic Array of Subarray
- **DCS** Digitally Controllable Scatterers
- **DPS** Double Phase Shifter
- **EM** Electromagnetic
- **FC** Fully Connected
- **GHz** Gigahertz
- **Gbps** Gigabits per Second
- **HBF** Hybrid Beamforming
- **IID** Independent and Identically Distributed
- **LIS** Large Intelligent Surfaces
- **LoS** Line-of-Sight
- **MIMO** Multiple-Input Multiple-Output
- **NLoS** Non-Line-of-Sight
- **PC** Partially Connected
- **PL** Path Loss
- **PLE** Path Loss Exponent
- **PSK** Phase-Shift Keying
- **QAM** Quadrature Amplitude Modulation
- **QPS** Quantized Phase Shifter
- **RF** Radio Frequency
- **RIS** Reconfigurable Intelligent Surface

- **Rx** Receiver
- **SCS** Software Controllable Surface
- **SM** Spatial Multiplexing
- **SNR** Signal-to-Noise Ratio
- **SPS** Single Phase Shifter
- **SRE** Smart Radio Environment
- **SVD** Singular Value Decomposition
- **THz** Terahertz
- **Tbps** Terabits per Second
- **Tx** Transmitter
- **UE** User Equipment
- **ULA** Uniform Linear Array
- **UM-MIMO** Ultra-Massive Multiple-Input Multiple-Output
- **UPA** Uniform Planar Array
- **UPS** Unquantized Phase Shifter
- **XR** Extended Reality
- **mmWave** Millimeter-Wave

CHAPTER 1

Introduction

1.1. Motivation and Context

The evolution of wireless communications in the past years led to an enormous increase in the number of data rates consumed globally to be able to support the ever-growing number of interconnected devices as well as create solutions to support future wireless communications.

Millimeter-wave (mmWave) communications (30-300 GHz) have been incorporated into 5G systems. However, the total bandwidth available in mmWave communications is less than 10 GHz, thus insufficient for higher Tbps data rates. Terahertz frequency band (0.1-10 THz) is considered a key wireless technology for the sixth generation (6G) through its ability on improving high-speed transmissions by reducing latency in future wireless applications so that communications at a Tbps rate is achievable [**1**].

Reconfigurable Intelligent Surfaces (RIS) are seen as a promising technology for THz systems for their ability to be programmable, being able to change an impinging electromagnetic (EM) wave and redirect it towards the desired user, without requiring a power amplifier, Radio Frequency (RF) chain, or sophisticated signal processing [**2**].

To combat the severe limitation of signal transmission distance and coverage provided for the Terahertz frequency band, Reconfigurable Intelligent Surfaces are seen as a solution towards creating a smart wireless communication environment based on software-controlled metasurfaces that are deployed in the wireless communications to shape the incoming radio waves and forward the incoming signal toward the end users.

The implementation of RIS facilitates the creation of a smart radio environment (SRE) by controlling the signal propagation properties as a means to improve its performance by guaranteeing signal reception [**3**].

1.2. Research Questions

Regarding the theme of this paper, the main research questions that will be studied and analysed are:

- How can RIS overcome the severe distance limitation in THz band?
- What are the beamforming architectures that can be implemented and which one is the most suitable towards a THz RIS scheme?

1.3. Goals

This dissertation will focus on the design of an efficient and effective smart wireless communication environment using reconfigurable intelligent surfaces (RIS) through the

optimization of the individual RIS elements and transceivers in order to combat the severe distance limitation in the Terahertz band. Accordingly, the main objectives to be studied are the usage of large antennas at the transmitter and receiver in combination with RIS, implementation of hybrid schemes at the transmitter in order to reduce its complexity, and the implementation of an algorithm for optimal design of the precoder and the RIS simultaneously.

A physical layer simulator will be developed using Matlab in order to incorporate the RIS based solutions with adequate THz hardware/channel models for different UM-MIMO hybrid architectures.

Through simulations, the performance of the environment-aware communication system based on RIS for the THz channel will then be evaluated and discussed.

1.4. Design Science Research

The dissertation will follow the main steps of the Design Science Research methodology to achieve all the goals defined for this dissertation:

Identify Problem: The main problem outlined in this project are the limitations found on the THz band.

Define Objectives: Study Reconfigurable Intelligent Surfaces and different hybrid architectures to overcome the distance limitations in THz band.

Design and Development: It will be designed and implemented in a physical layer simulator a realistic THz UM-MIMO model and it will be developed a RIS based solution using hybrid precoders to solve the problem found on the THz channel.

Demonstration: The results will be obtained in the simulation created on Matlab.

Evaluation: The final data gathered in the designed system will be evaluated by comparing the impact of the RIS and the hybrid precoder against existing results found in the literature in order to obtain a conclusion on the most efficient and effective model to be used in the THz band.

Communication: The solutions implemented and studied along the making of this thesis will be presented in the final dissertation paper.

1.5. Structure

This dissertation is divided into five chapters. The first chapter introduces the theme of the dissertation by outlining its context and motivations as well as the main research questions that will be analysed in order to achieve the goals that were set.

The second chapter provides a literature review that addresses the various topics on which this dissertation will be centered on, thereby providing clarification of the various articles already written and explaining to the reader THz technologies and RIS and MIMO systems.

The next chapter will describe the model for a hybrid UM-MIMO THz architecture, employing transmit and receive antenna arrays as well as reconfigurable intelligent surfaces.

The fourth chapter presents the results obtained from the simulations that were performed, as well as an analysis of the values and graphs that were produced during the simulations undertaken.

Finally, the fifth chapter outlines the conclusions of the proposed framework that has been studied, as well as the following key takeaways that can be suggested for future development in this domain of research.

1.6. Contributions

The study developed in this dissertation led to the realization of an article titled "Hybrid Precoder Algorithm Optimization in Reconfigurable Intelligent Surface-Assisted THz Ultra Massive MIMO Systems", where the system designed was tested and the results derived from the model are presented in the body of work. The article submitted is in appendix A.

1.7. Notation

The notations in this document are described as:

- $[.]^T$ - Transpose matrix
- $[.]^H$ - Conjugate transpose of a matrix/vector
- $\mathbf{I}_{n\times n}$ - Identity matrix of the dimension $n \times n$
- $diag(.)$ - Diagonal matrix whose elements are given in the argument
- $|.|$ - Modulus operator
- $\|.\|_F$ - Frobenius norm
- $det(.)$ - determinant

CHAPTER 2

Literature Review

2.1. 6G Wireless Networks

The evolution to 6G communication systems comes as a response to culminate the missing elements present on existing LTE and 5G systems. According to the recommendations outlined on ITU-R M.2083, 5G is designed to reach as far as 20 Gbps [**4**]. As a result, 5G communications are no longer sufficient as the ever growing pace of wireless communications globally and its large volume of data created and required have surpassed the current experience data rate supported.

The key features for a 6G system will focus on various components to enable and increase user experience data rate performance, focusing on increasing data availability as well as improving mobile data rates.

Future 6G communication systems will be developed in order to support programmable smart surfaces, AI, extended reality (XR), high fidelity mobile hologram, and digital replica. The main prerequisites for the migration from 5G to a 6G framework are associated with improving the energy and spectrum efficiency, increasing the peak data rate experience from previously achieving only 20 Gbps to reaching 1 Tbps [**5**].

The development and implementation of 6G networks requires a huge amount of real-time data processing, a hyper-fast data throughput, and extremely low latency. Terahertz technology is regarded as a leading contender for the implementation of 6G communications, by providing the bandwidth required to sustain high speed Tbps transmission for macro or micro services. MIMO antennas and ultra massive multiple-input multiple-output antennas, are also envisioned as a focal point in 6G communications with the aim of facilitating communications using high-powered beams targeted towards a specific direction to bypass the distance constraint that THz communications are prone to [**6**].

The main focus towards achieving higher data rates requires the allocation of higher blocks of spectrum in higher frequency bands than those already in use to accommodate the large amount of data traffic, and the increasing complexity of the devices currently in use so as to provide the bandwidth required to improve the quality of service by offering better service coverage. The 6G spectrum can be divided into three main sections [**7**]:

- **low-band:** Below 1GHz
- **mid-band:** Between 1-24 GHz
- **high-band:** Divided into two regions
  - mmWave band, between 24-92 GHz
  - Sub-THz frequency, from 92-300 GHz

2.2. Millimeter Wave

Millimeter wave bands already provide support to 5G and have a very substantial contribution towards the roll out of 6G technologies by enabling gigabit-per-second data rates in indoor systems for wireless networks.

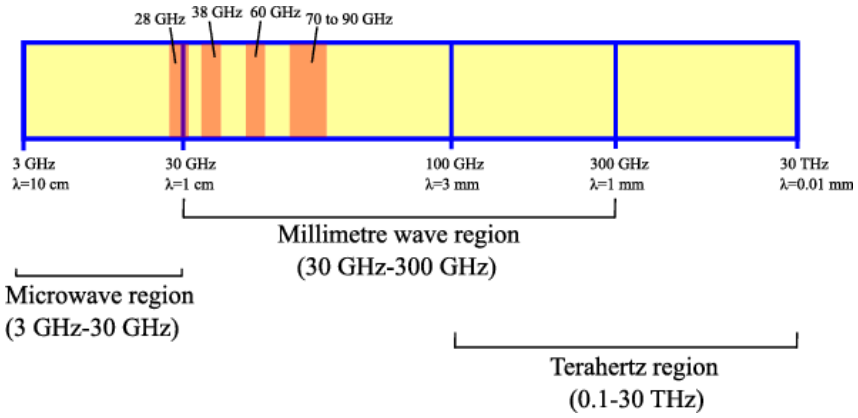

FIGURE 2.1. Electromagnetic spectrum for the mmWave and THz region. Source [**8**].

The mmWave spectrum is divided in multiple frequency smaller blocks. Each block can have differing bandwidths, depending on the requirements proposed by the user on the 5G service to be executed. Notably, 28 GHz has been successfully commercially developed and deployed in several countries, such as Japan and US [**7**].

2.3. Terahertz Communications

Terahertz Band is envisioned as a key wireless technology to satisfy the future demands within sixth generation (6G) systems by solving the spectrum scarcity problem observed on millimeter wave systems due to the narrowed bandwidths available [**1**].

The THz band offers higher spectrum efficiency, experienced data rate and peak data rate, as well as lower latency in comparison to existing 5G systems. The large bandwidth available in the THz band allows the transmission of high data rates in the order of terabits per second (Tbps) [**9**].

THz waves have radio frequency (RF) higher than millimeter waves resulting in forwarding data faster through the wireless network, however it presents lower wavelengths, ensuing in a shorter propagation distance possible.

2.3.1. THz Channel Behaviour

The channel characteristics operating at the THz band are susceptible to atmospheric loss, meaning molecular absorption loss due to water vapor and oxygen molecules at THz frequencies. This results in high path loss for line-of-sight (LoS) links by creating spectral windows with different bandwidths and distance variations [**1**].

The THz band is also significantly affected by Spreading Loss. According to Friis' Law the spreading loss increases quadratically with the frequency thus resulting in distance limitation with high propagation path loss [**10**].

6G THz systems suffer from high sparsity when electromagnetic (EM) waves are reflected, refracted, or absorbed on rough surfaces, resulting in attenuation as well as scattered waves amongst all directions. The higher the frequency in use, the higher the scattering will be [**11**].

THz waves exhibit both specular and diffuse scattering from most surfaces they come in contact with [**12**]. The electromagnetic wave that the transmitter sends out towards the receiver, as shown in figure 2.2, will generate a reflected wave and a scattered wave.

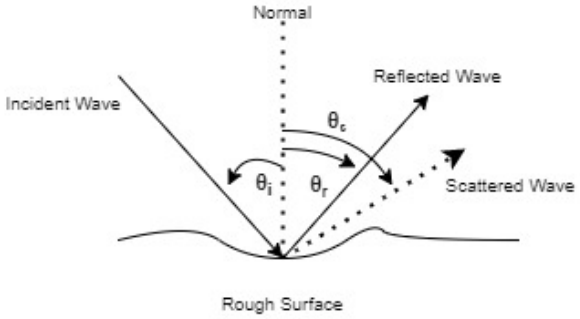

FIGURE 2.2. Incident radio wave at an angle θ_i with a rough surface creates a reflected wave, θ_r reflected angle, and a scattered wave with a θ_s angle.

Propagation at high carrier frequencies suffer from blockage between the transmitter and receiver, limiting the reliability of the Line-of-Sight path. To avoid obstructions, it is necessary to create multiple possible paths (multi-paths) to guarantee full coverage when LoS is obstructed.

Thus, MIMO systems relying on arrays implemented on metamaterials or metasurfaces, previously present on 5G systems, are seen as a good solution in order to improve the propagation paths that were severely affected in the THz band.

2.4. HyperSurfaces

Hypersurfaces are intelligent surfaces designed with the purpose of controlling the characteristics of the propagation environment in which they are installed. The intelligent surfaces are programmable and can control and change the electromagnetic behavior of the signals present in the ambient environment [**1**].

2.4.1. Metasurfaces

These surfaces are often described as metasurfaces for the use of materials that are responsible for shaping and modifying the propagation environment [**2**].

Metasurfaces have the ability to control electromagnetic waves due to their dielectric permittivity (ε) and magnetic conductivity (μ) properties.

There is a plethora of different types of metasurfaces, such as Reconfigurable Intelligent Surfaces (RIS), Large Intelligent Surfaces (LIS), Digitally Controllable Scatterers (DCS) and Software Controllable Surfaces (SCS).

The metasurfaces can also be distinguished according to the functions they are capable of accomplishing in the propagation environment in which they are deployed:

Active Surface: Smart surface geared to amplify and conduct signal processing procedures on incoming signal waves.

Passive Surface: Smart surface that cannot use power amplification during the operation phase.

Static surface: Surface that cannot be altered upon its implementation in the wireless communication system.

Dynamic/Reconfigurable Surface: Surface with digital signal processing capabilities that allow the configuration of the surface after being manufactured [**13**].

Metasurfaces are considered to be a solution for controlled wireless environment, namely Reconfigurable Smart Surfaces for the ability of being programmable and thereby turning the radio environment for wireless communications into a smart space [**3**].

The RIS that was considered the most suitable for implementation in this thesis is based on passive reflective elements, meaning that it does not require a power amplifier to forward the incoming signal, hence in relies only on simple digital signal processing to configure the intelligent surface [**13**].

2.5. Reconfigurable Intelligent Surfaces

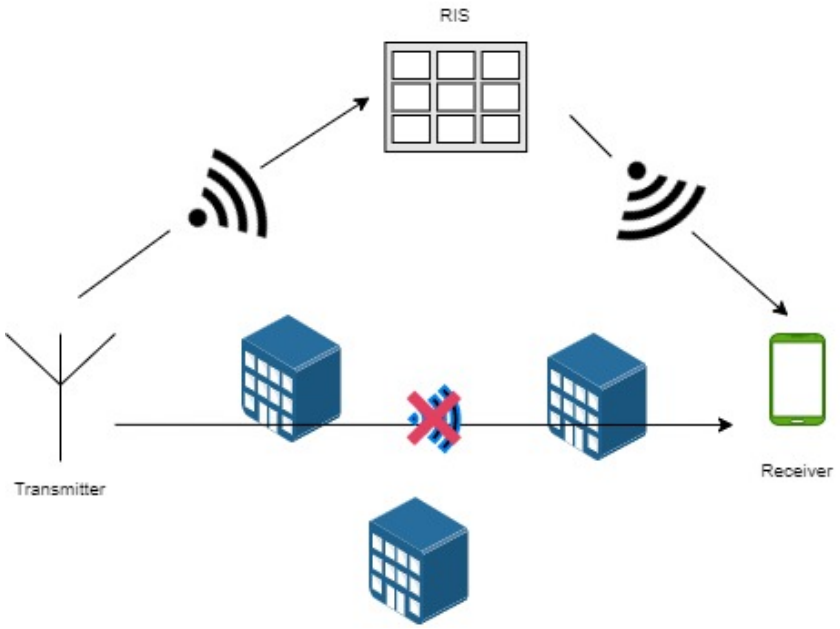

FIGURE 2.3. Example of a RIS application in a wireless environment with the LoS between the BS and the user obstructed

Reconfigurable Intelligent Surfaces are ultra-thin surfaces composed of materials capable of shaping the propagation environment by modifying the radio waves impinging upon the RIS surface and controlling their direction [**3**].

The RIS is configured to focus the beam it receives from the transmitter and redirect it towards the receiver intended. LoS blockages can be routed with the use of multi paths available on the environment, as seen in figure 2.3.

RIS are capable of being reconfigurable regarding the environment they encounter themselves in and can alter the wireless signals that are being propagated between the transmitter and receiver, thus enabling optimization of the transmitter as well as the receiver in use.

The implementation of RIS in communication systems has been demonstrated through the modeling of channel matrices for lower frequencies within the mmWave Band in [**14**] and [**15**]. The introduction of RIS structures for THz band are based on a RIS graphene model where this framework is viewed as one of the most efficient structures towards the THz frequency spectrum for reflecting almost in its entirety the THz wave in an operational frequency between 0.1 to 4 THz [**16**].

According to the laws of reflection, a conventional mirror is only capable of reflecting the impinging wave in an angular direction. However, the RIS can form and synthesize a beam as well as configure its shape and angle to focus the signal towards the receiver to maximize the Signal-to-noise ratio (SNR) [**17**].

2.5.1. RIS Structure

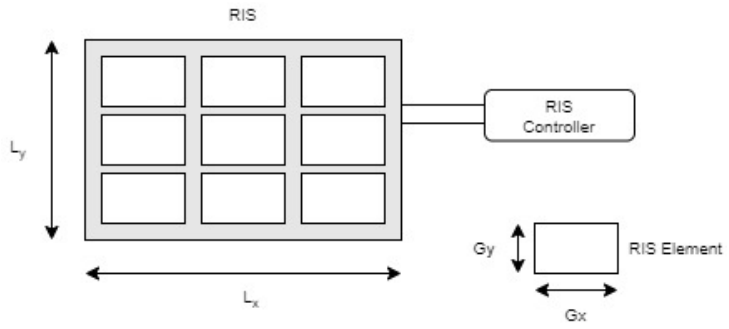

FIGURE 2.4. RIS architecture - RIS with N elements and a controller

Whilst the RIS for THz frequency is based on a graphene model, the RIS used in lower frequency bands is structured with N passive scattering elements and a tunable chip or PIN switch. The PIN diode has two modes: ON and OFF state. Each PIN diode interacts with an individual element on the RIS structure and communicates directly with the controller.

The controller associated with the RIS receives requests from external sources and configures the metasurface with the information received by adjusting the RIS elements, thus steering the beams and propagating the signal through the implementation of phase shifts [**3**].

The reconfiguration implemented by the controller has a bearing on the power consumption and efficiency of the system with its simultaneous system programming and reconfiguration [**17**].

The scattering elements are controlled via a software implemented on the RIS that changes EM properties of the radio-frequency (RF) signals in order to reflect it around existing obstacles, thus creating a multi-path effect. Upon receiving reconfiguration request from external devices, the synced chip can reconfigure itself according to the information given by the controller [**18**].

The N reconfigurable scatterers present in the RIS structure are all equipped with a small antenna that receives and re-radiates without amplification, but with a configurable time-delay.

For narrow-bands this delay corresponds to a phase shift. Assuming the phase-shifts are properly adjusted, the N scattered waves will add constructively at the receiver. The RIS reflects the RF signals as a passive array.

2.6. MIMO

Multiple-Input Multiple-Output (MIMO) systems employ several antennas at both ends of the link to increase the spectral efficiency as well as the number of users served simultaneously by being able to transmit multiple streams of data, a fundamental key for wireless communication systems [**19, 20**].

High gain antennas are adapted with MIMO systems in order to overcome the high path loss observed in either the mmWave band or the interference seen in THz band.

The frequency band 28 GHz, referred previously on the millimeter wave region, is proposed for 5G MIMO applications due to improving the gain and achieving high data rates regardless of the high signal attenuation observed [**21**].

2.6.1. UM-MIMO

Ultra-massive MIMO structures enables the high number of antenna arrays existing at each end to be grouped together, thus increasing the transmission throughput, as well as steering the narrow beam on the strongest path possible between the transmitter and receiver [**19**].

The beamforming (BF) technique used on MIMO systems is advantageous for its capability to overcome the attenuation present on mmWave and THz frequencies bands, thus improving the communication distance.

The spatial multiplexing scheme used on MIMO groups multiple streams on a single carrier to increase the capacity per user. This method of combining multiple streams is crucial when radio links are operated on a high signal-to-noise ratio (SNR) regime and have limitations regarding their bandwidth [**1**].

2.6.2. THz UM-MIMO System

A THz UM-MIMO model based on a point-to-point system between extensive antenna arrays is designed with N_{Tx} transmit antenna arrays and N_{Rx} and receive antennas arrays, represented in figure 2.5. The equation for the baseband signal in this case can be expressed as

$$\mathbf{y}(t) = \mathbf{H}(t)\mathbf{s}(t) + \mathbf{n}_t \tag{2.1}$$

whereas $y(t)$ is the received signal, $s(t)$ is the transmitted signal, $n(t)$ is the noise vector and $H(t)$ is the $N_{Tx} \times N_{Rx}$ matrix, representing the THz UM-MIMO channel [**22**].

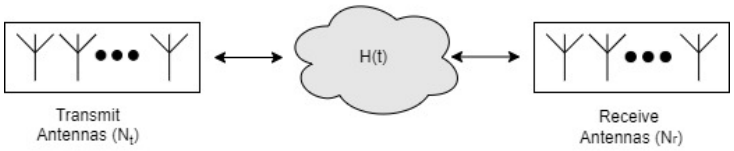

FIGURE 2.5. UM-MIMO System Scheme

The multiple antennas deployed on the THz channel create multiple propagation paths, each one with unique angles of departure and arrival (AoD/AoA). However, the high frequency employed on this system increases the free spreading loss (L_{spread}), obtained according to Friis formulation [**23**],

$$L_{spread}(f, d) = \left(\frac{4\pi f d}{c}\right)^2 \tag{2.2}$$

where c represents the speed of light, f the carrier frequency, and d the distance where the loss is calculated.

The high attenuation present in the THz band is solvable with the implementation of the UM-MIMO framework and its hybrid precoder framework. The use of RIS within UM-MIMO communication systems can surpass the high energy intake that is generated while communicating from the transmitter antennas to the receiver using THz frequency band.

2.7. Beamforming

Beamforming (BF) is a technique used with the objective of targeting all the signal waves that are currently in transmission to the intended destination.

Beamforming allows the base station (BS) to find a suitable route to deliver data to the user, thus reducing possible interference the signal waves could suffer from other devices present in the same wireless environment. The link signal-to-noise ratio (SNR) increases with the output of each antenna element combined.

The implementation of beamforming in massive MIMO systems increases spectrum efficiency and the capability of multi-path.

On mmWave, whereas the wavelength used is shorter and the propagation is limited due to possible obstacles between the BS and the user, beamforming is used to achieve higher data rates by directing all the signal waves, such as concentrated beams, towards the user thus reducing interference with other users [**19**].

The main types of beamforming architectures that will be studied along this project are digital beamforming, analog beamforming and hybrid beamforming (HBF).

2.7.1. Digital Beamforming Architecture

A fully digital beamforming architecture uses a single radio frequency (RF) chain and DAC/ADC for each single antenna. Digital BF architecture is not practical for systems that implement a high number of antennas, including THz UM-MIMO systems, due to the fact that its power consumption and hardware complexity cannot be supported for its high costs [**19**].

2.7.2. Analog Beamforming Architecture

A fully analog beamforming architecture uses only one RF chain and DAC/ADC to control all existing antennas in the system through the use of phase shifters.

The analog scheme reduces drastically the power consumption, as well as the hardware complexity with the use of a single RF chain, however it only supports a single data stream at a time, thus limiting the number of users and the data rate it produces. This architecture is not practical for systems that require a high number of antennas for its many users.

2.7.3. Hybrid Beamforming Architecture

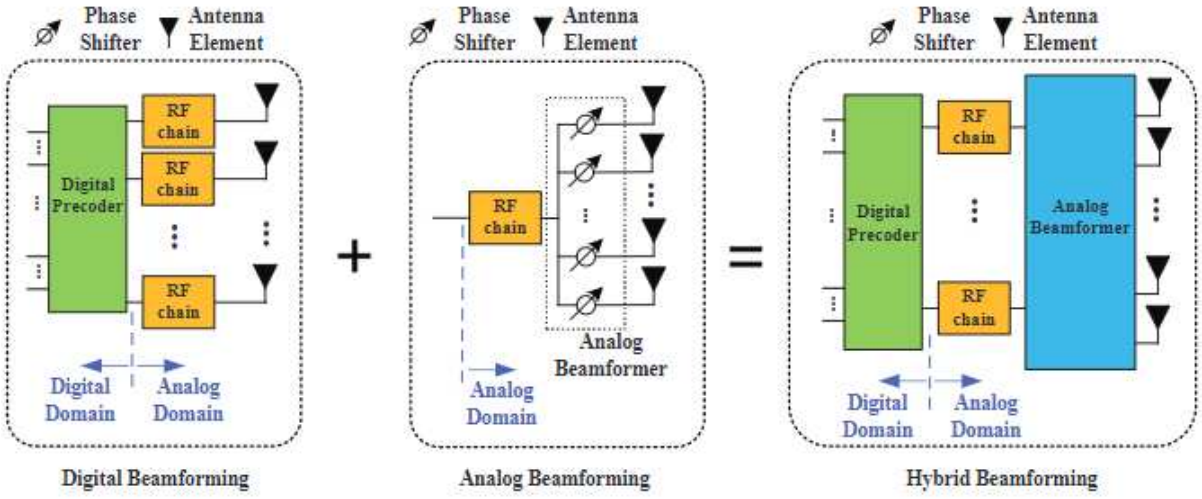

FIGURE 2.6. Hybrid Beamforming scheme, resulting from the combination of the digital and analog beamforming. Retrieved from [**19**].

The hybrid beamforming architecture combines the analog and digital BF schemes.

It employs a limited number of RF chains and DAC/ADC combined with phase-shift networks, thus achieving performance levels similar to digital beamforming but with lower hardware implemented, i.e. lower costs, and lower power consumption overall. This solution is the most suitable for THz UM-MIMO systems [**24, 11**].

Figure 2.6 shows the HBF architecture resulting from the combination of digital and analog beamforming techniques on the base station responsible for transmitting the signal.

2.7.4. Hybrid Beamforming Scheme for RIS

RIS consists of a large number of RIS elements, or antenna elements far away from the Base Station, configured to do analog beamforming, though the existent phase shifters in each RIS element. These RIS elements do not have any digital processing capacity, requiring signal processing to be carried out at the BS.

Digital beamforming is realized at the Base Station where each antenna is responsible for encoding the data stream and transmitting it. Analog beamforming is executed by the RIS through discrete phase shifts responsible for the reflection of the incident wave. All signals obtained in each RIS element will be grouped together and form the signal the user will receive [**24**].

CHAPTER 3

Hybrid Precoder and RIS Optimization

The THz band limits severely the feasible distance between transmitter and receivers, requiring the implementation of high-gain antennas capable of directing the incoming signal in order to transmit it successfully. The deployment of RIS surfaces, capable of controlling the distribution of the receiving electric current, i.e. the signal, and modifying its direction are seen as a solution to improve the efficiency rate and obtain higher achievable throughput rates for the THz and mmWave bands for UM-MIMO systems in comparison to the rates obtained using the direct propagation path between the BS and the user.

The main function of RIS is distributing the electromagnetic (EM) currents coming from the transmitter antennas towards the numerous elements that compose a RIS. The current signal will be controlled and modified by the RIS elements in order to modify its path and allow to impinge the signal towards its final destination, the receiver antennas [**15**].

It will be modeled a channel for two distinct scenarios: firstly when the direct path between the transmit and receive antennas is blocked, thus there is only the propagation link using a RIS. Secondly, the channel model will assume that both paths are available in order to analyse how the link in use affects the signal.

The RIS is responsible for receiving the signals from the transmitter antennas. Subsequently, the signal received by the RIS undergoes a phase shift at each RIS element to which the signal is directed and a new channel matrix is created.

The end-to-end channel matrix is composed with N_{Tx} large transmit antenna arrays and N_{Rx} large receive antenna arrays in operation, as well as a RIS with N_{RIS} reflecting elements.

3.1. Channel Modeling

The original simplified channel matrix without RIS employs a point-to-point system stemming from the large antenna transmit arrays towards the receiver antenna array. All the existent transmit antennas generate the entrance signal and the receiver antennas acquire the exit signal. The total antenna matrix $\mathbf{H}$, that represents the effect of the channel on the signal sent between the each Tx and Rx antenna, will be applied to the symbol vector $\mathbf{s}$ in use, whether the modulation in use is QAM or PSK, the precoder matrix of the base station $\mathbf{F} \in \mathbb{C}^{N_{Tx} \times N_s}$, the user combiner matrix $\mathbf{W} \in \mathbb{C}^{N_{Rx} \times N_s}$ and the average received power, ρ.

The Gaussian noise vector, $\mathbf{n}$, represents the complex N_{Rx} noise components on each destination receiver antenna where $n \in \mathbb{C}^{N_{Rx} \times 1}$. The noise vector is independent and identically distributed random variables (IID) containing zero mean circularly symmetric and complex Gaussian [**25, 26**].

The resulting vector, $\mathbf{r}$, will be represented as:

$$\mathbf{r} = \sqrt{\rho}\mathbf{W}^H\mathbf{H}\mathbf{F}\mathbf{s} + \mathbf{n} \tag{3.1}$$

Each symbol can be modulated in the amplitude, A, as well as in phase $e^{\theta j}$, resulting in $S = Ae^{\theta j}$. The combination of both amplitude and phase modulation creates a symbol that is independent for each channel the signal comes into contact with.

The data stream is composed of multiple symbols, thus $\mathbf{s} = [S_1 \dots S_{Ns}]^T$, where $N_s = E\left[\|\mathbf{s}\|^2\right]$.

3.2. Channel Modeling for RIS Systems

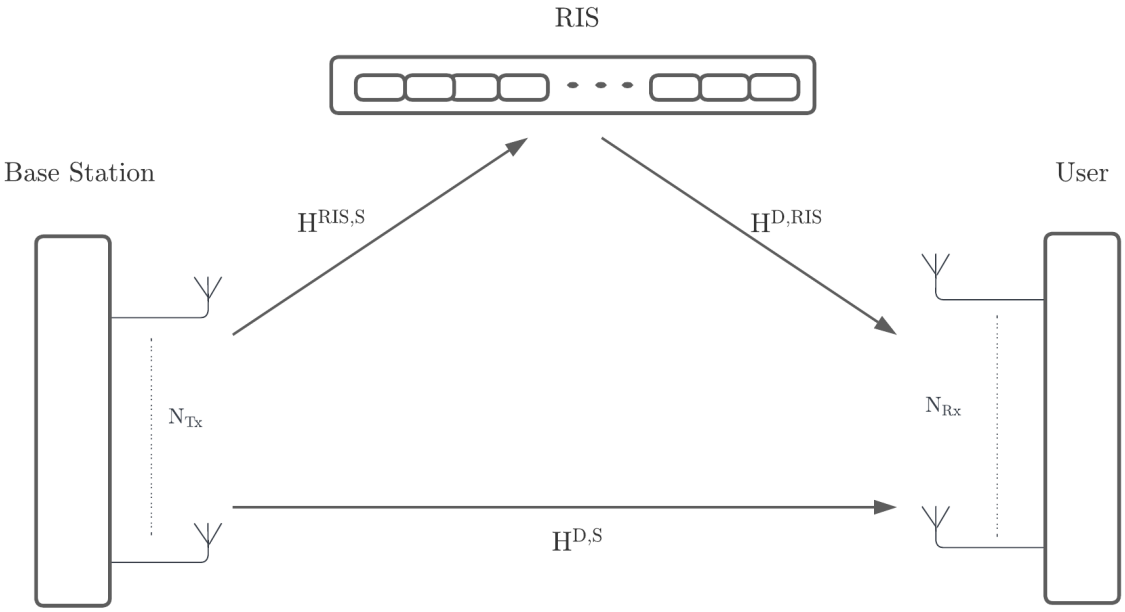

FIGURE 3.1. RIS-assisted communications with LoS and NLoS links between base station and user.

According to the new scenario in study, represented in figure 3.1, the resulting vector $\mathbf{r}$ will have new factors resulting from the addition of reconfigurable intelligent surfaces to the channel modeling system resulting in a new vector, $\mathbf{r}$.

$$\mathbf{r} = \sqrt{\rho}\mathbf{W}^H\mathbf{H}^{total}\mathbf{F}\mathbf{s} + \mathbf{n} \tag{3.2}$$

The antenna matrix represented as $\mathbf{H}$ on 3.1 is changed to $\mathbf{H}^{total}$ on equation 3.2 as a result of the introduction of Reconfigurable Intelligent Surfaces, thereby including two distinct channel matrices that depart from the transmit antennas.

The vector **r** will be altered with the introduction of RIS elements, thus suffering the effect of three distinct channel matrices between the connection with the transmitter, RIS and receiver antennas:

$\mathbf{H}^{RIS,S}$: Channel matrix between the source, transmit antennas, N_{Tx}, and the RIS elements, N_{RIS}, whereas $\mathbf{H}^{RIS,S} \in \mathbb{C}^{N_{RIS} \times N_{Tx}}$.

$\mathbf{H}^{D,RIS}$: Channel matrix between RIS elements and the destination, the receive antennas, N_{Rx}, whereby $\mathbf{H}^{D,RIS} \in \mathbb{C}^{N_{Rx} \times N_{RIS}}$.

Φ : Phase Shift matrix, diagonal matrix, as represented in 3.3, acquires the response of each RIS element.

$$\Phi = \begin{bmatrix} e^{\alpha j} & & & \\ & e^{\alpha j} & & \\ & & \dots & \\ & & & e^{\alpha j} \end{bmatrix} = diag\,(\boldsymbol{\varphi}) \tag{3.3}$$

The RIS is able to control and alter the phase shift of the signal it receives since each RIS element acts as a new signal source by capturing the transmitted signals. In response, it will be created a matrix proportional to the number of RIS elements in use, represent the signal effect between the RIS and the end user,$\mathbf{H}^{RIS,D}$.

The use of the THz band makes the direct link between the transmit and receiver antennas obsolete for its high attenuation values when there is no LoS. As a result the total channel matrix is given as

$$\mathbf{H}_a^{total}(\boldsymbol{\varphi}) = \mathbf{H}^{D,RIS}\boldsymbol{\Phi}\mathbf{H}^{RIS,S} \tag{3.4}$$

the channel matrix H^{total} in use will differ for the system that applies mmWave band in comparison to the channel matrix for higher frequencies, on account of its attenuation not being as severe, thus both paths are available for transmitting the desired signal towards its recipient. As a result, it will be added a new channel matrix between source and destination, $\mathbf{H}^{D,S} \in \mathbb{C}^{N_{Rx} \times N_{Tx}}$, resulting on

$$\mathbf{H}_b^{total}(\boldsymbol{\varphi}) = \mathbf{H}^{D,RIS}\boldsymbol{\Phi}\mathbf{H}^{RIS,S} + \mathbf{H}^{D,S} \tag{3.5}$$

3.2.1. Indirect Link Channel Matrix

The expression for each channel matrix between BS-RIS-user connection is represented in Eq. 3.6 and 3.10.

The connection from the Transmitter passing through the RIS towards the Receiver has 3 distinct link channel matrices in a THz UM-MIMO channel:

- Transmitter - RIS
- RIS - Receiver
- Transmitter - Receiver

The THz and mmWave model considered here adopt a channel where the rays arrive in clusters [**27**], thus the channel matrix between the base station and RIS, $H^{RIS,S}$, can be written as

$$\mathbf{H}^{RIS,S} = \sum_{c=1}^{C}\sum_{s=1}^{S_c} \beta_{c,s}\sqrt{\frac{PL_{NLOS}^{RIS,S}}{K_{rice}}}\mathbf{a}_{RIS}(\phi_{c,s}^{RIS,S}, \theta_{c,s}^{RIS,S})\mathbf{a}_S(\phi_{c,s}^{S}, \theta_{c,s}^{S}) + \mathbf{H}_{LOS}^{RIS,S} \tag{3.6}$$

each channel matrix has a LoS for that path. In regards to the $\mathbf{H}^{RIS,S}$ matrix, the $\mathbf{H}_{LOS}^{RIS,S}$ depicts the Line-of-Sight component for the path between Tx-RIS.

Moreover, C and S_c represent the number of clusters and rays in each cluster for the link specified, Tx-RIS, for the $(c,s)th$ propagation path existent. $\beta_{c,s}$ denotes the complex Gaussian distributed path coefficient.

The clusters and the arrays present within each cluster have particular angles of arrival and departure, thus the vectors $\mathbf{a}_S(\phi_{c,s}^{S}, \theta_{c,s}^{S})$ and $\mathbf{a}_{RIS}(\phi_{c,s}^{RIS,S}, \theta_{c,s}^{RIS,S})$ represent the array response vector, for the considered azimuth $\phi_{c,s}$ and elevation $\theta_{c,s}$ for the angles of arrival (AoA) or the angles of departure (AoD).

In equation 3.6 AoD is represented as $\mathbf{a}_S$ for the large transmitter antenna array and AoA is outlined as $\mathbf{a}_{RIS}$ for the RIS, respectively. Assuming an uniform planar array (UPA) implementation, the array response vector for the transmitter, $\mathbf{a}_S(\phi_{c,s}^{S}, \theta_{c,s}^{S})$ is calculated [**14, 28**] as

$$\begin{aligned}\mathbf{a}_S(\phi_{c,s}^{S}, \theta_{c,s}^{S}) = \Big[1, ..., e^{j\frac{2\Pi}{\lambda}d_s(a\sin\left(\phi_{c,s}^{S}\right)\sin\left(\theta_{c,s}^{S}\right)+b\cos\left(\theta_{c,s}^{S}\right))}, \ldots, \\ e^{j\frac{2\Pi}{\lambda}d_s((\sqrt{N_{Tx}}-1)\sin\left(\phi_{c,s}^{S}\right)\cos\left(\theta_{c,s}^{S}\right)+(\sqrt{N_{Tx}}-1)\cos\left(\theta_{c,s}^{S}\right))}\Big]^T\end{aligned} \tag{3.7}$$

where $0 \leqslant a \leqslant (\sqrt{N_{Tx}} - 1)$ and $0 \leqslant b \leqslant (\sqrt{N_{Tx}} - 1)$, a and b represent the width and height of the square array for the antennas, respectively. λ is the signal wavelength and d_s is the spacing between elements in the transmission matrix.

The expression of the channel vector, $\mathbf{H}_{LOS}^{RIS,S}$ is written as

$$\mathbf{H}_{LOS}^{RIS,S}(n,m) = \sqrt{\frac{G_{Tx}\ A_{RIS}}{(4\pi d_{n,m})^2}e^{-k_{abs}(f)d_{n,m}}}e^{-j2\pi\frac{d_{n,m}}{\lambda}} \tag{3.8}$$

The line-of-sight expression in 3.8 for the link between the transmitter and RIS, represents the transmit antenna gain as G_{Tx} and A_{RIS} signifies the area of RIS element, obtained through $A_{RIS} = \lambda^2$. The variable n describes the n^{th} RIS element and the m^{th} transmitter antenna element, thus $d_{n,m}$ denotes the distance for each existent transmitter antenna and RIS element. The coefficient of the molecular absorbing loss is represented as $k_{abs}(f) = 0.0033$ [**29**].

The path loss of the NLoS channel between Tx-RIS for the $(c,s)th$ element is obtained through

$$PL_{NLOS}^{RIS,S} = \frac{G_{Tx}A_{RIS}}{(4\pi d_{s,RIS})^2} e^{-k_{abs}(f)d_{s,RIS}} \tag{3.9}$$

whereas $d_{s,RIS}$ is the distance between the transmitter and the RIS element in use.

As the path loss is applied, the rice factor is implemented in order to normalize the channel. The Rice factor, K_{rice}, denotes the relative level of the LOS component, thus it indicates the quality of the channel and the fading the path is subjected to. As a result, the Rician factor represents the ratio between the LOS and NLOS components [**30**].

The sub-channel matrix from the RIS towards the Receiver, RIS-Rx, denominated as $\mathbf{H}^{D,RIS}$ will be written similarly as the equation 3.6

$$\mathbf{H}^{RIS,S} = \sum_{c=1}^{C}\sum_{s=1}^{S_c} \beta_{c,s}\sqrt{PL_{NLOS}^{D,RIS}}\mathbf{a}_{RIS}(\phi_{c,s}^{D,RIS}, \theta_{c,s}^{D,RIS})\mathbf{a}_D(\phi_{c,s}^{D}, \theta_{c,s}^{D}) + \mathbf{H}_{LOS}^{D,RIS} \tag{3.10}$$

3.2.2. Direct Link Channel Matrix

The activation of the direct LoS between the transmitter and receiver also generates an unique channel matrix, $\mathbf{H}^{D,S}$

$$\mathbf{H}^{D,S} = \sum_{c=1}^{\tilde{C}}\sum_{s=1}^{\tilde{S}_c} \tilde{\beta_{c,s}}\sqrt{\frac{PL_{c,s}^{D,S}}{K_{rice}}}\mathbf{a}_D(\phi_{c,s}^{D}, \theta_{c,s}^{D})\mathbf{a}_S(\phi_{c,s}^{S}, \theta_{c,s}^{S}) + \mathbf{H}_{LOS}^{D,S} \tag{3.11}$$

the channel represented on 3.11, is calculated using the array response vectors of the transmitter and receivers and the attenuation of the $(c, s)th$ propagation path.

3.3. System Model

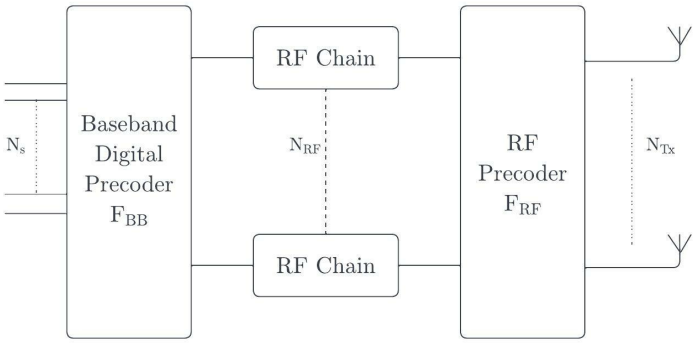

FIGURE 3.2. General architecture of a hybrid precoder.

It was considered an UM-MIMO system operating in a mmWave/THz frequency band where the base station (BS) has a large N_{Tx} antenna array.

A traditional digital precoding is not suitable for ultra massive MIMO systems due to the fact that it would require each antenna to be equipped with a radio frequency (RF) chain, thus it would increase exponentially the complexity of the circuit as well as the cost of the hardware to be installed.

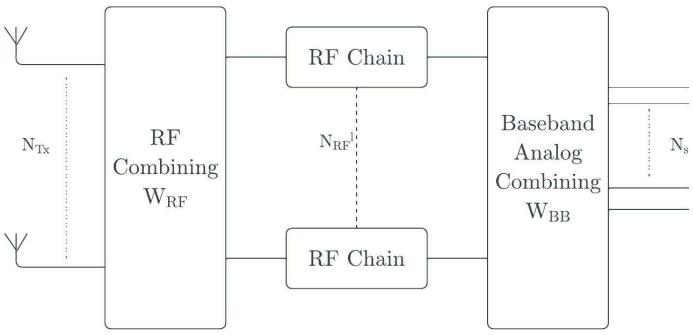

FIGURE 3.3. General architecture of a hybrid combiner.

Instead of a fully digital design that would require a dedicated RF chain per antenna element, both the precoder and combiner comprise separate digital and analog processing blocks. This separation reduces greatly the number of digital blocks used, thus only a few RF chains are needed in order to implement the structure. The digital blocks are also complemented with analog blocks that are supported on networks of phase shifters and switches.

3.3.1. Hybrid precoder

The usage of a hybrid precoder enables the conjoined use of an analog as well as a digital precoder. As follows, the propagation channel that reaches the end user on equation 3.2 is modified by separating the fully digital precoder $\mathbf{F}$ into two distinct matrices representing the digital and the analog precoder. The processed received signal when implementing a hybrid precoder is obtained as

$$\mathbf{r} = \sqrt{\rho}\mathbf{W}\mathbf{H}^{total}\mathbf{F}_{RF}\mathbf{F}_{BB}\mathbf{s} + \mathbf{W}\mathbf{n} \tag{3.12}$$

where s is the symbol vector, $\mathbf{F}_{BB} \in C^{N_{RF} \times Ns}$ represents the baseband matrix obtained through $F_{BB} = N_{RF}N_s$, the RF precoder matrix $\mathbf{F}_{RF} \in C^{N_{Tx} \times N_{RF}}$, ρ designates the average received power and the channel noise is represented as n. The noise vector $n \in C^{N_{Tx} \times 1}$ is an additive white Gaussian function with a variance of σ_n^2 and zero mean.

The overall channel matrix, $\mathbf{H}^{total}$, on equations 3.4 and 3.5 can be represented using the singular value decomposition (SVD). In this instance, $\mathbf{H}^{total}$ is obtained through,

$$\mathbf{H}^{total} = \mathbf{U}\Lambda\mathbf{V}^H \tag{3.13}$$

where $\mathbf{U}$ and $\mathbf{V}$ are both unitary matrices measuring $N_{Rx} \times N_{Rx}$ and $N_{Tx} \times N_{Tx}$ where $\mathbf{U}\mathbf{U}^H = \mathbf{U}^H\mathbf{U} = I_{N_{Rx}}$ and $\mathbf{V}\mathbf{V}^H = \mathbf{V}^H\mathbf{V} = I_{N_{Tx}}$, respectively. Λ represents a diagonal matrix of $N_{Rx} \times N_{Tx}$ [**31**].

The precoder matrix is defined as $\mathbf{F} = \mathbf{V}[: 1 : N_s]$ for a fully digital structure. Albeit, instead of using a fully digital design, it will be implemented an hybrid system using an analog precoder, in order to avoid installing digital-analog converters (DAC) on every

single antenna, thus reducing the hardware complexity whilst achieving a performance close to the design that employs a fully digital circuit.

The algorithm to be developed with the hybrid design will employ a smaller digital precoder. The baseband digital precoder is connected through several radio frequency chains to the analog precoder, responsible for generating the final signal that will be transmitted on each existent N_{Tx} antenna, as seen in figure 3.2.

The hybrid combiner $\mathbf{W}$ is obtained via $\mathbf{W} = \mathbf{W}_{RF}\mathbf{W}_{BB}$, representing the RF combiner $\mathbf{W}_{RF} \in C^{N_{Rx} \times N_{RF}^{Rx}}$ and the baseband combiner $\mathbf{W}_{BB} \in C^{N_{RF}^{Rx} \times N_s}$, represented in figure 3.3. Both matrices $\mathbf{F}_{RF}$ and $\mathbf{W}_{RF}$ are implemented in analog, where the RF signal processing will depend on the architecture that is selected and implemented [**32**].

Using the analog and the digital precoder matrices, the hybrid precoder design problem will be formulated as

$$\min_{\mathbf{F}_{RF},\mathbf{F}_{BB},\Phi} - \ln\det\left(\mathbf{I}_{N_{Rx}} + \frac{\rho}{P_N}\mathbf{H}^{total}\mathbf{F}_{RF}\mathbf{F}_{BB}^{H}\mathbf{F}_{RF}^{H}\mathbf{H}^{total^H}\right) \tag{3.14}$$

$$\text{subject to} \begin{cases} \left\|\mathbf{F}_{RF}\,\mathbf{F}_{BB}\right\|_F^2 \leq P_{Tx} \\ |\Phi(k)| = 1, k \in |1, ..., N_{RIS}| \\ \mathbf{F}_{RF} \in C^{N_{Tx} \times N_{RF}} \end{cases} \tag{3.15}$$

where the power per stream ρ suffers from noise power calculated using $P_N = \sigma^2$.

The problem on 3.14 must be solved under the constraints defined in 3.15, where $\mathbf{F}_{RF} \in C^{N_{Tx} \times N_{RF}}$ represents the set of matrices that will vary depending on the hybrid architecture to be adopted, since each set of precoding analog matrices are defined according to the RF structure that is implemented. The algorithm for the hybrid precoder must be designed to be able to handle the various RF architectures that can be implemented. The restriction imposed $\left\|\mathbf{F}_{RF}\,\mathbf{F}_{BB}\right\|_F^2 \leq P_{Tx}$ enforces the total power constraint at the transmitter.

The three restrictions render the Proximal Gradient algorithm difficult to apply all at once. Thus, the alternative is the implementation of Alternating Minimization.

In order to avoid the problem noted above, it will be used the proximal gradient algorithm [**33**] to firstly fix $\mathbf{F}_{RF}$ and Φ whilst solving over $\mathbf{F}_{BB}$ according to the expression

$$\min_{\mathbf{F}_{BB}} - \ln\det\left(\mathbf{I}_{N_{Rx}} + \frac{\rho}{P_N}\mathbf{H}^{total}\mathbf{F}_{RF}\mathbf{F}_{BB}^{H}\mathbf{F}_{RF}^{H}\mathbf{H}^{total^H}\right) \tag{3.16}$$

$$\text{subject to} \left\|\mathbf{F}_{RF}\,\mathbf{F}_{BB}\right\|_F^2 \leq P_{Tx}, (P_{Tx} = N_s) \tag{3.17}$$

the equation on 3.16 can be simplified by adopting $\widetilde{\mathbf{H}} = \mathbf{H}^{total}\mathbf{F}_{RF}$,

$$\min_{\mathbf{F}_{BB}} f(\mathbf{F}_{BB}) = - \ln\det\left(\mathbf{I}_{Ns} + \frac{\rho}{P_N}\mathbf{F}_{BB}^{H}\widetilde{\mathbf{H}}^{H}\widetilde{\mathbf{H}}\mathbf{F}_{BB}\right) \tag{3.18}$$

$$\text{subject to } \left\|\mathbf{F}_{RF}\ \mathbf{F}_{BB}\right\|_F^2 \leq P_{Tx} \tag{3.19}$$

the restriction on 3.19 can be integrated on the problem referenced in 3.18, resulting in

$$\min_{\mathbf{F}_{BB}} f(\mathbf{F}_{BB}) = -\ln\det\left(\mathbf{I}_{Ns} + \frac{\rho}{P_N}\mathbf{F}_{BB}^H\widetilde{\mathbf{H}}^H\widetilde{\mathbf{H}}\mathbf{F}_{BB}\right) + \underset{\|\mathbf{F}_{RF}\,\mathbf{F}_{BB}\|_F \leqslant P_{Tx}}{\mathbf{I}(\mathbf{F}_{BB})} \tag{3.20}$$

According to the expression deduced on 3.20 the baseband matrix can be calculated by using the proximal gradient algorithm [**33**],

$$\mathbf{F}_{BB}^{(t+1)} = prox_{\lambda\mathbf{I}_{\|\mathbf{F}_{RF}\,\mathbf{F}_{BB}\|_F \leqslant P_{Tx}}}[\mathbf{F}_{BB}^{(t)} - \nabla_{\mathbf{F}_{BB}^*} f(\mathbf{F}_{BB}^{(t)})] \tag{3.21}$$

the gradient needed in equation 3.21 for the expression $\mathbf{F}_{BB}^{(t+1)}$ can be obtained via:

$$\begin{aligned}\nabla_{\mathbf{F}_{BB}^*} f(\mathbf{F}_{BB}^{(t)}) = \frac{\partial f}{\partial \mathbf{F}_{BB}^*} = -\frac{\rho}{P_N}\widetilde{\mathbf{H}}^H\widetilde{\mathbf{H}}\mathbf{F}_{BB}^{(t)}(\mathbf{I}_{Ns} + \frac{\rho}{\rho_N}\mathbf{F}_{BB}^{(t)^H}\widetilde{\mathbf{H}}^H\widetilde{\mathbf{H}}\mathbf{F}_{BB}{}^{(t)})^{-1} \\ = -\frac{\rho}{P_N}\mathbf{F}_{RF}^H\mathbf{H}^{total^H}\mathbf{H}^{total}\mathbf{F}_{RF}\mathbf{F}_{BB}^{(t)}(\mathbf{I}_{Ns} + \frac{\rho}{P_N}\mathbf{F}_{BB}^{(t)^H}\mathbf{F}_{RF}^H\mathbf{H}^{total^H}\mathbf{H}^{total}\mathbf{F}_{RF}\mathbf{F}_{BB}^{(t)})^{-1}\end{aligned} \tag{3.22}$$

The equation 3.22 enables the problem to be optimized, following the previous methodology and allowing the baseband matrix to be obtained, through the calculation of the proximal operator in equation 3.21 by normalizing the matrix $\mathbf{F}_{BB}$. As a result, the minimization expression with fixed $\mathbf{F}_{BB}$ is expressed as

$$\begin{aligned}\min_{\mathbf{F}_{RF},\Phi} -\ln\det\left(\mathbf{I}_{N_{Rx}} + \frac{\rho}{P_N}\mathbf{H}^{total}\mathbf{F}_{RF}\mathbf{F}_{BB}\mathbf{F}_{BB}^H\mathbf{F}_{RF}^H\mathbf{H}^{total^H}\right) = \\ = -\ln\det\left(\mathbf{I}_{Ns} + \frac{\rho}{P_N}\mathbf{F}_{BB}^H\mathbf{F}_{RF}^H\mathbf{H}^{total^H}\mathbf{H}^{total}\mathbf{F}_{RF}\mathbf{F}_{BB}\right)\end{aligned} \tag{3.23}$$

$$\text{subject to}\begin{cases}\left\|\mathbf{F}_{RF}\ \mathbf{F}_{BB}\right\|_F^2 \leq P_{Tx} \\ \mathbf{F}_{RF} \in C^{N_{Tx}\times N_{RF}} \\ |\Phi(k)| = 1\end{cases} \tag{3.24}$$

The problem formulated on 3.23 and 3.24 allows to apply the proximal gradient to the phase shifting matrix, Φ, and the RF precoder ,$\mathbf{F}_{RF}$, for $t+1$ iteration in conjunction

$$\begin{cases}\Phi^{(t+1)} = prox_{\mu I_{(.)=1}}(\Phi^{(t)} - \lambda\nabla_{\Phi^*} f(\Phi^{(t)}) \\ \mathbf{F}_{RF}^{(t+1)} = prox_{\mu I_{\left\|.\right\|_F^2 \leq P_{Tx}}}(\mathbf{F}_{RF}^{(t)} - \lambda\nabla_{\mathbf{F}_{RF}^*} f(\mathbf{F}_{RF}{}^{(t)})\end{cases} \tag{3.25}$$

the proximal operator in the expression $\Phi^{(t+1)}$ in 3.25 is calculated by normalizing each element in the vector, whereas the proximal operator for the expression $\mathbf{F}_{RF}^{(t+1)}$ is obtained through the projection of the $\mathbf{F}_{RF}$ matrix. The calculation of the RF precoder depends on the architecture in use.

The expressions on 3.25 require the expression ∇_{Φ^*} that denote the gradient of $f(.)$ which can be obtained as

$$\begin{aligned}\nabla_{\Phi^*} f =& \frac{\partial f}{\partial \Phi^*} = -diag\left[(\mathbf{H}^{RD})^H \mathbf{H}^{total} \mathbf{F}_{RF} \mathbf{F}_{BB} \times \right. \\ & \left. \times \left(\mathbf{I}_{Ns} + \frac{\rho}{P_N} \mathbf{F}_{BB}^H \mathbf{F}_{RF}^H \mathbf{H}^{total^H} \mathbf{H}^{total} \mathbf{F}_{RF} \mathbf{F}_{BB}\right)^{-1} \mathbf{F}_{BB}^H \mathbf{F}_{RF}^H (\mathbf{H}^{SR})^H \right]\end{aligned} \tag{3.26}$$

where f is defined as

$$f = -\ln |\mathbf{I}_{Ns} + \beta \, \mathbf{F}_{BB}^H \mathbf{F}_{RF}^H X \, \mathbf{F}_{RF} \mathbf{F}_{BB}| \, , \begin{cases} \beta = \frac{\rho}{P_N} \\ X = \mathbf{H}^{total^H} \mathbf{H}^{total} \end{cases} \tag{3.27}$$

utilizing the expression in 3.25 requires the computation of gradient $\nabla_{F_{RF}^*}$ which can be written as

$$\nabla_{F_{RF}^*} f = \frac{\partial f}{\partial F_{RF}^*} \tag{3.28}$$

thus, the first df can be deduced as

$$\begin{aligned} df &= -d \ln |\mathbf{I} + \beta \, \mathbf{F}_{BB}^H \mathbf{F}_{RF}^H X \, \mathbf{F}_{RF} \mathbf{F}_{BB}| \\ &= -T\Omega[(\mathbf{I} + \beta \mathbf{F}_{BB}^H \mathbf{F}_{RF}^H X \mathbf{F}_{RF} \mathbf{F}_{BB})^{-1} d(\mathbf{I} + \beta \mathbf{F}_{BB}^H \mathbf{F}_{RF}^H X \mathbf{F}_{RF} \mathbf{F}_{BB})] \\ &= -T\Omega[(.)^{-1} d(\beta \mathbf{F}_{BB}^H \mathbf{F}_{RF}^H X \mathbf{F}_{RF} \mathbf{F}_{BB})] \\ &= -T\Omega[(.)^{-1} (\beta \mathbf{F}_{BB}^H d\mathbf{F}_{RF}^H X \mathbf{F}_{RF} \mathbf{F}_{BB} + \beta \mathbf{F}_{BB}^H \mathbf{F}_{RF}^H X d\mathbf{F}_{RF} \mathbf{F}_{BB})] \\ &= -T\Omega[(.)^{-1} \beta \mathbf{F}_{BB}^H d\mathbf{F}_{RF}^H X \mathbf{F}_{RF} \mathbf{F}_{BB}] - T\Omega[(.)^{-1} \beta \mathbf{F}_{BB}^H \mathbf{F}_{RF}^H X d\mathbf{F}_{RF} \mathbf{F}_{BB}] \\ &= -T\Omega[\beta d\mathbf{F}_{RF}^H X \mathbf{F}_{RF} \mathbf{F}_{BB} (.)^{-1} \mathbf{F}_{BB}^H] - T\Omega[\beta \mathbf{F}_{BB} (.)^{-1} \mathbf{F}_{BB}^H \mathbf{F}_{RF}^H X d\mathbf{F}_{RF}] \\ &= +T\Omega[-\beta (X \mathbf{F}_{RF} \mathbf{F}_{BB} (.)^{-1} \mathbf{F}_{BB}^H)^T d\mathbf{F}_{RF}^*] + T\Omega[-\beta \mathbf{F}_{BB} (.)^{-1} \mathbf{F}_{BB}^H \mathbf{F}_{RF}^H X d\mathbf{F}_{RF}] \end{aligned} \tag{3.29}$$

From the final expression in 3.29 where $(\frac{\partial f}{\partial \mathbf{F}_{RF}^x})^T = -\beta (X \mathbf{F}_{RF} \mathbf{F}_{BB} (.)^{-1} \mathbf{F}_{BB}^H)^T$, the expression for $\nabla_{\mathbf{F}_{RF}^*} f$ is given as

$$\frac{\partial f}{\partial \mathbf{F}_{RF}^x} = -\frac{\rho}{P_N} H^{total^H} \mathbf{H}^{total} \mathbf{F}_{RF} \mathbf{F}_{BB} (\mathbf{I}_{N_0} + \frac{\rho}{P_N} \mathbf{F}_{BB}^H \mathbf{F}_{RF}^H \mathbf{H}^{total^H} \mathbf{H}^{total} \mathbf{F}_{RF} \mathbf{F}_{BB})^{-1} \mathbf{F}_{BB}^H \tag{3.30}$$

Thus, algorithm 3.0 shows all steps of the hybrid precoder implemented

Algorithm 3.0 Hybrid Precoder Algorithm

1: **for** $t = 0, ...T-1$ **do**
2: Compute baseband precoder, $\mathbf{F}_{BB}$, using equation 3.21
3: Compute RIS matrix, Φ using equation 3.25
4: Compute the precoder matrix $\mathbf{F}_{RF}$ using equation 3.25
5: **end for**
6: Generate output precoder matrix $\mathbf{F} = \mathbf{F}_{RF} \mathbf{F}_{BB}$

3.4. Analog Precoder

Finally, with the problem solved regarding the minimization of the precoder matrices, it will be detailed the different architectures that can be implemented on the analog precoder, such as

- Unquantized Phase Shifter
- Quantized Phase Shifter
- Switches
- Antenna Selection
- Adjacent Dynamic Array of Subarrays
- Free Dynamic Array of Subarrays

The several structures to be implemented will be investigated by employing fully or partially connected RF chains, single or double phase shifters and their subsequent impact on the quality of the propagation signal, depending on the architecture in use.

3.4.1. Fully and Partially Connected Hybrid Design

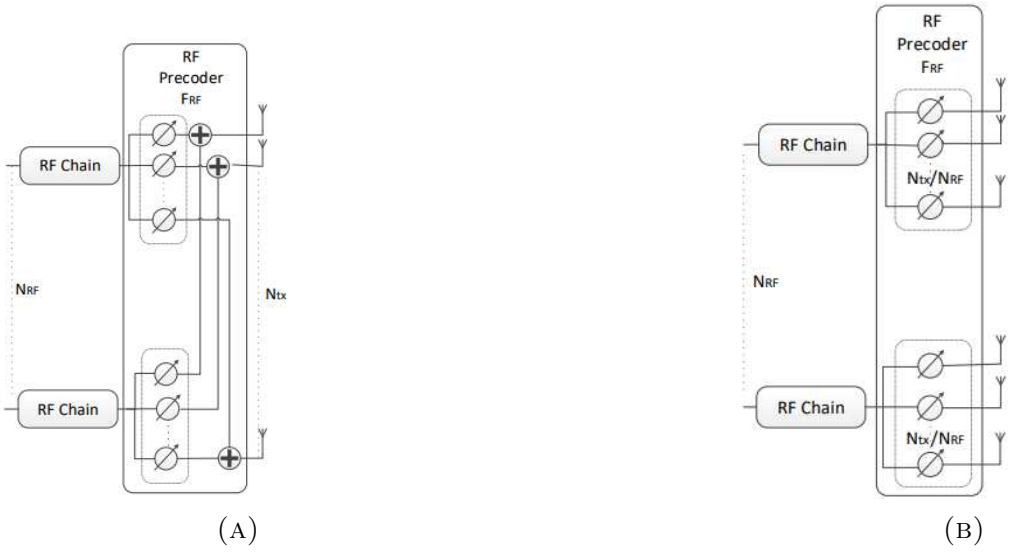

FIGURE 3.4. Hybrid Designs: Fully Connected structure 3.4a and Partially Connected structure 3.4b, retrieved from [**34**].

The fully connected (FC) hybrid design shown in figure 3.4a divides the signal coming from each RF chain into various phase shifters. Subsequently, the signal conveyed from each phase shifter from different RF chains is combined before its transmission in each antenna. The architecture with a fully connected design has an elevated hardware complexity in comparison with the partially connected structure.

The partially connected (PC) design, as shown in figure 3.4b, divides the signal from each RF chain towards the phase shifters in use. Each phase shifter is connected directly towards the transmission antenna.

3.4.2. Unquantized Phase Shifters (UPS)

The architecture that uses unquantized phase shifters can be considered a reference benchmark when comparing it to the structure that employs quantized phase shifters, since UPS employs phase shifters with an infinite resolution.

As a result, unquantized phase shifters provide a solution considered to be ideal and closer to the fully digital RIS architecture, applying a phase between $[0, 2\pi)$.

The UPS architecture will be implemented according to [**34**].

3.4.3. Quantized Phase Shifters (QPS)

Whilst UPS demonstrates an ideal solution, quantized phase shifters demonstrate a more real-life case since the number of phase shifts that can be implemented is finite. The phase shifters have N_b bits in use, each with 2^{N_b} phases available.

3.4.4. Double Phase Shifters (DPS)

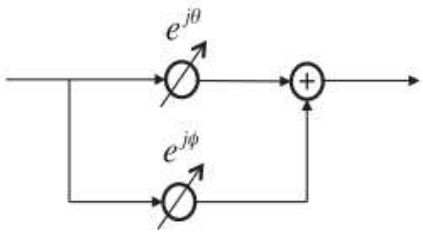

FIGURE 3.5. Double Phase Shifter configuration, retrieved from [**35**].

The analog RF precoder, whether it is using a fully connected or partially connected structure, can be implemented doubling the phase shifters in parallel, as seen in figure 3.5. Double phase shifting removes the restrictions placed on the modulus of the analog precoder matrix $\mathbf{F}_{RF}$, increasing the complexity of the analog component.

Double phase shifters generate a complex number where the final signal is expressed as [**35**]

$$c = s(e^{j\theta} + e^{j\sigma}) \tag{3.31}$$

the amplitude of the RF signals is adjusted by the phase shifters, consequently, the limitation seen on single phase shifters (SPS) regarding the maximum amplitude that was achieved can be surpassed with the implementation of DPS, increasing the amplitude to an interval between $[0, 2]$ [**36**].

The structure with DPS in use will be implemented according to [**34**].

3.4.5. Switches

Figure 3.6 demonstrates the structure of the RF precoder whilst using switches and its connection between the RF chain and the antennas.

The switches will determinate which antenna the signal will pass through. This case is more extreme in relation to the RF precoder with phase shifters, since not all antennas will be connected, thus affecting the efficiency of the transmitted signal.

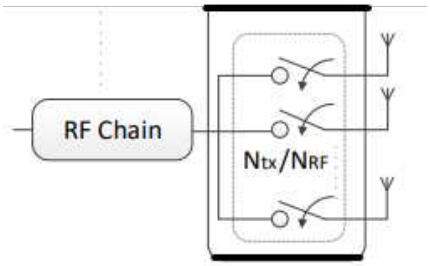

FIGURE 3.6. Structure employing switches, retrieved from [**34**].

The RF constraint and the implementation of the RF precoder will be followed according to [**34**].

3.4.6. Antenna Selection

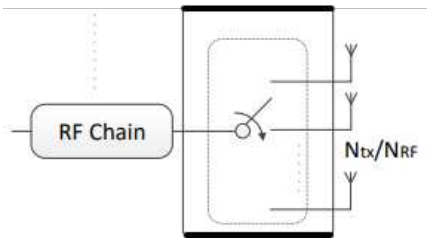

FIGURE 3.7. Antenna Selection scheme, retrieved from [**34**].

The hybrid architecture that employs antenna selection in the RF precoder, seen in figure 3.7, presents a lower complexity than the RF precoder that uses phase shifters. Amongst all the antennas connected per RF chain, the RF precoder will select only one antenna.

This structure presents an extreme case in comparison with the design that employs phase shifters due to the fact that only one antenna will be in use per RF chain. Even though the complexity is drastically reduced for employing only one antenna in each RF chain, the overall performance will be impacted significantly.

3.4.7. Array of Subarrays (AoSA)

The RF precoder that employs Array of subarray (AoSA) divides per the number of active RF chains a group of antennas, denominated as subarrays. The number of subarrays, N_{SA}, is set as $N_{SA} = N_{RF}$, the size of each subarray is given as $N_{SA,Tx} = \frac{N_{Tx}}{N_{SA}}$, thus it divides the number of transmitter antennas equally per each subset [**34**].

The complexity of AoSA architecture depends on the number of subarrays connected in each RF chain. In order to improve performance as well as have a manageable complexity, the number of subarrays is limited in each connection, denominated as L_{max}. When there is 1 subarray for each RF chain, the AoSA architecture in study corresponds to the partially connected structure, as seen in figure 3.4b.

Even though the AoSA architecture that will be analysed uses phase shifters, as seen in figure 3.4b, the AoSA structure can also implement switches or antenna selection on its RF precoder, represented in figure 3.8.

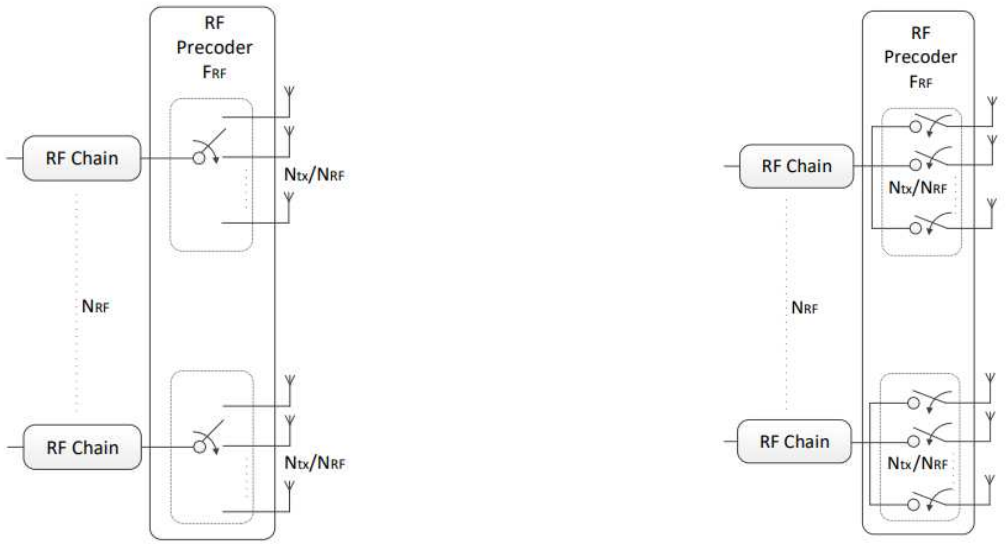

FIGURE 3.8. AoSA Hybrid Designs: (3.8a) Switches, (3.8b) Antenna Selection, retrieved from [**34**].

3.4.8. Dynamic Array of Subarrays (DAoSA)

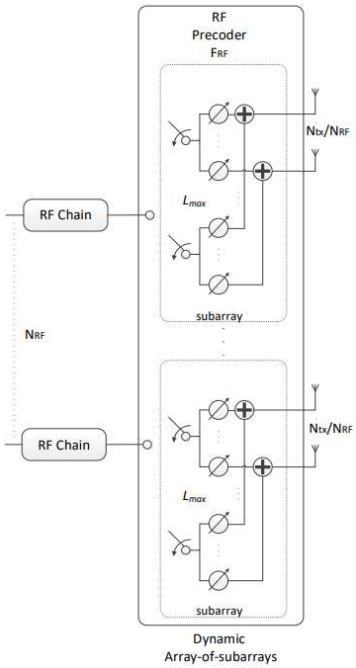

FIGURE 3.9. Hybrid architecture dynamic array of subarrays based on phase shifters, retrieved from [**34**].

Dynamic array of subarray is based on the AoSA design. Whereas in the structure utilizing AoSA each RF is directly connected to a subset of antennas via phase shifters or other method described above, the DAoSA structure, as seen in figure 3.9, links the RF chain to a switch, allowing the option of choosing which subset of antennas the RF chain

connects to. The existent transmitted antennas are divided per the existent RF chains, represented as L_t, therefore the number of switches is obtained through $\alpha_s = L_t^2$.

Moreover, DAoSA also allows choosing the number of subarrays that are connected in each RF chains, allowing different chains to have different numbers of transmit antennas, whilst AoSA divided the number of antennas equally per RF chain.

A dynamic AoSA design implemented in hybrid precoding allows a free and dynamic control since it does not have a fixed circuit, seen in AoSA and FC structure, thus offering better power consumption and higher spectral efficiency [**37**].

The hybrid precoder DAoSA studied will have two distinct designs:

- Adjacent Dynamic Array of Subarrays
- Free Dynamic Array of Subarrays

CHAPTER 4

Analysis and Discussion of Results

The results obtained in this paper were acquired through the development of a simulator in order to evaluate the performance of the algorithm that opmitizes the hybrid precoder and the RIS, derived in the previous chapter. Besides that, it will be analysed the impact of the different RF precoder architectures, regarding switches, phase shifters, AoSA, antenna selection or DAoSA.

4.1. Simulator

A simulator developed in Matlab, which is based on the Monte Carlo method in order to mimic an indoor environment scenario. Firstly, the parameters of the scenario the simulator will run are assigned by specifying the number of total symbols per transmission, N_s, the number of transmit antennas, N_{tx}, the number of receiver antennas N_{rx} and the number of elements in the RIS, N_{RIS}. Then, it is selected the frequency in which the channel will operate in by attributing the frequency, f, and the corresponding bandwidth, B.

The path loss exponent between each link existent, transmit-to-receiver, transmit-to-RIS and RIS-to-receiver is obtained through [**38**] where the frequency that deployed in the simulation will determine the path loss the mmWave/THz channel will suffer.

Regardless of the scenario in use, certain parameters were not changed, such as the rice factor, $K_{rice} = 10$, bandwidth $B = 8$ GHz, retrieved from [**38**], the distance between adjacent antenna elements in the transmitter, d_{Tx}, in the RIS, d_{RIS}, and in the receiver, d_{Rx}, which were assumed to be $d_{Tx} = d_{Rx} = d_{RIS} = 0.0054$ m. Thus the area of each RIS element is $A_{RIS} = d_{RIS}^2$.

4.2. Study of Achievable Rate with variable Distance for 28 GHz

The first scenario is configured with a frequency $f = 28$ GHz to evaluate the differences as well as similarities that may exist between a frequency set in the mmWave band and the RIS effect on radio propagation among Tx-Rx, in comparison to the scenario implemented further along using a frequency in the THz band.

As the frequency chosen uses the mmWave frequency band, it will offer better coverage, thus the achievable rates will also increase, regardless of the hybrid precoder in use.

In order for the transmission to be possible and to generate a mmWave channel, according to [**38**], the path loss exponent (PLE) between the transmitter and receiver for $f = 28$ GHz is defined as $n_{Tx-Rx} = 4.4$, the PLE for $n_{Tx-RIS} = n_{RIS-Rx} = 1.9$. The antenna array considered between the Tx and Rx will be UPA, Uniform Planar Array,

and the number of NLoS signal paths is set to 10. The array type in use will determine the number of RIS elements that can be implemented.

The coordinates of the BS, RIS array and the user are defined as (0,0), (2 m,2 m) and (d,0), respectively, where d represents the distance spanning [0:3:40] meters between Tx and Rx.

In this scenario, the frequency chosen offers better coverage range, thus i is reasonable to assume the existence of a path between Tx-RIS-Rx activated as well as the direct path between the Transmitter and Receiver. The simulation will study the achievable rates depending on the paths in use and compare them regarding the number of antennas and RIS elements deployed.

Firstly, it is simulated the designs that do not employ hybrid precoder achitectures, such as simple reflectarrays and Alternating Minimization with non monotone Accelerated Proximal Gradient for Precoder and RIS (AM-APG), seen in figure 4.1.

The simple reflectarray structure models the worst-case scenario due to the fact that even though this algorithm uses a fully digital SVD precoder, it also employs a fixed RIS, that functions as simple mirror since it will only blindly reflect the carrier signal.

The AM-APG algorithm, based on the proposed accelerated proximal gradient (APG) jointly to all RIS matrices, is a version of the algorithm presented in chapter 3 where it will automatically compute the digital precoder matrix $\mathbf{F}$, since there is no $\mathbf{F}_{RF}$ matrix. The AM-APG will provide the best case scenario, since the algorithm employs fully digital precoder and RIS structure.

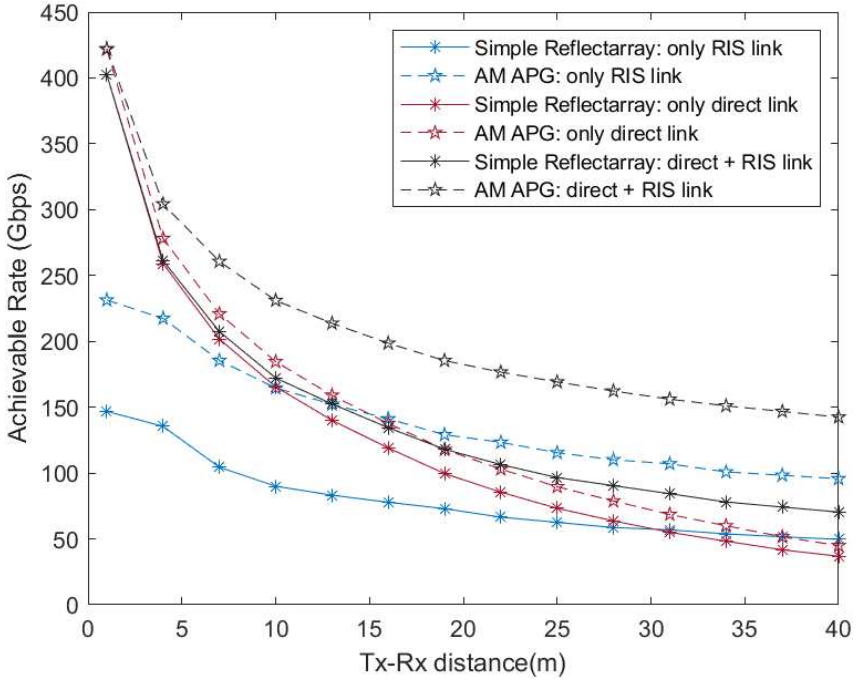

FIGURE 4.1. Study of Achievable rate (Gbps) using simple reflectarrays and AM-APG for $N_{RIS} = 256$, whilst increasing the distance between Tx and Rx.

When the simple reflectarray is in use , the activation of the direct link improves the achievable rate significantly in the first few meters, going from 502.5 to 261.294 Gbps on the first 4 meters. On the other hand, the rate the simple reflectarray produces with having only the RIS link activated goes from 146.8 to 135.4 Gbps in the first 4 meters.

As the coverage area increases, the scenario with only the direct link activated worsens in comparison with the RIS link after the 31 meter mark achieving 55 Gbps.

The fully digital RIS seen in figure 4.1, when only the RIS link is activated, goes from 231 Gbps to 217.463 Gbps in the first 4 meters. When it has both links activated the initial rate goes from 422.228 Gbps to 304.336 Gbps on the first 4 meters of distance between Tx-Rx. However when it only has the direct link activated the initial rate is the same, 422.228 Gbps, although when the distance from the Tx to Rx increments to 16 meters it starts to present worse rates that the scenario where only the RIS link was in use. This is due to the fact that the LoS component for the direct link, $\mathbf{H}_{LOS}^{D,S}$, is null.

Comparing both RIS types, simple reflectarray and AM-APG, as well as the three different scenarios, all represented on figure 4.1, the use of the direct and the RIS link simultaneously present the best coverage range overall. The greater the distance between Tx and Rx is, the usage of only the RIS link will have better rates than the ones obtained through using solely the direct link. The direct link is beneficial solely when the distance between the transmitter and receiver antennas are smaller than 13 meters using AM APG, and smaller than 28 meters for simple reflectarrays since it records better coverage.

4.2.1. Hybrid Precoders

The following figure 4.2 demonstrates varied hybrid precoders designs, either fully or partially connected, using 3 bit quantization for 256 RIS elements and both RIS and direct link activated.

The AM-APG curve is used as a benchmark in order to evaluate the performance of different hybrid precoders. The simple reflectarray also provides perspective in order to assess how a fully digital SVD precoder and a blind RIS are in comparison with an hybrid precoder.

The hybrid precoder that employs switches presents the lowest performance, followed by the curves that represent the design that applies antenna selection. The curve obtained with simple reflectarray presents better coverage range than the curve from the switches throughout the 40 meters of distance. Comparing the simple reflectarray and antenna selection curves, the simple reflectarrays display better rates up to 19 meters of distance registering 118 Gbps. When the distance is bigger than 19 meters, the simple reflectarrays offer an achievable rate similar to the one acquired using antenna selection when the distance between Tx-Rx is increased.

Unquantized phase shifters have the best coverage range out of all hybrid precoders deployed in figure 4.2 with 400 Gbps in 1 meter of distance and 163 Gbps halfway through the interval between the BS and the user.

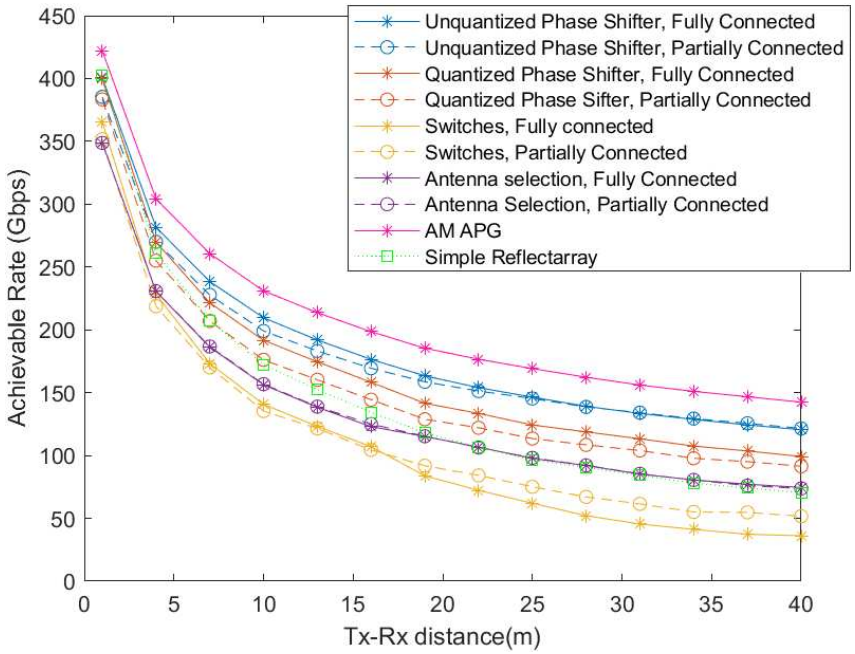

FIGURE 4.2. Study of Achievable rate (Gbps) for different hybrid precoders for $N_{RIS} = 256$, direct + RIS link in use.

Figures 4.3 and 4.4 represent the simulation for various hybrid precoders designs using only the RIS link with 256 RIS elements for fully connected and partially connected hybrid designs, respectively.

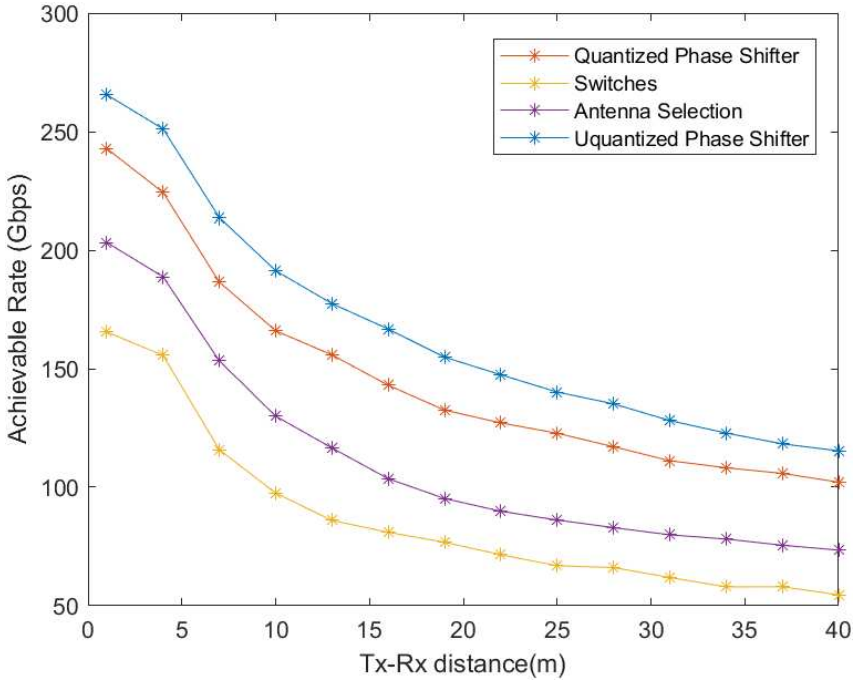

FIGURE 4.3. Study of Achievable rate (Gbps) for different fully connected hybrid precoders for $N_{RIS} = 256$, with only RIS link in use.

As seen in figures 4.3 and 4.4, the use of unquantized and quantized phase shifters offer the best coverage range. The switches, the most extreme hybrid design being tested,

provide the worst rates throughout the increment of the distance between the transmitter and end user.

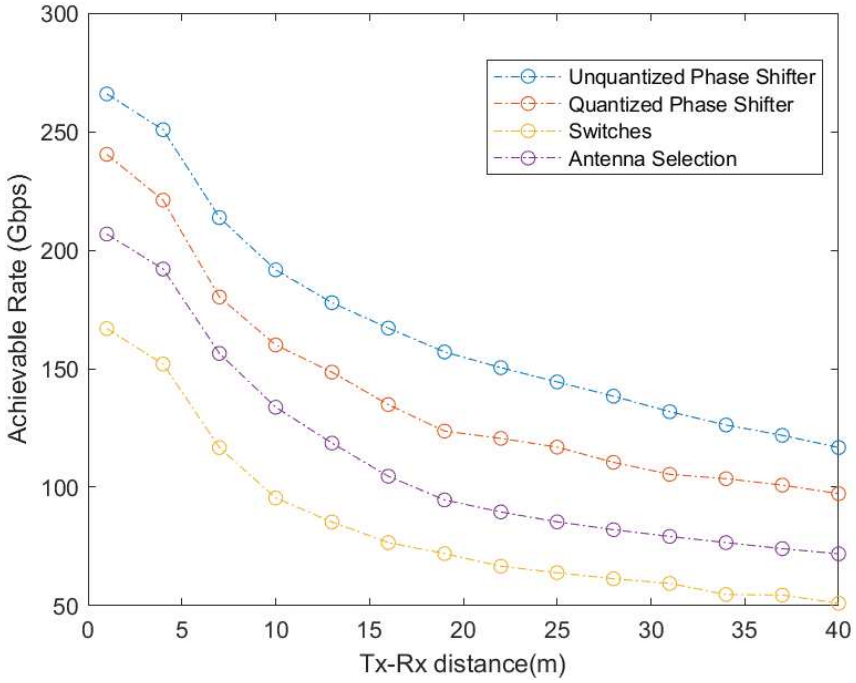

FIGURE 4.4. Study of Achievable rate (Gbps) for different partially connected hybrid precoders for $N_{RIS} = 256$, with only RIS link in use.

Comparing the architectures that employ fully connected, represented in figure 4.3, or partially connected designs, seen in figure 4.4, the unquantized phase shifters achieve similar rates in the first 4 meters for fully or partially connected, attaining 251.1 Gbps and 250.8 Gbps, respectively. When the distance is increased to 25 meters the unquantized phase shifter partially connected offers better coverage range, 144.4 Gbps than when it is fully connected, 140.1 Gbps. The quantized phase shifters fully connected achieve 224.3 Gbps when the distance between the transmitter and receiver is only 4 meters and 122.8 Gbps when it increases to 25 meters. The quantized phase shifter partially connected obtains lower rates for the same distances, 221 Gbps and 116.9 Gbps for 4 meters and 25 meters, respectively. Thus, the hybrid precoder that employs quantized phase shifter fully connected offers better coverage range comparatively to partially connected.

4.2.2. Dynamic Array of Subarray

The hybrid precoder free dynamic array of subarray is represented in figure 4.5 with only the RIS link activated for different RIS elements.

Figure 4.5 shows that regardless of the number of RIS elements in use, the curves that use more than 1 subarray per RF chain do not have higher achievable rates in comparison with those that only employ one subarray per RF chain. As the interval where the different curves are being analysed is relatively small, the differences between curves for the same number of RIS elements are virtually nonexistent. This behaviour is a result of

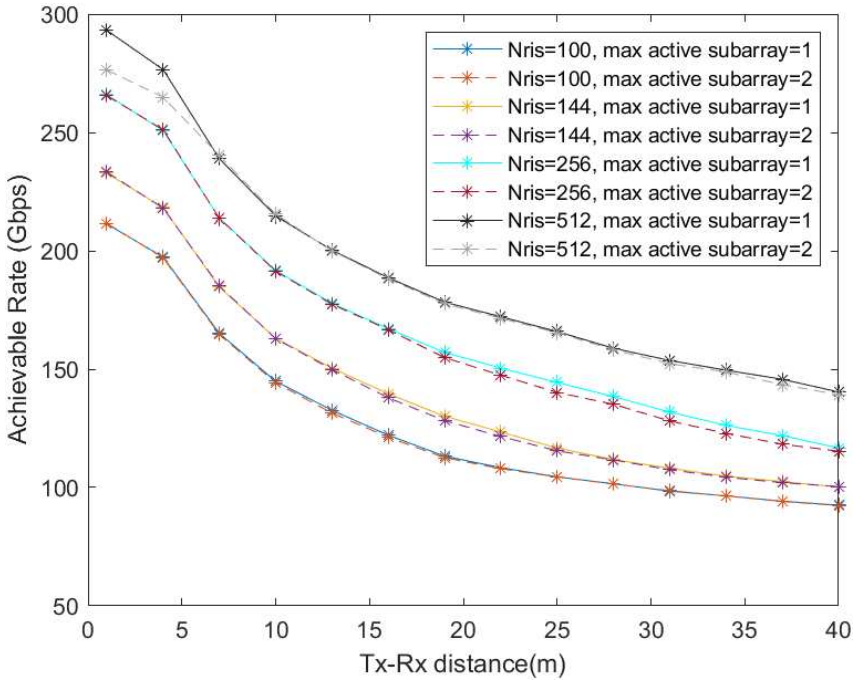

FIGURE 4.5. Study of Achievable rate (Gbps) for free dynamic AoSA using different RIS elements, with only RIS link in use.

the number of symbols being transmitted, as well as the current channel configuration in use.

Thus, the number of transmit and receiver antennas can be shortened as having the frequency $f = 28$ GHz does not need an elevated number of receiver and transmitter antennas that were previously in use. As a result, it will also reduce its costs on implementation as it lowers its complexity.

In the following figure 4.6, it is demonstrated several simulations for free dynamic array of subarrays using $N_{RIS} = 144$ and a varied number of N_{Tx} and N_{Rx} antennas with only the RIS link activated.

When the number of transmit antennas are reduced to 144 instead of 512, as demonstrated in figure 4.6 that employs $N_{RIS} = 144$, the achievable rate in the first 4 meters is higher for the curve that employ 2 subarrays in each RF chain, going from 152.7 Gbps to 142.4 Gbps, whereas for 1 subarray per RF chain goes from 143.5 Gbps to 134.8 Gbps. When the distance is increased the curves present similar rates, regardless of the number of subarrays in use. The achievable rate seen with $N_{Tx} = 512$ and $N_{Rx} = 36$ within the first 10 meters goes from 214.5 Gbps to 153.4 Gbps when there is only 1 subarray per RF chain. These values are similar to those obtained with 2 active subarrays, going from 212.9 Gbps to 151.3 Gbps.

When the number of RIS elements in use is increased to 256 and the number of transmit and receiver antennas are 144 and 16 or 256 and 36, seen in figure 4.7, the behaviour is similar to the one depicted in figure 4.6 for the same number of N_{Tx} N_{Rx}. Thus, the number of antennas affects how the achievable rate is dependent or not on the number of subarrays connected in each RF chain.

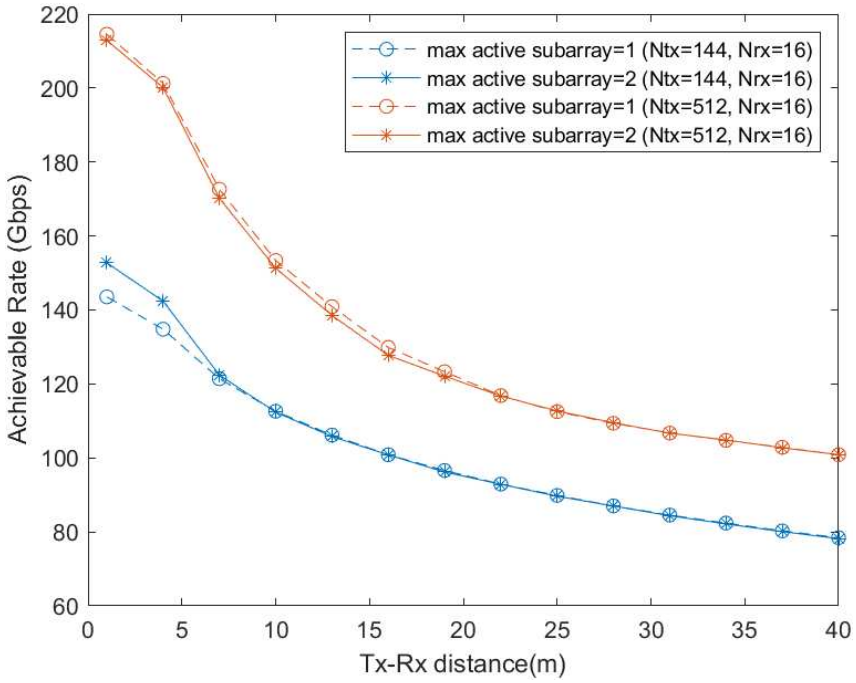

FIGURE 4.6. Study of Achievable rate (Gbps) for free dynamic AoSA using different Tx and Rx antennas for $N_{RIS} = 144$, with only RIS link in use.

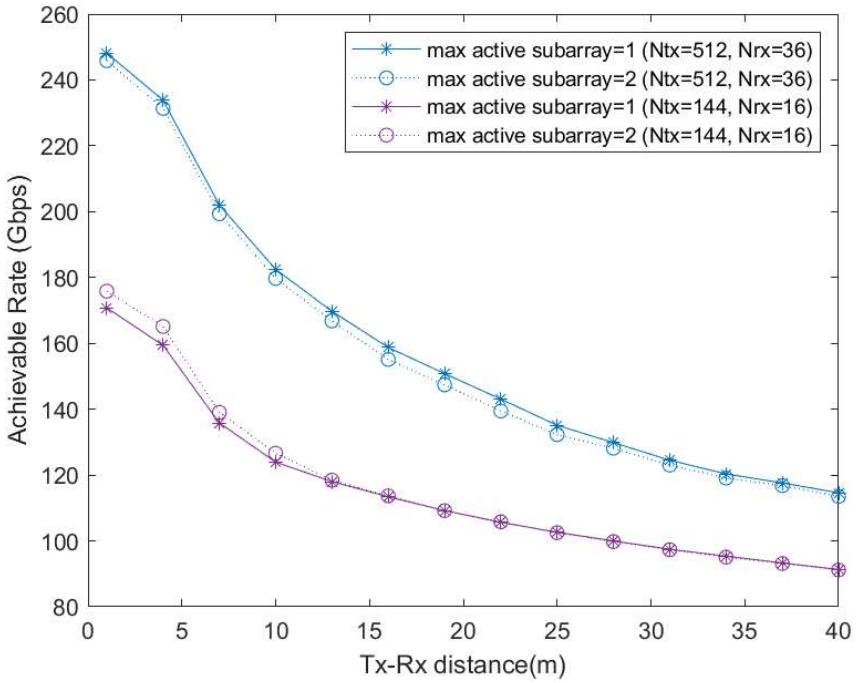

FIGURE 4.7. Study of Achievable rate (Gbps) for free dynamic AoSA using different Tx and Rx antennas for $N_{RIS} = 256$, with only RIS link in use.

Whilst figure 4.6 only had the RIS link activated, the figure 4.9 has both the RIS and the direct link activated. In both figures it is tested the achievable rate using free dynamic AoSA and how different subarrays in use on RF chains affect the rate depending on the number of antennas for 144 RIS elements.

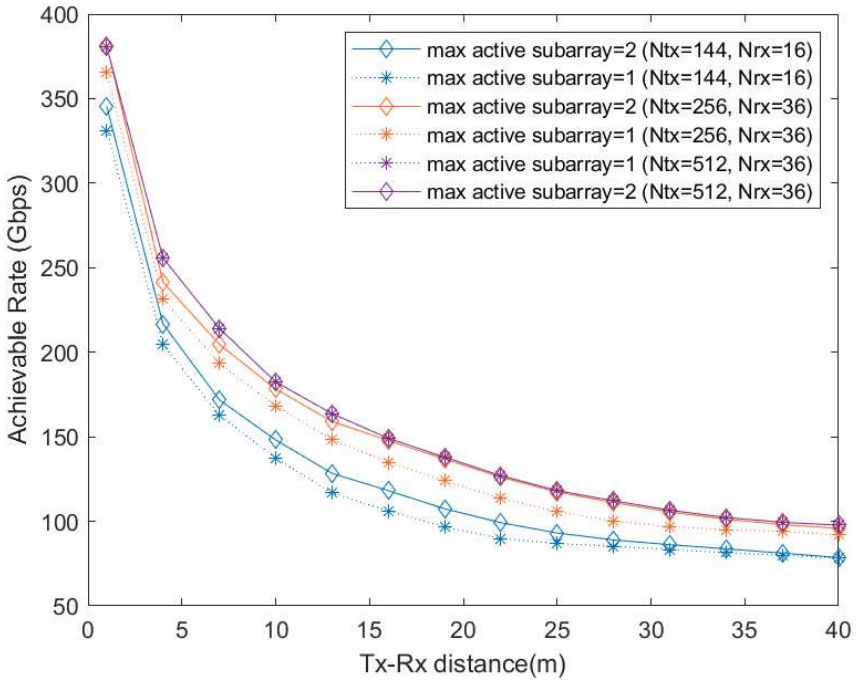

FIGURE 4.8. Study of Achievable rate (Gbps) for free dynamic AoSA using different Tx and Rx antennas for $N_{RIS} = 144$, with both the RIS and direct link in use.

The figure with both links activated, figure 4.8, shows how advantageous having more than one subarray per RF chain is when the number of antennas for the transmitter and receiver are scaled down, since the frequency being used, 28 GHz, is reduced as well. For $N_{Tx} = 144$ and $N_{Rx} = 16$ the initial achievable rate goes from 331.2 Gbps to 137.4 Gbps in its first 10 meters of distance from Tx to Rx when there is one subarray per chain. When the number of active subarrays is increased to its double, within the same distance the rate goes from 345.2 Gbps to 148.1 Gbps.

When the number of antennas is changed to $N_{Tx} = 512$ and $N_{Rx} = 36$ the curves for 1 or 2 subarrays active per RF chain seen in figure 4.8 are equivalent. The initial rate goes from 380.6 Gbps to 182.4 Gbps in the first 10 meters of distance.

Comparing both figures 4.8 and 4.6, it is concluded that when the distance between the BS and the user is reduced, the use of both links is more beneficial since it provides better rates. However, for bigger distances between Tx-Rx, such as over 31 meters, the connection with only the RIS link activated offers similar coverage range as the connection using direct and RIS link simultaneously, as seen in figure 4.9, due to the fact that the simulation effect will always generate variance that impacts the precision of the simulation.

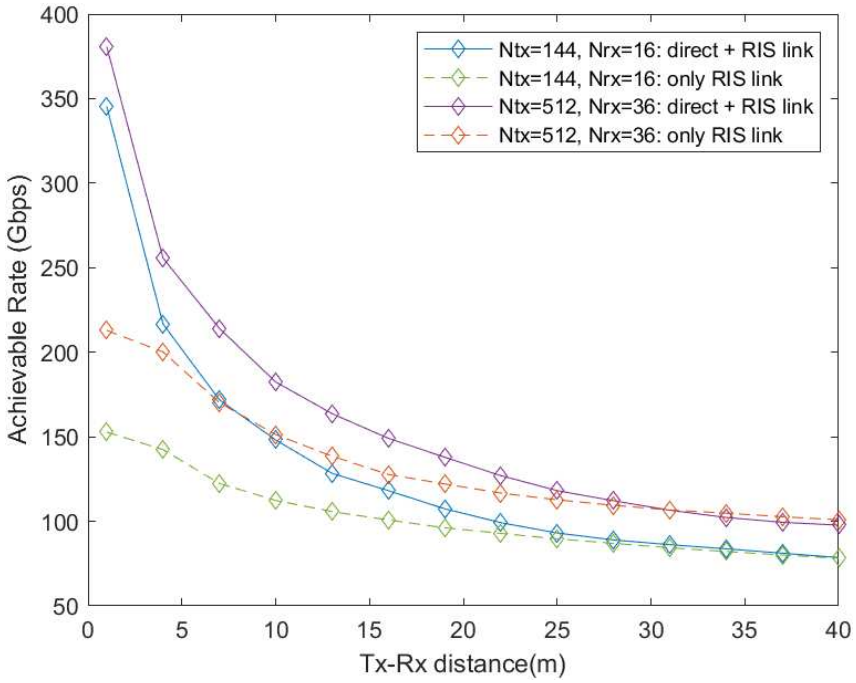

FIGURE 4.9. Study of Achievable rate (Gbps) for free dynamic AoSA using different Tx and Rx antennas for $N_{RIS} = 144$, and for different links in use.

4.3. Study of Achievable Rate with variable Transmitter Power for 28 GHz

In this section, it is studied how the achievable rate is influenced by the transmitter power in use depending on the distance that the RIS finds itself between the transmitter and receiver. The closer the RIS is stationed to the base station, or the user, the achievable rate will be improved for the transmitted power that is being deployed.

The following figures 4.10 - 4.15 are configured for a frequency of $f = 28$ GHz, $N_s = 2$, $N_{Tx} = 144$, $N_{Rx} = 16$, with the distance between Tx-Rx fixed to 10 meters, using the following coordinates for the transmitter (0,0) and for the receiver (10 m,0). The transmitted power will range between [0:4:40] dBm.

The position of the RIS will vary in order to study how the achievable rate will evolve depending on its position between the transmit and receiver antennas. Firstly, the RIS will be positioned 1m from the transmitter, secondly halfway between the transmitter and receiver, and finally it is placed 1 meter from the receiver.

Figure 4.10 describes the curves for different numbers of RIS elements employed using a hybrid precoder with unquantized phase shifters and fully connected, whilst figure 4.11 studies the achievable rate using free dynamic array of subarrays. In both of these figures, the RIS is stationed within 1 meter of distance of the transmitter antennas, where its coordinates will be $(\frac{\sqrt{2}}{2}\text{m}, \frac{\sqrt{2}}{2}\text{m})$, with only the RIS link activated.

Figures 4.12 and 4.13, use the same hybrid precoder architectures deployed in figures 4.10 and 4.11, respectively, with also only the RIS link activated, however the RIS is stationed 5 meters from the transmitter as well as the receiver, using the coordinates $(\frac{5\sqrt{2}}{2}\text{m}, \frac{5\sqrt{2}}{2}\text{m})$.

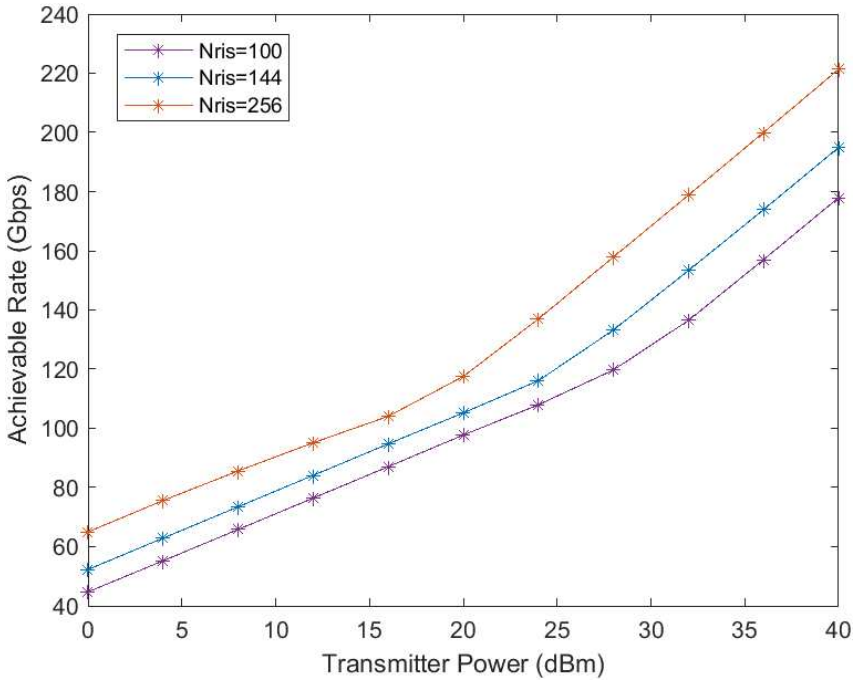

FIGURE 4.10. Study of Achievable rate (Gbps) for Unquantized Phase Shifters fully connected whilst increasing the transmitter power between Tx and Rx, for Tx-Rx=10 m and RIS 1 m from Tx, only RIS link in use.

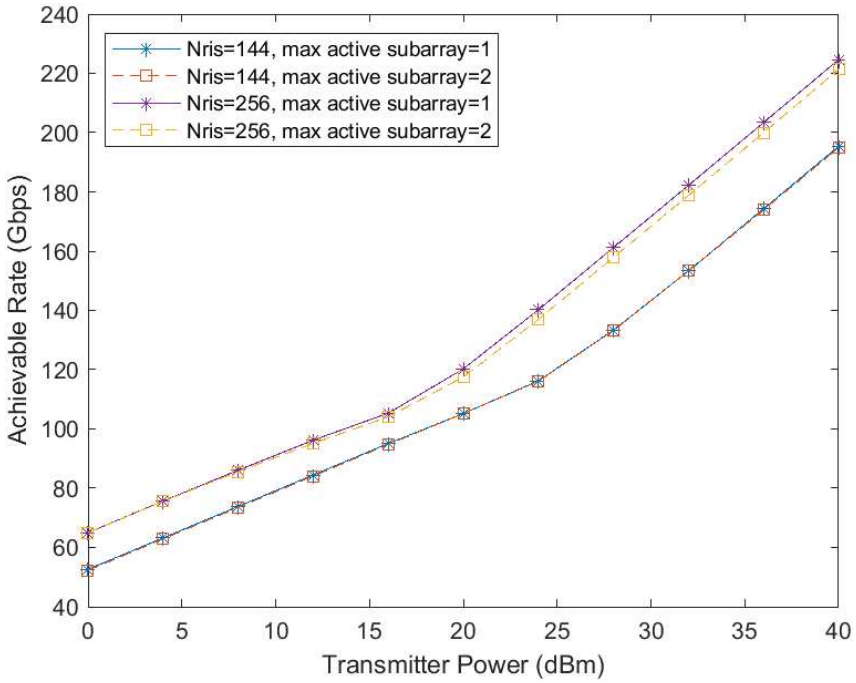

FIGURE 4.11. Study of Achievable rate (Gbps) for free dynamic AoSA whilst increasing the transmitter power between Tx and Rx, for Tx-Rx=10 m and RIS 1 m from Tx, only RIS link in use.

Finally, when the RIS is situated 1 meter of distance from the receiver, $(\frac{10-\sqrt{2}}{2}\text{m}, \frac{\sqrt{2}}{2}\text{m})$, the hybrid precoder unquantized phase shifter and free dynamic AoSA, as represented in figures 4.14 and 4.15, respectively.

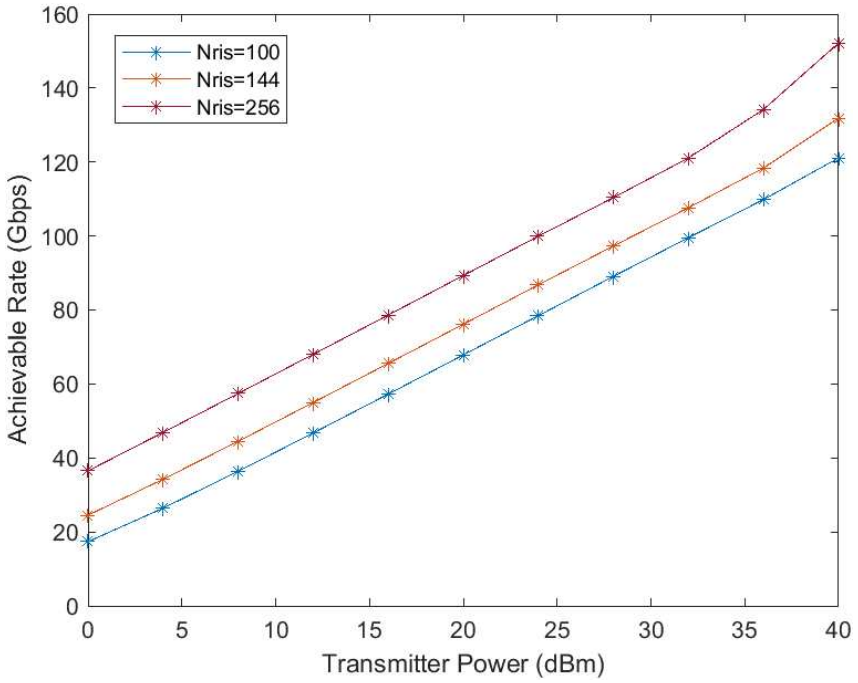

FIGURE 4.12. Study of Achievable rate (Gbps) for Unquantized Phase Shifters whilst increasing the transmitter power between Tx and Rx, for Tx-Rx=10 m and RIS 5 m from Tx, only the RIS link activated.

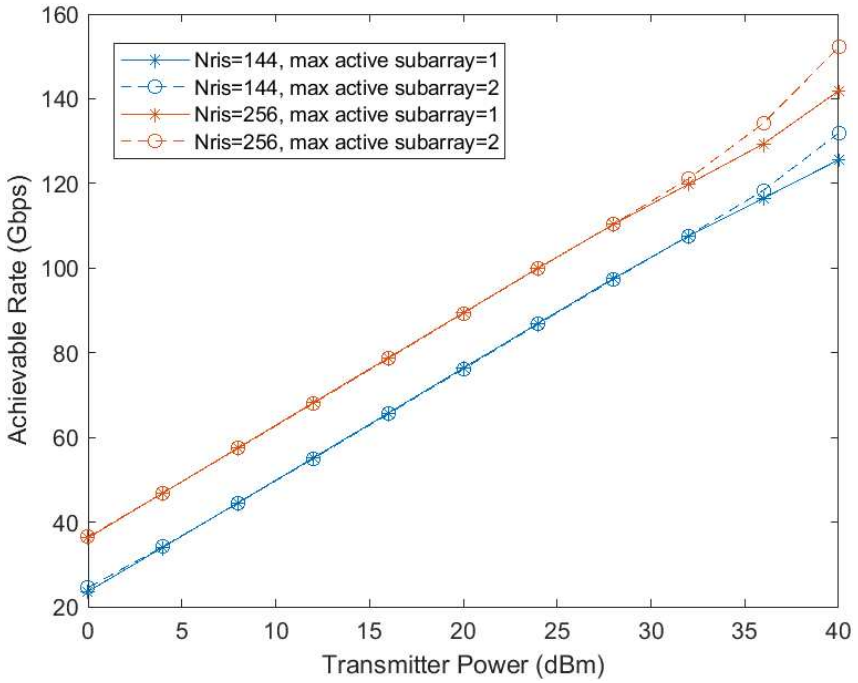

FIGURE 4.13. Study of Achievable rate (Gbps) for free dynamic AoSA whilst increasing the transmitter power between Tx and Rx, for Tx-Rx=10 m and RIS 5 m from Tx, only the RIS link activated.

Comparing all hybrid precoders that use unquantized phase shifters fully connected, represented in figures 4.10, 4.12 and 4.14, where the RIS is positioned in different locations, it is concluded that the achievable rate is higher the closer the RIS is stationed to the

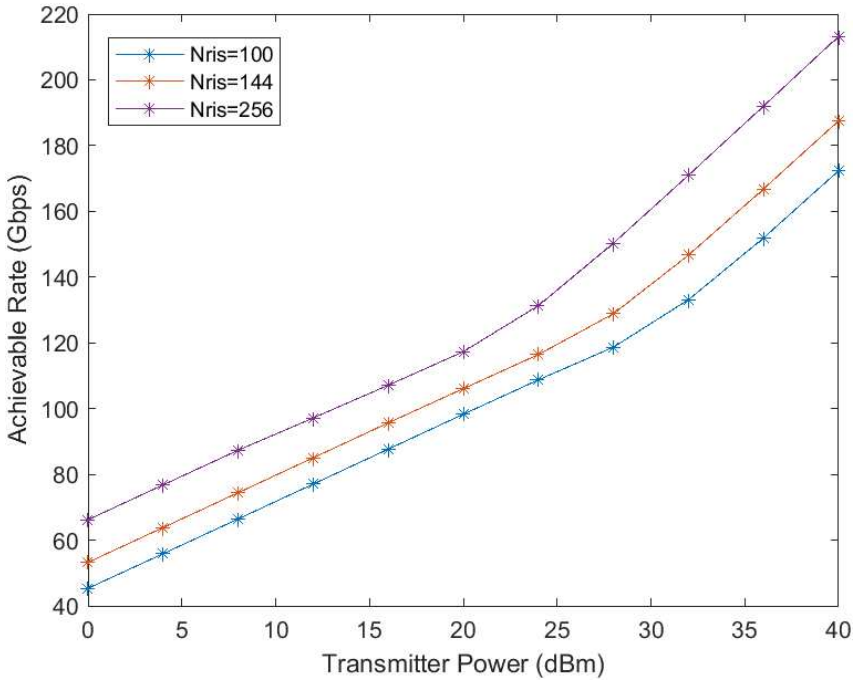

FIGURE 4.14. Study of Achievable rate (Gbps) for Unquantized Phase Shifters fully connected, for Tx-Rx=10 m and RIS 1 meter from Rx, only the RIS link activated.

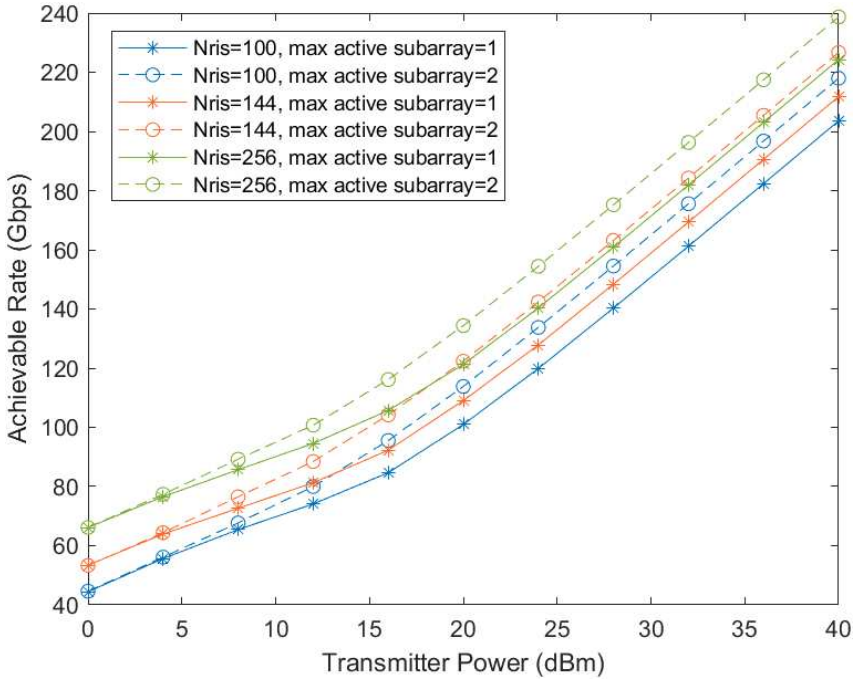

FIGURE 4.15. Study of Achievable rate (Gbps) for free dynamic AoSA for Tx-Rx=10 m and RIS 1 meter from Rx, only the RIS link activated.

transmitter or the receiver antennas. For $N_{RIS} = 256$ and $P_{Tx} = 20$ dBm the achievable rate for the RIS positioned 1 meter from the transmitter is 117.5 Gbps, when it is 5 meters from the transmitter it is 89.3 Gbps, and for 1 meter of distance from the receiver it records 117.315 Gbps. These values change for higher transmitter power, $P_{Tx} = 30$

Gbps, achieving 179 Gbps, 121.1 Gbps and 171 Gbps, respectively. Therefore, figure 4.10 shows the best results while figure 4.12 demonstrates lower curves.

As a result, the farther the RIS finds itself to either one of the antennas, transmitter or receiver, the achievable rate will decrease. Alternately, it is favorable to settle the RIS near the base station or the receiver.

Figures 4.11, 4.13 and 4.15 present the achievable rate depending on the position of the RIS between Tx-Rx, using a hybrid precoder with free dynamic array of subarray with 1 or 2 subarrays per RF chain. When the RIS is 1 meter of distance from the transmitter, figure 4.11, the curves for the $N_{RIS} = 144$ using 1 or 2 subarrays in each RF chain achieve the same result. When the number of RIS elements is increased, the curves with different subarrays do not overlap each other, however it shows that using more than 1 subarray does not offer an advantage when the RIS is stationed so close to the Tx, performing lower when the transmitter power is increased.

When the distance between RIS and Tx is increased to 5 meters, as seen in figure 4.13, the curves show lower achievable rates, and for $N_{RIS} = 144$ the curves are identical for 1 or 2 active subarrays up to 32 dBm where it records 107 Gbps.

The changes for the number of subarrays employed are noticeable when the distance between the RIS and the receiver is 1 meter, as seen in figure 4.15. The curve that represents 2 subarrays with $N_{RIS} = 100$ offers better results in comparison with the curve with only 1 subarray with $N_{RIS} = 144$. The same behaviour is noticeable between 144 and 256 RIS elements.

4.3.1. Direct + RIS link activated

When both the direct and RIS link are activated, the achievable rate will improve significantly, in comparison with the rates observed when only the RIS link was in use, as seen in figures 4.16, 4.17 and 4.18.

As shown in figure 4.16, the use of direct and RIS link simultaneously offers better rates whilst increasing the transmitter power being used. When both links are activated, for $P_{Tx} = 20$ dBm and $N_{RIS} = 144$, the achievable rate is 122.5 Gbps, whilst when only the RIS link activated is 105.2 Gbps. When the transmitter power is increased to $P_{Tx} = 32$ dBm the difference between the rates increases, achieving 184.6 Gbps and 153.3 Gbps, respectively. Moreover, when the number of RIS elements is increased to $N_{RIS} = 256$, the difference between both curves achieved is similar throughout the increment of transmitter power, recording for $P_{Tx} = 20$ dBm 117.5 Gbps and 132.8 Gbps for only the RIS link and both the direct and RIS link, and for $P_{Tx} = 32$ dBm an increase to 178.8 Gbps and 195 Gbps, subsequently.

Appendix C presents results for unquantized phase shifters fully connected for different positions of the RIS, when it is 5 meters of distance from the Tx, figure C.1, and 1 meter from the Rx.

Figures 4.17 and 4.18 describe the curves for different RIS elements using only the RIS link or the direct link conjoined with the RIS link, for the hybrid precoder free dynamic

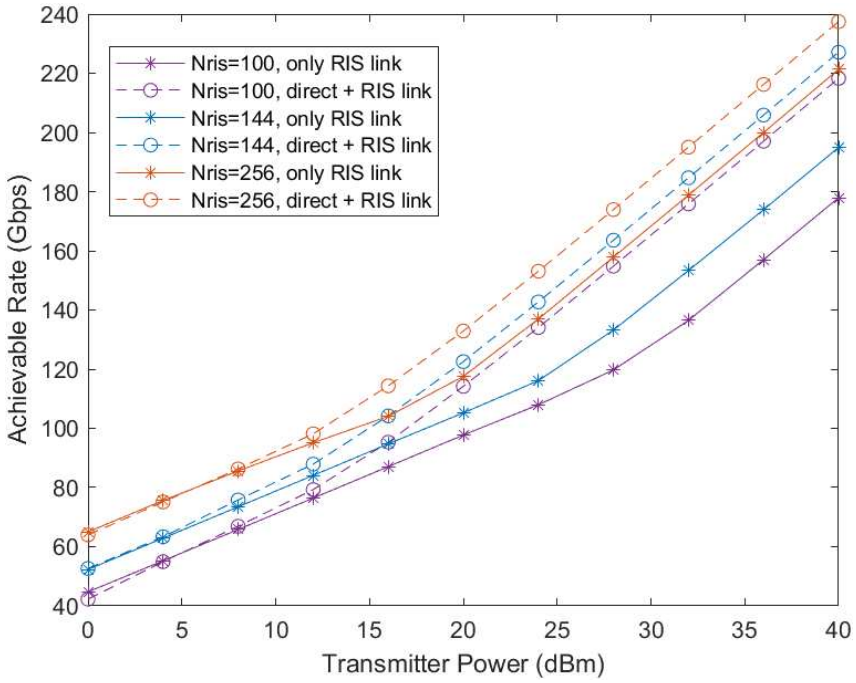

FIGURE 4.16. Study of Achievable rate (Gbps) for Unquantized Phase Shifters fully connected, for Tx-Rx=10 m and RIS 1 m from Tx, comparing only RIS link and direct + RIS link.

array of subarrays. Figure 4.17 represents the results using only 1 subarray per RF chain, while figure 4.18 has 2 subarrays activated for each RF chain.

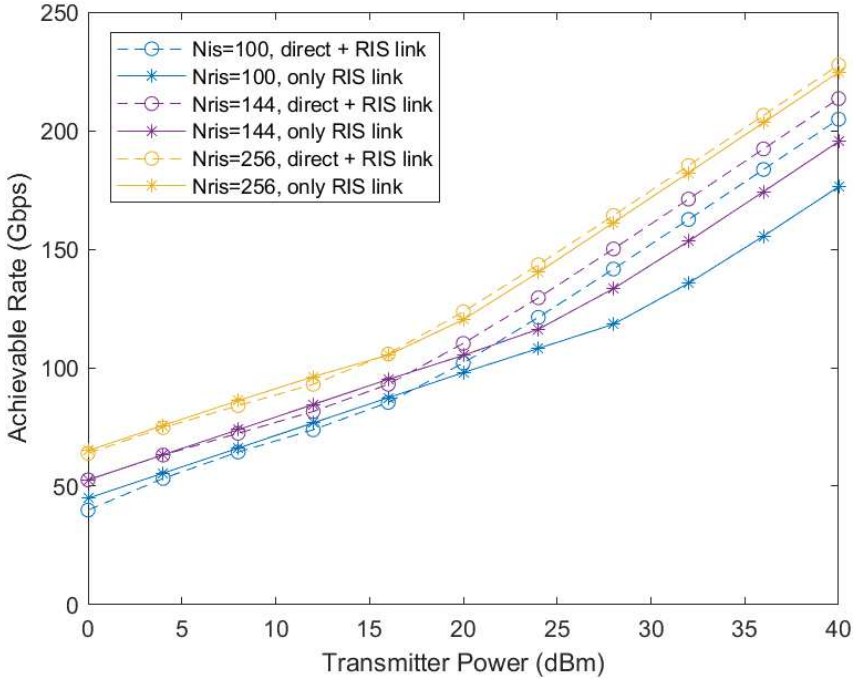

FIGURE 4.17. Study of Achievable rate (Gbps) for free dynamic AoSA using 1 subarray per RF chain, for Tx-Rx=10 m and RIS 1 m from Tx, comparing only RIS link with direct + RIS link.

Analysing for $N_{RIS} = 144$ and $P_{Tx} = 20$ dBm, in figure 4.17, the achievable rate is 105.2 Gbps for only the RIS link activated, and 110.26 Gbps for both links in use. When the power is increased to 32 dBm, the rate changes to 153.3 Gbps and 171.1 Gbps, respectively. Moreover, the curves that employ 2 subarrays in each RF chain, represented in figure 4.18 for the same parameters, it has higher results whilst the direct and RIS link are both in use, achieving 122.5 Gbps and 184.6 Gbps when the transmitter power is 20 dBm and 32 dBm, respectively. The curve with only the RIS link activated has the same results as those obtained with only 1 subarray connected to each RF chain.

In appendix C, figures C.3 and C.4, compare for different subarrays deployed, how the achievable rate is affected when the RIS finds itself in different positions.

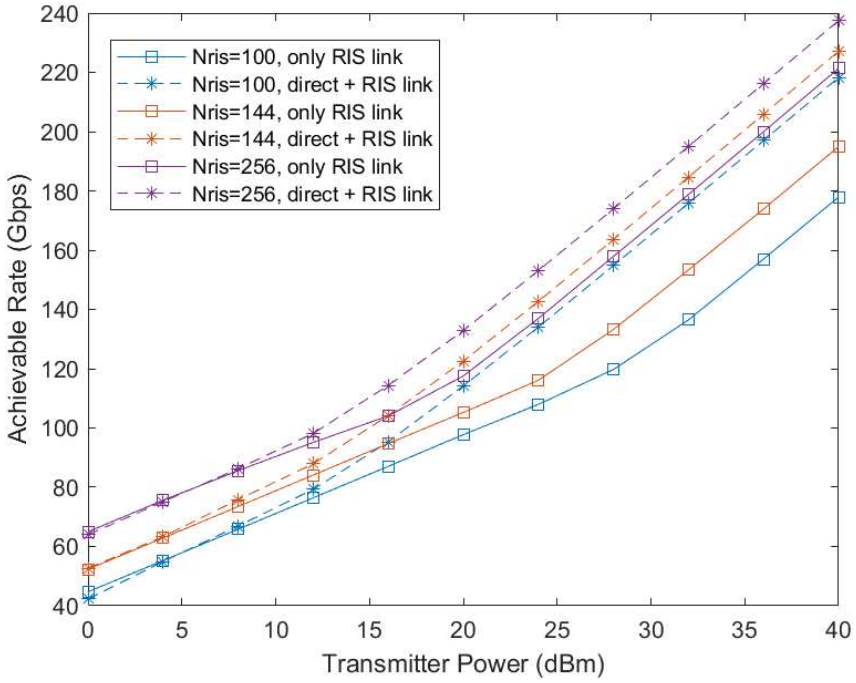

FIGURE 4.18. Study of Achievable rate (Gbps) for free dynamic AoSA using 2 subarrays per RF chain, whilst increasing the transmitter power between Tx and Rx, for Tx-Rx=10 and RIS 1 m from Tx, comparing direct and direct + RIS link.

Thus, when using free dynamic AoSA it is advantageous to employ several subarrays when both links are in use.

4.4. Study of Achievable Rate with variable Distance for 300 GHz

When a higher frequency band is in use, the coverage range provided will be significantly lower, thus certain parameters need to be changed.

The frequency studied in the previous section belongs to the mmWave band that is already used in 5G. However, as the main focus is to deploy a THz band in order to enable communications in 6G, the frequency will need to be increased closer to the THz band.

The second scenario in use has the frequency set to $f = 300$ GHz, and will only have the indirect path active, Transmitter-RIS-Receiver. Path loss exponent between Tx and

RIS is equal to the path loss between RIS and Rx, equaling $n_{Tx-RIS} = n_{RIS-Rx} = 2.05$, retrieved from [**38**]. The coordinates of the BS, RIS array and the user are defined as (0,0), (2 m,2 m), and (d,0), respectively, where d represents the distance between Tx-Rx. The number of NLoS signal paths is set to 3.

The following figures from 4.19 to 4.31 show the results for a scenario with $N_{Rx} = 36$, $N_{RIS} = 512$, $N_s = 2$ and $N_{Tx} = 512$, with no direct path between the transceiver and receiver.

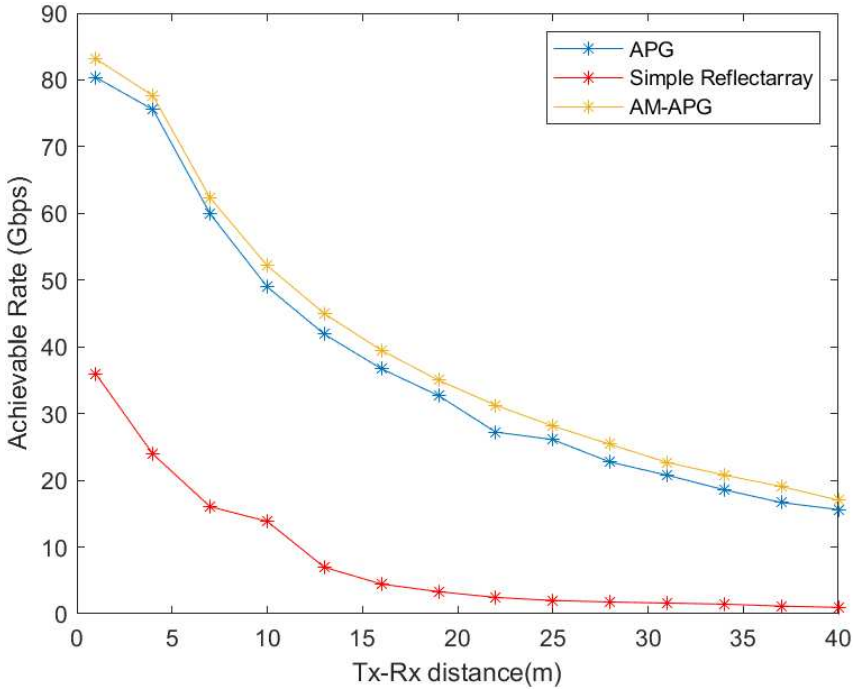

FIGURE 4.19. Achievable rate versus distance between Transmitter and Receiver for APG, AM-APG and Static Reflectarray algorithms.

Figure 4.19 compares the achievable rate (Gbps) whilst increasing the distance between the transmitter and receiver using APG [**25**], AM-APG and simple reflectarray algorithms.

The algorithm that was based on APG and employs a fully digital precoder matrix (AM-APG) has the best achievable rates, going from 83 Gbps to 77 Gbps in the first four meters. The proposed accelerated proximal gradient algorithm jointly to all RIS matrices (APG) has slightly lower curve in comparison to the curve obtained with AM-APG in figure 4.19, having an achievable rate of 80 Gbps in the first meter and 75.5 Gbps when the distance between Tx-Rx is four meters. The simple reflectarray demonstrates the worst-case scenario, having an achievable rate going from 36 to 24 Gbps in the first four meters. When this distance is increased to 22 meters the simple reflectarray has an achievable rate of 2.4 Gbps while AM-APG has 31.2 Gbps.

Whilst the AM-APG algorithm represents a fully digital RIS scenario since it employs a digital precoder, thus has a better achievable rate than hybrid scenarios that use analog precoders, the various simulations that were completed aim to find the most suitable hybrid precoder so that its implementation is physically feasible, in regards to its complexity

level and material costs. In order to find the optimal hybrid architecture for this scenario, all the different configurations that were mentioned above will be tested in detail.

4.4.1. Phase Shifters - RIS Quantization Bits:

The following figures 4.20 and 4.21 depict the achievable rate using phase shifters with 3 bit quantization in the RF precoder for $N_{RIS} = 512$ whilst comparing different RIS quantization bits.

Figure 4.20 demonstrates the curves obtained using different quantization bits in the RIS. The curves for the quantized phase shifters in a fully connected architecture are being compared towards the unquantized phase shifters structure. Figure 4.21 also employs differing quantization bits in the RIS and 3 bit quantization in the RF precoder for quantized phase shifters in a partially connected structure.

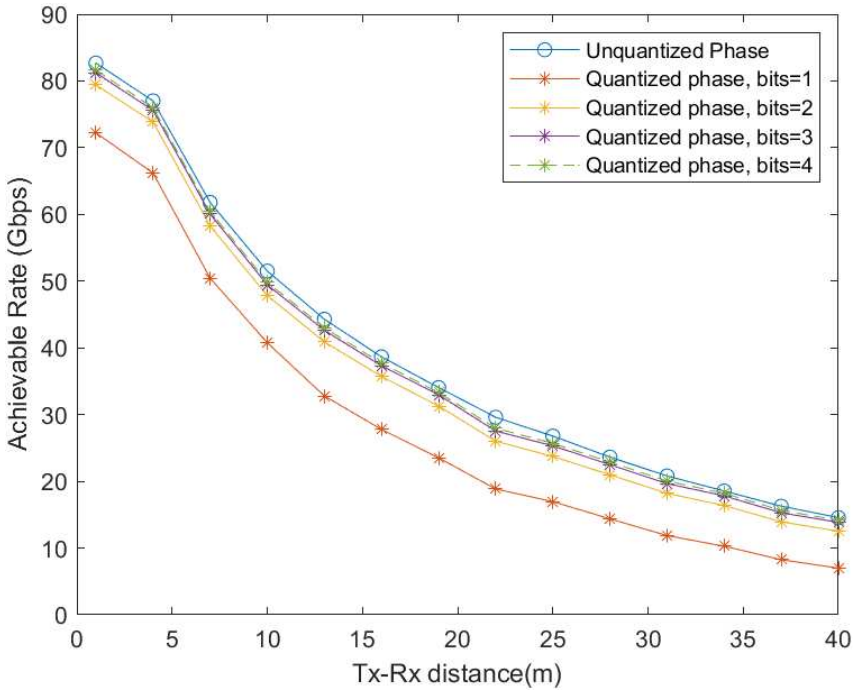

FIGURE 4.20. Achievable rate vs distance between Tx-Rx for fully connected precoders using quantized phase shifters, in comparison with UPS, using $N_{RIS} = 512$.

The use of 2 quantization bits on the reconfigurable intelligent surface emulates significantly close the achievable rate recorded using the unquantized phase shifter, seen in figure 4.20. The use of 3 bits is almost identical to the result obtained with higher quantization bits, thus 3 bits are suitable to achieve the ideal optimization on the phase shifter. The only case that worsens significantly the achievable rate is with 1 bit quantization.

Figure 4.21 demonstrates lower achievable rates in comparison with the values for the same RIS quantization bits used in figure 4.20 as a result of the current antennas not being connected to all existing subarrays. The 1 bit quantization at 1 meter of distance has an achievable rate of 67 Gbps. Upping the quantization bits to 3 or 4 at 1 meter of distance the achievable rate is 76 Gbps. This type of precoder benefits from using 3 bit

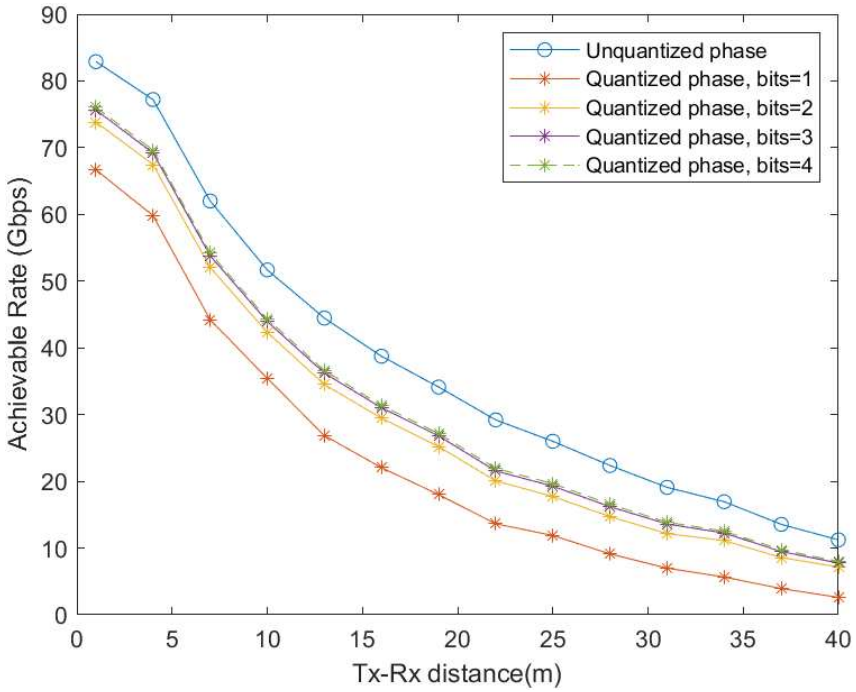

FIGURE 4.21. Achievable rate vs distance between Tx-Rx for partially connected precoders using quantized phase shifters, in comparison with UPS, considering $N_{RIS} = 512$.

quantization in order to achieve the best results without jeopardizing the quality of the communication between the transmitter and receiver.

4.4.2. Phase Shifter - Precoder Quantization Bits:

The RF precoder that implements phase shifters in its structure also quantizes its phases in the precoder, thus in the following figures 4.22 and 4.23 the RIS use a 3 bit quantization and the quantization in the RF precoder will vary.

Figures 4.22 and 4.23 represent different quantization bits in the RF precoder for fully and partially connected RF chains, respectively. In both figures, the use of 3 bit quantization presents the best result for implementation, since the curves for 3 and 4 bit quantization are virtually identical.

Therefore, in both cases the most beneficial quantization bits to be implemented in the RF precoder as well as in the RIS is 3 bits. It presents a near ideal solution without compromising the complexity of the hardware for not requiring the deployment of costly phase-shifters in RIS and in the precoder that uses phases shifters on its structure.

4.4.3. Switches

Figures D.3 and D.4 demonstrate the achievable rate using switches on the hybrid design. Whether it be fully connected, or partially connected, the achievable rate is very similar. As it is observed on figure 4.24 that conjoins the results seen in D.3 and D.4, for 512 RIS elements, the switches have the same achievable rate for fully and partially

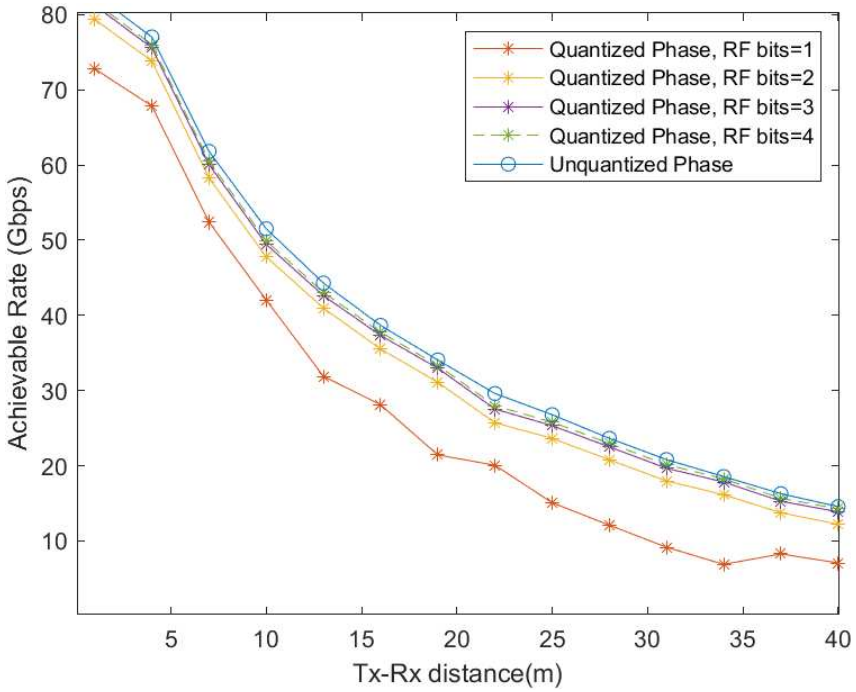

FIGURE 4.22. Achievable rate versus distance between Tx-Rx for fully connected quantized RF precoders, in comparison with unquantized phase shifter, considering $N_{RIS} = 512$.

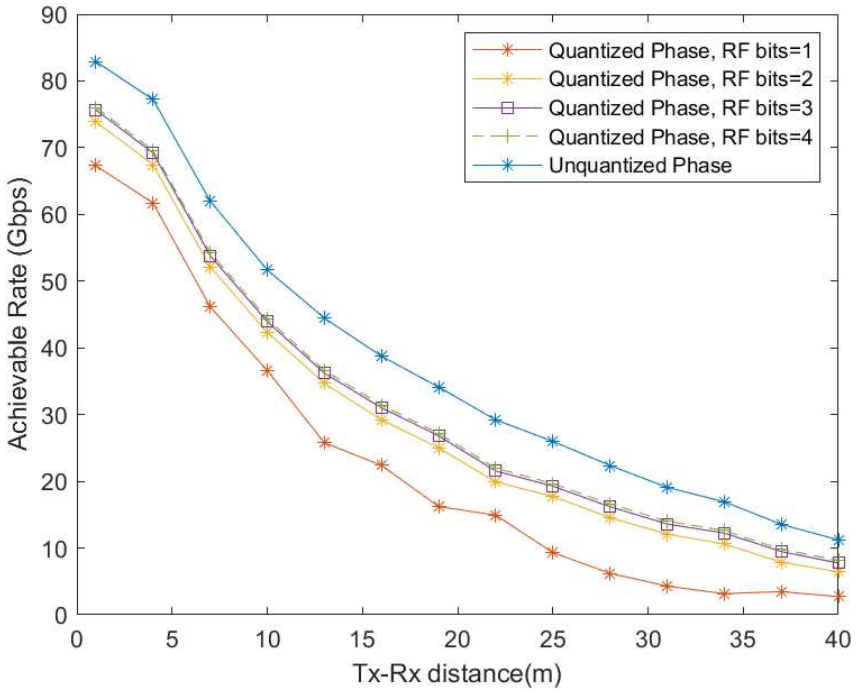

FIGURE 4.23. Achievable rate versus distance between Tx-Rx for partially connected quantized RF precoders, in comparison with unquantized phase shifter, considering $N_{RIS} = 512$.

connected, where at 10 meters of distance it reduces its rate to 3.8 Gbps, and at 15 meters of distance accomplishes a null achievable rate.

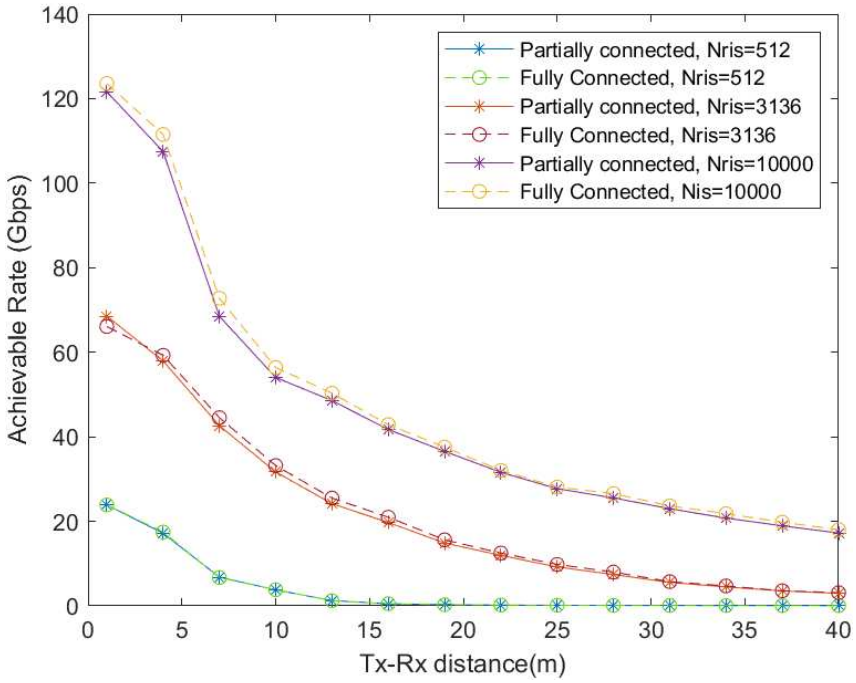

FIGURE 4.24. Study of Achievable rate (Gbps) comparing fully and partially connected switches, for different RIS elements whilst increasing the distance between Tx-Rx.

At the same distance, while employing 3136 RIS elements, the achievable rate increases to 33 Gbps within 10 meters of distance between the base station and the user. When this distance is increased to 40 meters of distance, the achievable rate for $N_{RIS} = 3136$ will reduce drastically towards 3.1 Gbps.

It may not be feasible to employ switches on the scenario implemented, since it demands an immense amount of RIS elements in order to make the communication between the transmitter and receiver viable. The use of 10000 RIS elements suffers a steep drop from 107.5 Gbps to 68.5 Gbps going from 4 to 7 meters of distance amidst the base station and the user.

4.4.4. Antenna Selection

The hybrid design that employs antenna selection is responsible for allotting each chain towards one single antenna. This method affects severely the achievable rate, as it is seen in figure 4.25 and D.5. According to figure 4.26, where both hybrid designs that use antenna selection are represented, the differences between fully or partially connected for the same RIS elements are minimal, thus it is more beneficial to utilize partially connected design for dividing the existing RF chains towards subarrays.

According to figure 4.25, when using 10000 RIS elements the user at 4 meters distance of the transmitter has a rate of 150 Gbps. If the distance is doubled to 10 meters, the rate decreases to 78.7 Gbps. In the same distance only using 3138 RIS elements, it is achieved 79.9 Gbps in the first 4 meters and 51.8 Gbps with a 10 meter distance between the BS and User.

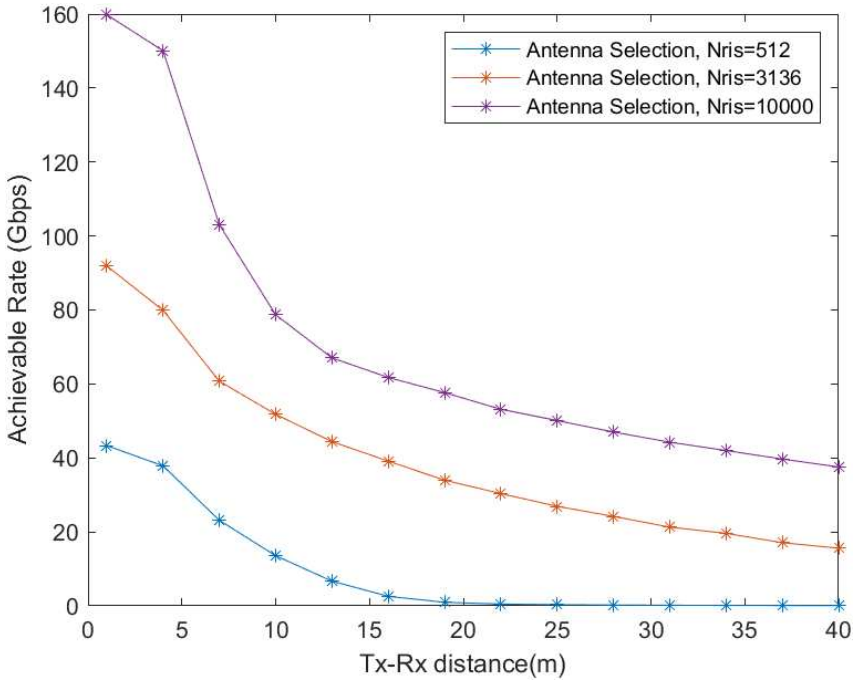

FIGURE 4.25. Study of Achievable rate (Gbps) using antenna selection fully connected for hybrid beamforming architecture, for different RIS elements whilst increasing the distance between Tx and Rx.

The smallest number of RIS elements tested, 512 RIS elements, recorded 37.9 Gbps in 4 meters amidst Tx and Rx and 13.56 Gbps for 10 meters. Increasing the distance between the transmitter and the receiver for $N_{RIS} = 512$, the achievable rate will reach null values. Thus, a higher number of RIS elements are needed if the hybrid design has antenna selection implemented.

4.4.5. Dynamic Array of Subarrays

In figure 4.27 it is simulated an hybrid design based on the AoSA architecture. In this case the hybrid precoding architecture in use is designated as dynamic array of subarrays. For $N_{RIS} = 512$ it is studied the impact of having more than one subarray connected to a RF chain, as well as selecting double or single phase shifters.

Accordingly, as observed in figure 4.27, the ideal case is represented with the curve of a fully digital RIS, AM-APG. Even though the implementation of DPS in the hybrid precoder design in theory should enhance the communication between Tx-RX, the achievable rate does not improve in comparison with the single phase shifter architecture.

When there is one subarray per RF chain, the rate obtained while the transceiver is within 5 meters of the user is 77 Gbps. This value drops when increasing the distance between Tx-Rx reaching 26 Gbps at 25 meters of distance.

Whilst theoretically having 2 subarrays in the same RF chain should present achievable rates higher than having only one subarray, according to the simulation, and as seen in figure 4.27, at 5 meters of distance the rate recorded is 73 Gbps, and at 25 meters this value decreases to 23 Gbps.

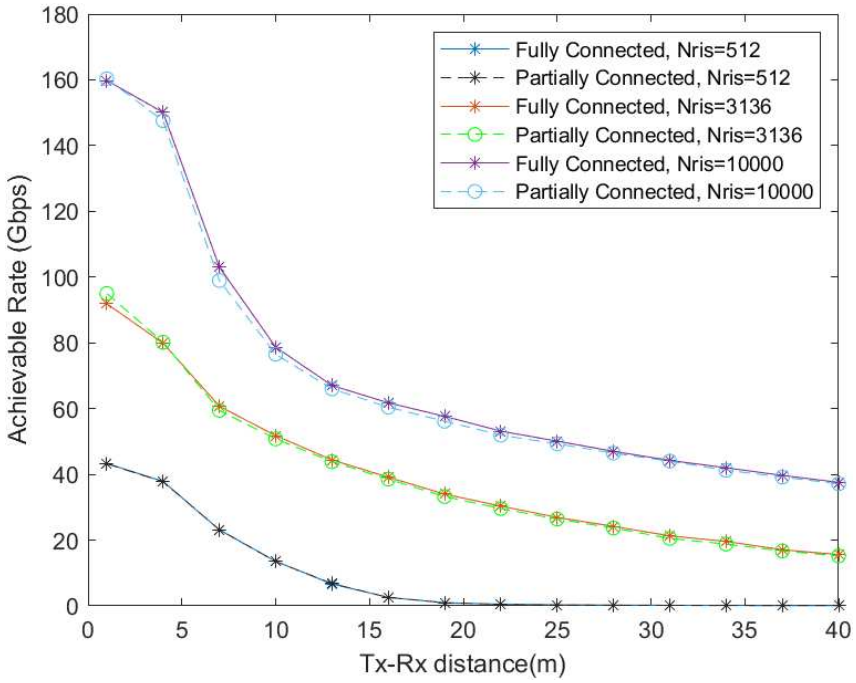

FIGURE 4.26. Study of Achievable rate (Gbps) comparing fully and partially connected antenna selection for hybrid beamforming architecture, for different RIS elements whilst increasing the distance between Tx and Rx.

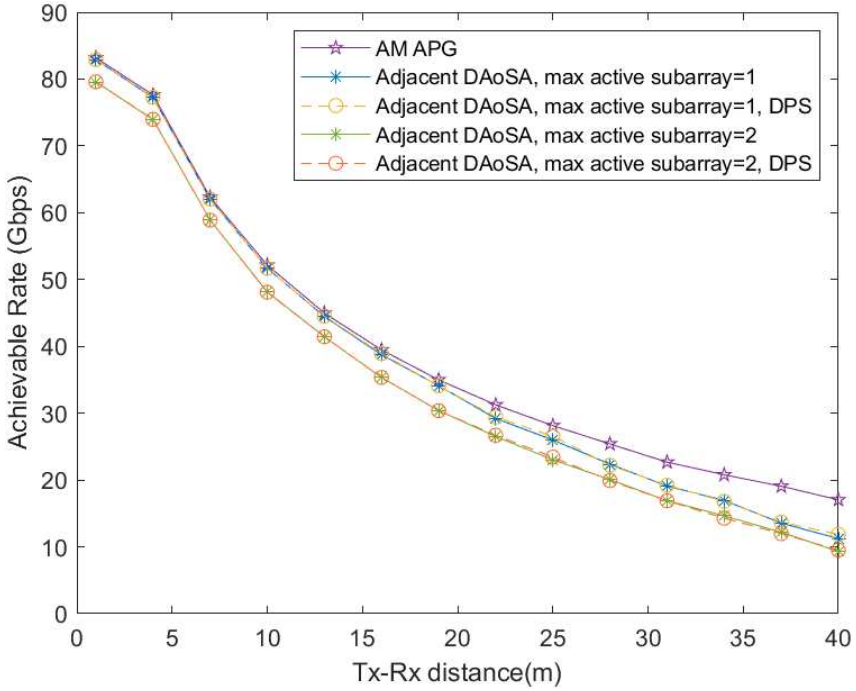

FIGURE 4.27. Study of Achievable rate (Gbps) using adjacent dynamic array of subarrays for hybrid beamforming architecture, with different number of subarrays per RF chain, as well as single or double phase shifter whilst increasing the distance between Tx and Rx.

Double phase shifter allows to change the phase and also the amplitude, however it does not affect the results seen in figure 4.27, having close to the same rate for the same distance whilst utilizing single phase shifters.

The hybrid precoder design using DAoSA architecture can also use free dynamic array of subarrays, as represented in figure 4.28. Using AM-APG curve as reference, all the curves have similar rates from 1 up to 16 meters of distance between Tx-Rx, going from 83 Gbps downwards to 39 Gbps.

After the distance surpasses 16 meters, the differences are viewable in figure 4.28. The greater the number of subarrays connected in each RF chain, the higher the achievable rate.

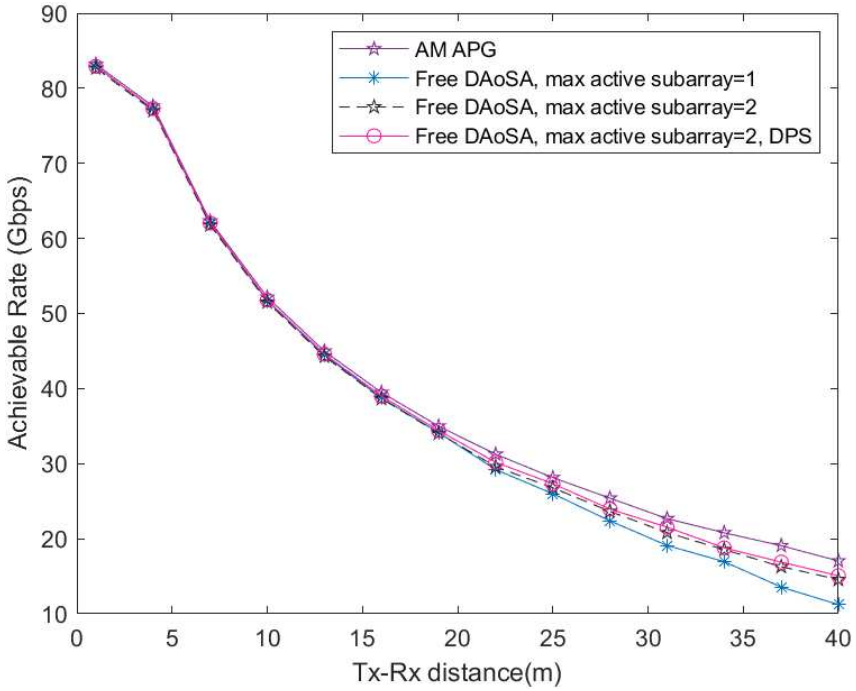

FIGURE 4.28. Study of Achievable rate (Gbps) using free dynamic array of subarrays with different number of subarrays per RF chain, as well as SPS or DPS, whilst increasing the distance between Tx and Rx.

Conjoining all DAoSA architectures tested in figure 4.29, whenever there is only one subarray per RF chain, the achievable rate will be equal regardless of it being adjacent DAoSA or free DAoSA.

Furthermore, when the number of subarrays per chain is 2, the rate achieved with the use of free dynamic array of subarray is closer to the values recorded with AM-APG, than with adjacent DAoSA. Thus, it is advantageous to use free dynamic AoSA rather than adjacent DAoSA.

4.4.6. All Hybrid architectures

Combining all hybrid architectures for $N_{RIS} = 512$, represented in figure 4.30, and considering fully connected stuctures, the designs that manage to obtain the rates closer to those obtained with AM-APG design are quantized and unquantized phase shifters.

The scenarios that do not use phase shifters present the worst rates whilst increasing the distance between the transmitter and the receiver. This is the case of the hybrid

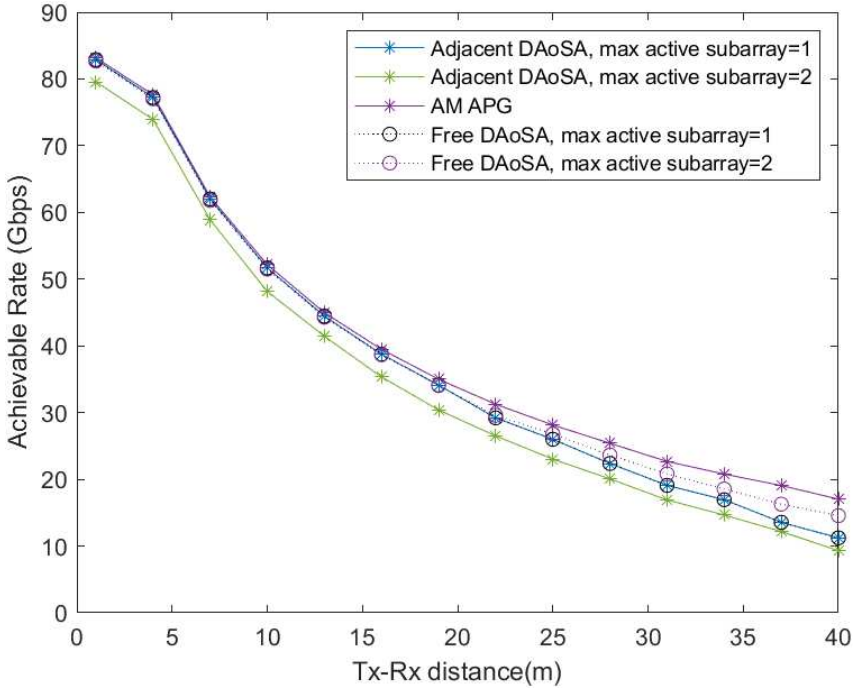

FIGURE 4.29. Study of Achievable rate (Gbps) using dynamic AoSA architecture with different number of subarrays per RF chain, whilst increasing the distance between Tx and Rx.

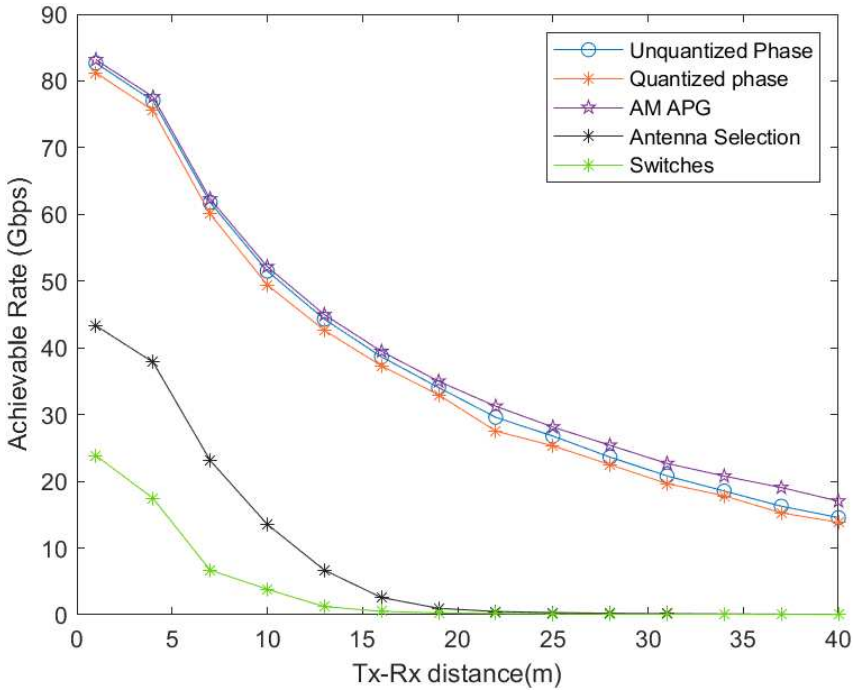

FIGURE 4.30. Study of Achievable rate (Gbps) on all fully connected hybrid designs with $N_{RIS} = 512$, whilst increasing the distance between Tx and Rx.

design that employs antenna selection or switches where the coverage range is severely limited.

In figure 4.31, it is demonstrated all the partially connected hybrid designs for $N_{RIS} = 512$ and using 3 quantization bits.

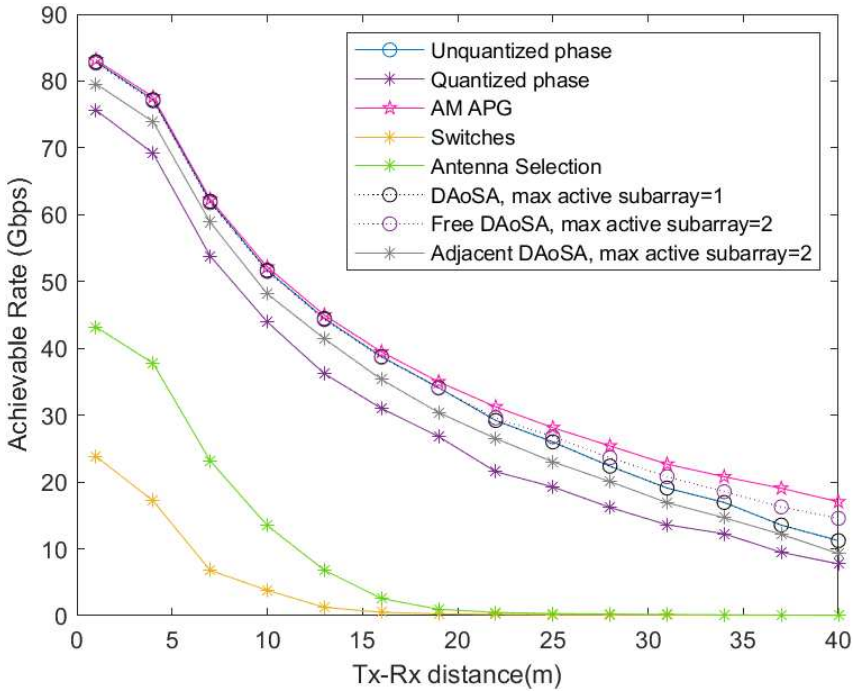

FIGURE 4.31. Study of Achievable rate (Gbps) for partially connected hybrid designs with $N_{RIS} = 512$, whilst increasing the distance between Tx-Rx.

It is concluded that the design that employs unquantized phase shifters achieves exactly the same rates as the architecture that uses dynamic array of subarrays, regardless of being adjacent or free DAoSA, as long as there is one subarray per RF chain. When there is more than one subarray per RF chain the rate will change accordingly: free dynamic AoSA offers higher rates when the distance increases and adjacent DAoSA presents inferior rates regardless of the distance between Tx-Rx.

Switches and antenna selection present the same behaviour in both figures 4.30 and 4.31. However, quantized phase shifters, for the same quantization bits in use, have lower achievable rates using partially connected hybrid precoders in comparison with their counterpart shown in figure 4.30 that employ fully connected hybrid precoders.

CHAPTER 5

Conclusion and Future Works

5.1. Conclusion

The dissertation examined and studied a RIS-supported UM-MIMO scheme aimed at improving the communication system for THz frequencies in order to support 6G communications. The system was designed to test several distinct hybrid precoders which were evaluated to determine the most adequate for implementation that would return an achievable rate similar to an all-digital precoder, while also reducing the overall implementation complexity and cost. In addition, the analysis of the quantization bits in each RIS element was also conducted in order to assess the impact on the received signal and the effect on the output signal generated towards the end user.

Chapter 2 clarifies the literature reviewed pertaining 6G communications in the THz and mmWave bands, as well as the implementation of RIS in UM-MIMO systems along with the respective hybrid beamforming implementations that can be performed. The following chapter outlines the system and channel model that were considered in the design of the RIS-assisted UM-MIMO THz communications system. An algorithm was developed for the deployment of hybrid precoders optimizing both the channel matrix and the RIS matrix.

Chapter 4 reports all the results collected through the developed simulator for the different hybrid beamforming techniques. Since the THz band is not widely accessible for testing, a benchmark in the mmWave spectrum, already in use for 5G, is necessary to further evaluate the achievable rates in order to assess the performances of the hybrid precoders while also assessing how the number of RIS elements and the antennas used may impact the achievable rate .

The first studies conducted with mmWave set to 28 GHz show that the propagation is not so prone to high absorption losses, so the direct channel between Tx-Rx is not obstructed and can be used. As the smaller frequencies gain advantage by having the possibility of both the direct channel and the RIS channel being used simultaneously, the results show an increase in the achievable rate registered versus when only one path is activated. The smaller the operating frequency, the fewer the number of RIS and Tx and Rx antennas needed, reducing the complexity of the system.

The achievable rate when only the RIS link is active regarding the mmWave band displays that the hybrid precoders performing the closest to a fully digital RIS or to a hybrid precoder that uses the unquantized phase shifter are the quantized phase shifter partially connected using 3 bits and the free dynamic array of subarrays. The partially

connected structure delivers acceptable achievable rates and its structure provides lower complexity in assembling in comparison to a fully connected architecture.

Furthermore, for the mmWave frequency as well, the optimal RIS location was deducted to maximize the achievable rate. The nearer the RIS is located to either the transmitter or receiver antenna, the higher the achievable rate for the transmitted power will be.

In the final part of chapter 4, the THz frequency for RIS-assisted UM-MIMO communication systems is examined. The simulations for the THz frequency using 300 GHz illustrate the impact of the high absorption losses along the wave path, thereby making it required to deploy a greater number of RIS elements, transmitter and receiver antennas, to overcome and allow the forwarding of the inbound signal. The performance of the hybrid precoder is the same, and in addition, the phase shift that is quantized using 3 bits in the RF precoder and in the RIS delivers the most achievable rate. Nevertheless, the RIS with lower resolution using only 2 bits of quantization may suffice to achieve comparable unquantized phase shift rates, therefore decreasing its implementation cost.

The optimal hybrid precoder designs referred in the mmWave study, namely the quantized phase shifter and the free dynamic array of subarray, present the best achievable rates as well for the THz band. Both frameworks are similar to each other since the RF precoder employs phase shifts, however the capability of the free DAoSA to modify its structure by allowing differing RF subarrays to be connected per antenna will drastically improve the performance of the Tx-Rx link.

Dynamic AoSA presents the best achievable rates for the scenarios being tested. It is advantageous to utilize Free DAoSA with more than 1 subarray connected per RF chain in the system in order to obtain the best result for the communication between BS and the user.

In conclusion, the results obtained provide information about the importance of implementing RIS in order to improve the quality of communication systems in future wireless networks when the LoS is obstructed, as was documented in the literature that implemented RIS-empowered UM-MIMO systems. However, the existing limitations in the phase resolution of RIS elements and its implementation cost in a realistic environment still pose a number of concerns. While theoretically the analysis conducted demonstrates a potential for success, the elevated expense of installing RIS and the overall energy consumption still require further studies.

5.2. Future Work

The work presented in this thesis can be further extended by focusing on and broadening the RIS-assisted UM-MIMO communication system for THz frequencies while using a hybrid precoder that has been devised over the course of this dissertation through

- The design of a framework to handle multiple end users. In the present study only a single user equipment was devised to be in use towards the scheme planned.

The RIS-supported UM-MIMO structure could be developed in order to have multiple UEs on the same network.

- An additional framework to be implemented would allow multiple RIS panels, thus creating a larger and larger network interconnected via a BS to multiple RIS, and in return route the signal to the multiusers available on the same network.

Bibliography

[1] I. F. Akyildiz, C. Han, and S. Nie, "Combating the Distance Problem in the Millimeter Wave and Terahertz Frequency Bands," *IEEE Communications Magazine*, vol. 56, pp. 102–108, 6 2018.

[2] E. Björnson, Ö. Özdogan, and E. G. Larsson, "Reconfigurable Intelligent Surfaces: Three Myths and Two Critical Questions," *CoRR*, vol. abs/2006.03377, 2020.

[3] S. Gong, X. Lu, D. T. Hoang, D. Niyato, L. Shu, D. I. Kim, and Y. Liang, "Towards Smart Radio Environment for Wireless Communications via Intelligent Reflecting Surfaces: A Comprehensive Survey," *CoRR*, vol. abs/1912.07794, 2019.

[4] BR, "Recommendation ITU-R M.2083-0 IMT Vision-Framework and overall objectives of the future development of IMT for 2020 and beyond M Series Mobile, radiodetermination, amateur and related satellite services," tech. rep., Internation Telecommunication Union, 2015.

[5] "The Next hyper Connected Experience for All," tech. rep., Samsung, 12 2020.

[6] "Sixth generation (6G) wireless networks: Vision, research activities, challenges and potential solutions," *Symmetry*, vol. 12, 4 2020.

[7] "Spectrum Expanding the Frontier 6G," tech. rep., Samsung, 5 2022.

[8] N. Lawrence, B. Ng, H. Hansen, and D. Abbott, "5g Terrestrial Networks: Mobility and Coverage-Solution in Three Dimensions," *IEEE Access*, vol. 5, pp. 8064–8093, 04 2017.

[9] S. Dash, C. Psomas, I. Krikidis, I. F. Akyildiz, and A. Pitsillides, "Active Control of THz Waves in Wireless Environments using Graphene-based RIS," *IEEE Transactions on Antennas and Propagation*, pp. 1–3, 2022.

[10] J. M. Jornet and I. F. Akyildiz, "Channel Modeling and Capacity Analysis for Electromagnetic Wireless Nanonetworks in the Terahertz Band," *IEEE Transactions on Wireless Communications*, vol. 10, no. 10, pp. 3211–3221, 2011.

[11] C. Han, Y. Wu, Z. Chen, and X. Wang, "Terahertz Communications (TeraCom): Challenges and Impact on 6G Wireless Systems," 2019.

[12] T. S. Rappaport, Y. Xing, O. Kanhere, S. Ju, A. Madanayake, S. Mandal, A. Alkhateeb, and G. C. Trichopoulos, "Wireless Communications and Applications Above 100 GHz: Opportunities and Challenges for 6G and Beyond," *IEEE Access*, vol. 7, pp. 78729–78757, 2019.

[13] M. D. Renzo, A. Zappone, M. Debbah, M. S. Alouini, C. Yuen, J. D. Rosny, and S. Tretyakov, "Smart Radio Environments Empowered by Reconfigurable Intelligent Surfaces: How It Works, State of Research, and the Road Ahead," *IEEE Journal on Selected Areas in Communications*, vol. 38, pp. 2450–2525, 11 2020.

[14] E. Basar, I. Yildirim, and F. Kilinc, "Indoor and Outdoor Physical Channel Modeling and Efficient Positioning for Reconfigurable Intelligent Surfaces in mmwave Bands," *IEEE Transactions on Communications*, vol. 69, no. 12, pp. 8600–8611, 2021.

[15] E. Basar and I. Yildirim, "Reconfigurable Intelligent Surfaces for Future Wireless Networks: A Channel Modeling Perspective," *IEEE Wireless Communications*, vol. 28, no. 3, pp. 108–114, 2021.

[16] S. Dash, C. Psomas, I. Krikidis, I. F. Akyildiz, and A. Pitsillides, "Active Control of THz Waves in Wireless Environments using Graphene-based RIS," *IEEE Transactions on Antennas and Propagation*, pp. 1–1, 1 2022.

[17] H. Wymeersch, A. Clemente, J. He, B. Denis, and M. Juntti, "Radio Localization and Mapping with Reconfigurable Intelligent Surfaces," arXiv, 2019.

[18] C. Huang, Z. Yang, G. C. Alexandropoulos, K. Xiong, L. Wei, C. Yuen, Z. Zhang, and M. Debbah, "Multi-Hop RIS-Empowered Terahertz Communications: A DRL-Based Hybrid Beamforming Design," *IEEE Journal on Selected Areas in Communications*, vol. 39, pp. 1663–1677, jun 2021.

[19] E. G. Larsson, O. Edfors, F. Tufvesson, and T. L. Marzetta, "Massive MIMO for next generation wireless systems," *IEEE Communications Magazine*, vol. 52, pp. 186–195, 2014.

[20] R. Chataut and R. Akl, "Massive MIMO Systems for 5G and Beyond Networks—Overview, Recent Trends, Challenges, and Future Research Direction," *Sensors*, vol. 20, p. 2753, 05 2020.

[21] Z. Wani, M. P. Abegaonkar, and S. K. Koul, "A 28-GHz Antenna for 5G MIMO Applications," *Progress In Electromagnetics Research Letters*, vol. 78, pp. 73–79, 2018.

[22] B. Ning, Z. Tian, Z. Chen, C. Han, J. Yuan, and S. Li, "Prospective Beamforming Technologies for Ultra-Massive MIMO in Terahertz Communications: A Tutorial," *CoRR*, vol. abs/2107.03032, 2021.

[23] A. F. Molisch, *Wireless communications*. Wiley, 2011.

[24] B. Di, H. Zhang, L. Song, Y. Li, Z. Han, and H. V. Poor, "Hybrid Beamforming for Reconfigurable Intelligent Surface based Multi-User Communications: Achievable Rates with Limited Discrete Phase Shifts," *IEEE Journal on Selected Areas in Communications*, vol. 38, pp. 1809–1822, 8 2020.

[25] J. Praia, J. P. Pavia, N. Souto, and M. Ribeiro, "Phase Shift Optimization Algorithm for Achievable Rate Maximization in Reconfigurable Intelligent Surface-Assisted THz Communications," *Electronics*, vol. 11, p. 18, 12 2021.

[26] S. Jayaweera and H. Poor, "Capacity of multiple-antenna systems with both receiver and transmitter channel state information," *IEEE Transactions on Information Theory*, vol. 49, no. 10, pp. 2697–2709, 2003.

[27] A. Saleh and R. Valenzuela, "A Statistical Model for Indoor Multipath Propagation," *IEEE Journal on Selected Areas in Communications*, vol. 5, no. 2, pp. 128–137, 1987.

[28] O. E. Ayach, S. Rajagopal, S. Abu-Surra, Z. Pi, and R. W. Heath, "Spatially Sparse Precoding in Millimeter Wave MIMO Systems," *IEEE Transactions on Wireless Communications*, vol. 13, no. 3, pp. 1499–1513, 2014.

[29] K. Dovelos, S. D. Assimonis, H. Q. Ngo, B. Bellalta, and M. Matthaiou, "Intelligent Reflecting Surfaces at Terahertz Bands: Channel Modeling and Analysis," *2021 IEEE International Conference on Communications Workshops, ICC Workshops 2021 - Proceedings*, 6 2021.

[30] J. Ren and R. G. Vaughan, "Rice Factor Estimation from the Channel Phase," *IEEE Transactions on Wireless Communications*, vol. 11, no. 6, pp. 1976–1980, 2012.

[31] Y.-P. Lin, "On the Quantization of Phase Shifters for Hybrid Precoding Systems," *IEEE Transactions on Signal Processing*, vol. 65, no. 9, pp. 2237–2246, 2017.

[32] R. Méndez-Rial, C. Rusu, N. González-Prelcic, A. Alkhateeb, and R. W. Heath, "Hybrid MIMO Architectures for Millimeter Wave Communications: Phase Shifters or Switches?," *IEEE Access*, vol. 4, pp. 247–267, 2016.

[33] J. Miguel and R. Praia, "Um projeto de sistema de comunicações com reconhecimento de contexto para a banda Thz," Master's thesis, Iscte - Instituto Universitário de Lisboa, 2021.

[34] J. P. Pavia, V. Velez, R. Ferreira, N. Souto, M. Ribeiro, J. Silva, and R. Dinis, "Low Complexity Hybrid Precoding Designs for Multiuser mmWave/THz Ultra Massive MIMO Systems," arXiv, 2021.

[35] Y.-P. Lin, "On the quantization of phase shifters for hybrid precoding systems," *IEEE Transactions on Signal Processing*, vol. 65, no. 9, pp. 2237–2246, 2017.

[36] X. Yu, J. Zhang, and K. B. Letaief, "Doubling Phase Shifters for Efficient Hybrid Precoder Design in Millimeter-Wave Communication Systems," *Journal of Communications and Information Networks*, vol. 4, no. 2, pp. 51–67, 2019.

[37] L. Yan, C. Han, and J. Yuan, "A Dynamic Array-of-Subarrays Architecture and Hybrid Precoding Algorithms for Terahertz Wireless Communications," *IEEE Journal on Selected Areas in Communications*, vol. 38, pp. 2041–2056, 9 2020.

[38] Y. Xing, T. S. Rappaport, and A. Ghosh, "Millimeter Wave and sub-THz Indoor Radio Propagation Channel Measurements, Models, and Comparisons in an Office Environment," *CoRR*, vol. abs/2103.00385, 2021.

APPENDIX A

Article: Hybrid Precoder Algorithm Optimization in Reconfigurable Intelligent Surface-Assisted THz Ultra Massive MIMO Systems

MDPI

Article

Hybrid Precoder Algorithm Optimization in Reconfigurable Intelligent Surface-Assisted THz Ultra Massive MIMO Systems

Ana Rita Santos [1,2,*], Nuno Souto [1,2] and Marco Ribeiro [1,2]

[1] Department of Information Science and Technology, ISCTE - Instituto Universitário de Lisboa, 1649-026 Lisboa, Portugal; nuno.souto@iscte-iul.pt (N.S.); marco.ribeiro@iscte-iul.pt (M.R.)
[2] Instituto de telecomunicações, 1049-001 Lisboa, Portugal
* Correspondence: arbcr@iscte-iul.pt

Abstract: Future sixth generation (6G) wireless networks perceive the THz band as essential to support the high volume of wireless traffic data being generated in the network, enabling ultra high transmission rates. However, the behaviour of the THz frequency spectrum affects the propagation occurring in the wireless communication system due to high attenuation, leading to severe propagation losses. In this work we consider reconfigurable intelligent surfaces (RIS) to overcome the limitations present in the THz band by optimizing the communication network performance when combined with ultra-massive multiple-input multiple-output antennas (UM-MIMO) as the large number of antennas provides high directivity pencil like beams, thereby enabling easy data spread from the transmitter towards the receiver for THz frequencies. It will be devoloped a hybrid precoder algorithm to maximize the achievable rate of THz UM-MIMO communications by separating the computation of the digital and the analog precoder and the adoption of hybrid designs, namely fully connected, array of subarray (AoSA) and dynamic array of subarray (DAoSA). The numerical results obtained reveal the success of the algorithm adopted for severely impacted THz systems.

Keywords: 6G; achievable rate; Terahertz (THz) communications; channel modeling; reconfigurable intelligent surfaces (RIS); ultra massive multiple-input multiple-output (UM-MIMO).

Citation: Santos, A. R.; Souto, N.; Ribeiro, M. Hybrid Precoder Algorithm Optimization in Reconfigurable Intelligent Surface-Assisted THz Ultra Massive MIMO Systems. *Journal Not Specified* **2022**, *1*, 0. https://doi.org/

Received:
Accepted:
Published:

1. Introduction

The evolution of wireless communications in the past years led to an enormous increase in the number of data rates consumed globally to be able to support the ever-growing number of interconnected devices as well as create solutions to support future wireless communications [1].

The development for 6G communication systems comes as a response to culminate the missing elements present on existing LTE and 5G systems. According to the recommendations outlined on ITU-R M.2083, 5G is designed to reach as far as 20 Gbps [2]. As a result, 5G communications are no longer sufficient as the ever growing pace of wireless communications globally and its large volume of data created and required have surpassed the current experience data rate supported.

The main prerequisites for the migration from 5G to a 6G framework are associated with improving the energy and spectrum efficiency, increasing the peak data rate experience from previously achieving only 20 Gbps to reaching 1 Tbps [3].

Millimeter wave bands (30-300 GHz) already provide support to 5G and have a very substantial contribution towards the roll out of 6G technologies by enabling gigabit-per-second data rates in indoor systems for wireless networks. The mmWave spectrum is divided in multiple frequency smaller blocks where Each block can have differing bandwidths, depending on the requirements proposed by the user on the 5G service to be executed. Notably, 28 GHz has been successfully commercially developed and deployed in several countries, such as Japan and US [4].

Terahertz Band (0.1-10 THz) is envisioned as a key wireless technology to satisfy the future demands within sixth generation (6G) systems by solving the spectrum scarcity problem observed on millimeter wave systems due to the narrowed bandwidths available [1]. The THz band offers higher spectrum efficiency, experienced data rate and peak data rate, as well as lower latency in comparison to existing 5G systems. The large bandwidth available in the THz band allows the transmission of high data rates in the order of terabits per second (Tbps) [5].

THz waves have radio frequency (RF) higher than millimeter waves resulting in forwarding data faster through the wireless network, however it presents lower wavelengths, ensuing in a shorter propagation distance possible.

The channel characteristics operating at the THz band are susceptible to atmospheric loss, meaning molecular absorption loss due to water vapor and oxygen molecules at THz frequencies. This results in high path loss for line-of-sight (LoS) links by creating spectral windows with different bandwidths and distance variations [1]. 6G THz systems suffer from high sparsity when electromagnetic (EM) waves are reflected, refracted, or absorbed on rough surfaces, resulting in attenuation as well as scattered waves amongst all directions. The higher the frequency in use, the higher the scattering will be [6].

Reconfigurable Intelligent Surfaces (RIS) are seen as a promising technology for THz systems for their ability to be programmable, being able to change an impinging electromagnetic (EM) wave and redirect it towards the desired user, without requiring a power amplifier, Radio Frequency (RF) chain, or sophisticated signal processing [7,8].

To combat the severe limitation of signal transmission distance and coverage provided for the Terahertz frequency band, Reconfigurable Intelligent Surfaces are seen as a solution towards creating a smart wireless communication environment based on software-controlled metasurfaces that are deployed in the wireless communications to shape the incoming radio waves and forward the incoming signal toward the end users [9].

Propagation at high carrier frequencies suffer from blockage between the transmitter and receiver, limiting the reliability of the Line-of-Sight path. To avoid obstructions, it is necessary to create multiple possible paths (multi-paths) to guarantee full coverage when LoS is obstructed. Thus, MIMO systems relying on arrays implemented on metamaterials or metasurfaces, previously present on 5G systems, are seen as a good solution in order to improve the propagation paths that were severely affected in the THz band. The implementation of RIS facilitates the creation of a smart radio environment (SRE) by controlling the signal propagation properties as a means to improve its performance by guaranteeing signal reception [8].

Reconfigurable Intelligent Surfaces are ultra-thin surfaces composed of materials capable of shaping the propagation environment by modifying the radio waves impinging upon the RIS surface and controlling their direction by altering the wireless signals that are being propagated between the transmitter and receiver, thus enabling optimization of the transmitter as well as the receiver in use.[8]. The main function of RIS is distributing the electromagnetic (EM) currents coming from the transmitter antennas towards the numerous elements that compose a RIS. The current signal will be controlled and modified by the RIS elements in order to modify its path and allow to impinge the signal towards its final destination, the receiver antennas [10]. LoS blockages can be routed with the use of multi paths available on the environment.

The implementation of RIS in communication systems has been demonstrated through the modeling of channel matrices for lower frequencies within the mmWave Band in [11] and [10]. The introduction of RIS structures for THz band are based on a RIS graphene model where this framework is viewed as one of the most efficient structures towards the THz frequency spectrum for reflecting almost in its entirety the THz wave in an operational frequency between 0.1 to 4 THz [12].

RIS consists of a large number of RIS elements, or antenna elements far away from the Base Station (BS), configured to do analog beamforming, though the existent phase shifters in each RIS element. These RIS elements do not have any digital processing capacity,

requiring signal processing to be carried out at the BS. Digital beamforming is realized at the Base Station where each antenna is responsible for encoding the data stream and transmitting it. Analog beamforming is executed by the RIS through discrete phase shifts responsible for the reflection of the incident wave. All signals obtained in each RIS element will be grouped together and form the signal the user will receive [13].

The THz band limits severely the feasible distance between transmitter and receivers, requiring the implementation of high-gain antennas capable of directing the incoming signal in order to transmit it successfully. Multiple-Input Multiple-Output (MIMO) systems employ several antennas at both ends of the link to increase the spectral efficiency as well as the number of users served simultaneously by being able to transmit multiple streams of data, a fundamental key for wireless communication systems [14,15]. High gain antennas are adapted with MIMO systems in order to overcome the high path loss observed in either the mmWave band or the interference seen in THz band.

Ultra-massive MIMO structures enables the high number of antenna arrays existing at each end to be grouped together, thus increasing the transmission throughput, as well as steering the narrow beam on the strongest path possible between the transmitter and receiver [14]. The implementation of beamforming in massive MIMO systems increases spectrum efficiency and the capability of multi-pathby overcoming the attenuation present on mmWave and THz frequencies bands, thus improving the communication distance.

The high attenuation present in the THz band is solvable with the implementation of the UM-MIMO framework and its hybrid precoder framework.The use of RIS within UM-MIMO communication systems can surpass the high energy intake that is generated while communicating from the transmitter antennas to the receiver using THz frequency band.

This article will focus on the design of an efficient and effective smart wireless communication environment using reconfigurable intelligent surfaces (RIS) through the optimization of the individual RIS elements and transceivers in order to combat the severe distance limitation in the Terahertz band. The main objectives to be studied are the usage of large antennas at the transmitter and receiver in combination with RIS, implementation of hybrid schemes at the transmitter in order to reduce its complexity, and the implementation of an algorithm for optimal design of the precoder and the RIS simultaneously. To execute the evaluation of the proposed THz UM-MIMO system, the results achieved demonstrate the effectiveness of the proposed algorithm, where higher the number of RIS elements allocated, higher the achievable rate. It is also studied the impact of quantization in RIS elements and in the hybrid precoders.

This paper is organized as follows: section 2 displays the system model for RIS-assisted THz UM-MIMO system, section 3 presents the proposed hybrid precoder algorithm followed by the respective numerical results in section 4. Section 5 presents the conclusions.

Notation: Matrices and vectors are represented in boldface letters in uppercase and lowercase, respectively. The supperscript $[.]^T$ and $[.]^H$ denote a transpose and conjugate transpose matrix/vector, accordingly. $\mathbf{I}_{n\times n}$ identity matrix of the dimension $n \times n$, $|.|$ is a modulus operator, $\|.\|_F$ is the Frobenius norm and $det(.)$ represents the determinant.

2. System Model

It is assumed an UM-MIMO system for a THz band with an end-to-end channel matrix composed with N_{Tx} large transmit antenna arrays and N_{Rx} large receive antenna arrays in operation. The communication link in a indoor environment is established with the aid of RIS with N_{RIS} reflecting elements, represented in figure 1.

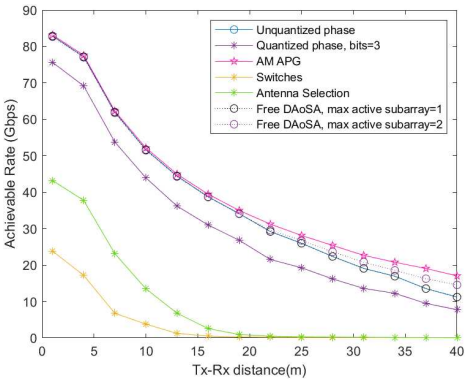

Figure 10. Study of Achievable rate (Gbps) for partially connected hybrid designs with $N_{RIS} = 512$, whilst increasing the distance between Tx-Rx.

The design that employs unquantized phase shifters achieves exactly the same rates as the architecture that uses dynamic array of subarrays with one subarray per RF chain. When there is more than one subarray per RF chain free dynamic AoSA offers higher rates when the distance increases .

Switches and antenna selection present the same behaviour in both figures 9 and 10. However, quantized phase shifters, for the same quantization bits in use, have lower achievable rates using partially connected hybrid precoders in comparison with their counterpart shown in figure 9 that employ fully connected hybrid precoders.

5. Conclusion

In this article it was examined and studied a RIS-supported UM-MIMO scheme aimed at improving the communication system for THz frequencies in order to support 6G communications. The system was designed to test several distinct hybrid precoders which were evaluated to determine the most adequate for implementation that would return an achievable rate similar to an all-digital precoder, while also reducing the overall implementation complexity and cost. In addition, the analysis of the quantization bits in each RIS element was also conducted in order to assess the impact on the received signal and the effect on the output signal generated towards the end user.

The simulations for the THz frequency using 300 GHz illustrate the impact of the high absorption losses along the wave path, thereby making it required to deploy a greater number of RIS elements, transmitter and receiver antennas, to overcome and allow the forwarding of the inbound signal. The performance of the hybrid precoder is the same, and in addition, the phase shift that is quantized using 3 bits in the RF precoder and in the RIS delivers the most achievable rate. Nevertheless, the RIS with lower resolution using only 2 bits of quantization may suffice to achieve comparable unquantized phase shift rates, therefore decreasing its implementation cost.

The optimal hybrid precoder designs quantized phase shifter and free dynamic array of subarray present the best achievable rates for the THz band. Both frameworks are similar to each other since the RF precoder employs phase shifts, however the capability of the free DAoSA to modify its structure by allowing differing RF subarrays to be connected per antenna will drastically improve the performance of the Tx-Rx link.

In conclusion, the results obtained provide information about the importance of implementing RIS in order to improve the quality of communication systems in future wireless networks when the LoS is obstructed, as was documented in the literature that implemented RIS-empowered UM-MIMO systems. However, the existing limitations in the phase resolution of RIS elements and its implementation cost in a realistic environment still pose a number of concerns. While theoretically the analysis conducted demonstrates

The clusters and the arrays present within each cluster have particular angles of arrival and departure, thus the vectors $\mathbf{a}_S(\phi^S_{c,s}, \theta^S_{c,s})$ and $\mathbf{a}_{RIS}(\phi^{RIS,S}_{c,s}, \theta^{RIS,S}_{c,s})$ represent the array response vector, for the considered azimuth $\phi_{c,s}$ and elevation $\theta_{c,s}$ for the angles of arrival (AoA) or the angles of departure (AoD).

In equation 3 AoD is represented as $\mathbf{a}_S$ for the large transmitter antenna array and AoA is outlined as $\mathbf{a}_{RIS}$ for the RIS, respectively. Assuming an uniform planar array (UPA) implementation, the array response vector for the transmitter, $\mathbf{a}_S(\phi^S_{c,s}, \theta^S_{c,s})$ is calculated [11,19] as

$$\mathbf{a}_S(\phi^S_{c,s}, \theta^S_{c,s}) = \Big[1, ..., e^{j\frac{2\Pi}{\lambda} d_s (a \sin(\phi^S_{c,s}) \sin(\theta^S_{c,s}) + b \cos(\theta^S_{c,s}))}, \ldots, e^{j\frac{2\Pi}{\lambda} d_s ((\sqrt{N_{Tx}}-1) \sin(\phi^S_{c,s}) \cos(\theta^S_{c,s}) + (\sqrt{N_{Tx}}-1) \cos(\theta^S_{c,s}))}\Big]^T \tag{4}$$

where $0 \leqslant a \leqslant (\sqrt{N_{Tx}} - 1)$ and $0 \leqslant b \leqslant (\sqrt{N_{Tx}} - 1)$, a and b represent the width and height of the square array for the antennas, respectively. λ is the signal wavelength and d_s is the spacing between elements in the transmission matrix.

The expression of the channel vector, $\mathbf{H}^{RIS,S}_{LOS}$ is written as

$$\mathbf{H}^{RIS,S}_{LOS}(n, m) = \sqrt{\frac{G_{Tx}\ A_{RIS}}{(4\pi d_{n,m})^2} e^{-k_{abs}(f) d_{n,m}}} e^{-j2\pi \frac{d_{n,m}}{\lambda}} \tag{5}$$

The line-of-sight expression in 5 for the link between the transmitter and RIS, represents the transmit antenna gain as G_{Tx} and A_{RIS} signifies the area of RIS element, obtained through $A_{RIS} = \lambda^2$. The variable n describes the n^{th} RIS element and the m^{th} transmitter antenna element, thus $d_{n,m}$ denotes the distance for each existent transmitter antenna and RIS element. The coefficient of the molecular absorbing loss is represented as $k_{abs}(f) = 0.0033$ [20].

The path loss of the NLoS channel between Tx-RIS for the $(c, s)th$ element is obtained through

$$PL^{RIS,S}_{NLOS} = \frac{G_{Tx} A_{RIS}}{(4\pi d_{s,RIS})^2} e^{-k_{abs}(f) d_{s,RIS}} \tag{6}$$

whereas $d_{s,RIS}$ is the distance between the transmitter and the RIS element in use.

As the path loss is applied, the rice factor is implemented in order to normalize the channel. The Rice factor, K_{rice}, denotes the relative level of the LOS component, thus it indicates the quality of the channel and the fading the path is subjected to. As a result, the Rician factor represents the ratio between the LOS and NLOS components [21].

The sub-channel matrix from the RIS towards the Receiver, RIS-Rx, denominated as $\mathbf{H}^{D,RIS}$ will be written similarly as the equation 3

$$\mathbf{H}^{RIS,S} = \sum_{c=1}^{C} \sum_{s=1}^{S_c} \beta_{c,s} \sqrt{PL^{D,RIS}_{NLOS}} \mathbf{a}_{RIS}(\phi^{D,RIS}_{c,s}, \theta^{D,RIS}_{c,s}) \mathbf{a}_D(\phi^D_{c,s}, \theta^D_{c,s}) + \mathbf{H}^{D,RIS}_{LOS} \tag{7}$$

3. Proposed Hybrid Precoder Algorithm

In this section, it is introduced the algorithm for the hybrid precoder and its implementation using distinct architectures.

3.1. Main Algorithm

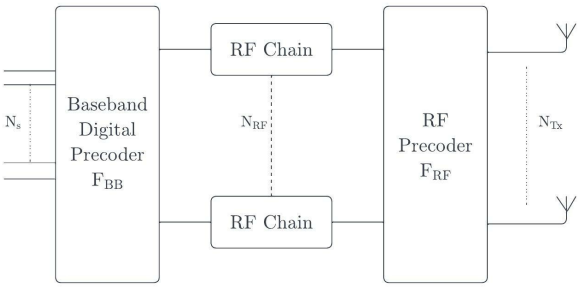

Figure 2. Hybrid Precoder.

The usage of a hybrid precoder enables the conjoined use of an analog as well as a digital precoder, represented in figure 2. As follows, the propagation channel that reaches the end user on equation 1 is modified by separating the fully digital precoder **F** into two distinct matrices representing the digital and the analog precoder. The processed received signal when implementing a hybrid precoder is obtained as

$$\mathbf{r} = \sqrt{\rho}\mathbf{W}\mathbf{H}^{total}\mathbf{F}_{RF}\mathbf{F}_{BB}\mathbf{s} + \mathbf{W}\mathbf{n} \tag{8}$$

where s is the symbol vector, $\mathbf{F}_{BB} \in C^{N_{RF} \times Ns}$ represents the baseband matrix obtained through $F_{BB} = N_{RF}N_s$, the RF precoder matrix $\mathbf{F}_{RF} \in C^{N_{Tx} \times N_{RF}}$, ρ designates the average received power and the channel noise is represented as n. The noise vector $n \in C^{N_{Tx} \times 1}$ is an additive white Gaussian function with a variance of σ_n^2 and zero mean.

The overall channel matrix, $\mathbf{H}^{total}$, on equation 2 can be represented using the singular value decomposition (SVD). In this instance, $\mathbf{H}^{total}$ is obtained through,

$$\mathbf{H}^{total} = \mathbf{U}\Lambda\mathbf{V}^H \tag{9}$$

where **U** and **V** are both unitary matrices measuring $N_{Rx} \times N_{Rx}$ and $N_{Tx} \times N_{Tx}$ where $\mathbf{U}\mathbf{U}^H = \mathbf{U}^H\mathbf{U} = I_{N_{Rx}}$ and $\mathbf{V}\mathbf{V}^H = \mathbf{V}^H\mathbf{V} = I_{N_{Tx}}$, respectively. Λ represents a diagonal matrix of $N_{Rx} \times N_{Tx}$ [22].

The precoder matrix is defined as $\mathbf{F} = \mathbf{V}[:1:N_s]$ for a fully digital structure. Albeit, instead of using a fully digital design, it will be implemented an hybrid system using an analog precoder, in order to avoid installing digital-analog converters (DAC) on every single antenna, thus reducing the hardware complexity whilst achieving a performance close to the design that employs a fully digital circuit.

The algorithm to be developed with the hybrid design will employ a smaller digital precoder. The baseband digital precoder is connected through several radio frequency chains to the analog precoder, responsible for generating the final signal that will be transmitted on each existent N_{Tx} antenna, as seen in figure 2.

The hybrid combiner **W** is obtained via $\mathbf{W} = \mathbf{W}_{RF}\mathbf{W}_{BB}$, representing the RF combiner $\mathbf{W}_{RF} \in C^{N_{Rx} \times N_{RF}^{Rx}}$ and the baseband combiner $\mathbf{W}_{BB} \in C^{N_{RF}^{Rx} \times N_s}$. Both matrices $\mathbf{F}_{RF}$ and $\mathbf{W}_{RF}$ are implemented in analog, where the RF signal processing will depend on the architecture that is selected and implemented [23].

Using the analog and the digital precoder matrices, the hybrid precoder design problem will be formulated as

$$\min_{\mathbf{F}_{RF},\mathbf{F}_{BB},\Phi} -\ln\det(\mathbf{I}_{N_{Rx}} + \frac{\rho}{P_N}\mathbf{H}^{total}\mathbf{F}_{RF}\mathbf{F}_{BB}^H\mathbf{F}_{RF}^H\mathbf{H}^{total^H}) \tag{10}$$

$$\text{subject to} \begin{cases} \left\| \mathbf{F}_{RF}\mathbf{F}_{BB} \right\|_F^2 \leq P_{Tx} \\ |\Phi(k)| = 1, k \in |1, ..., N_{RIS}| \\ \mathbf{F}_{RF} \in C^{N_{Tx} \times N_{RF}} \end{cases} \tag{11}$$

where the power per stream ρ suffers from noise power calculated using $P_N = \sigma^2$.

The problem on 10 must be solved under the constraints defined in 11, where $\mathbf{F}_{RF} \in C^{N_{Tx} \times N_{RF}}$ represents the set of matrices that will vary depending on the hybrid architecture to be adopted, since each set of precoding analog matrices are defined according to the RF structure that is implemented. The algorithm for the hybrid precoder must be designed to be able to handle the various RF architectures that can be implemented. The restriction imposed $\left\| \mathbf{F}_{RF}\mathbf{F}_{BB} \right\|_F^2 \leq P_{Tx}$ enforces the total power constraint at the transmitter.

The three restrictions render the Proximal Gradient algorithm difficult to apply all at once. Thus, the alternative is the implementation of Alternating Minimization.

In order to avoid the problem noted above, it will be used the proximal gradient algorithm [24] to firstly fix $\mathbf{F}_{RF}$ and Φ whilst solving over $\mathbf{F}_{BB}$ according to the expression

$$\min_{\mathbf{F}_{BB}} - \ln\det(\mathbf{I}_{N_{Rx}} + \frac{\rho}{P_N}\mathbf{H}^{total}\mathbf{F}_{RF}\mathbf{F}_{BB}^H\mathbf{F}_{RF}^H\mathbf{H}^{total^H}) \tag{12}$$

$$\text{subject to} \left\| \mathbf{F}_{RF}\mathbf{F}_{BB} \right\|_F^2 \leq P_{Tx}, (P_{Tx} = N_s) \tag{13}$$

the equation on 12 can be simplified by adopting $\widetilde{\mathbf{H}} = \mathbf{H}^{total}\mathbf{F}_{RF}$,

$$\min_{\mathbf{F}_{BB}} f(\mathbf{F}_{BB}) = - \ln\det(\mathbf{I}_{Ns} + \frac{\rho}{P_N}\mathbf{F}_{BB}^H\widetilde{\mathbf{H}}^H\widetilde{\mathbf{H}}\mathbf{F}_{BB}) \tag{14}$$

$$\text{subject to} \left\| \mathbf{F}_{RF}\mathbf{F}_{BB} \right\|_F^2 \leq P_{Tx} \tag{15}$$

the restriction on 15 can be integrated on the problem referenced in 14, resulting in

$$\min_{\mathbf{F}_{BB}} f(\mathbf{F}_{BB}) = - \ln\det(\mathbf{I}_{Ns} + \frac{\rho}{P_N}\mathbf{F}_{BB}^H\widetilde{\mathbf{H}}^H\widetilde{\mathbf{H}}\mathbf{F}_{BB}) + \underset{\|\mathbf{F}_{RF}\mathbf{F}_{BB}\|_F \leqslant P_{Tx}}{\mathbf{I}(\mathbf{F}_{BB})} \tag{16}$$

According to the expression deduced on 16 the baseband matrix can be calculated by using the proximal gradient algorithm [24],

$$\mathbf{F}_{BB}^{(t+1)} = prox_{\lambda \mathbf{I}_{\|\mathbf{F}_{RF}\mathbf{F}_{BB}\|_F \leqslant P_{Tx}}}[\mathbf{F}_{BB}^{(t)} - \nabla_{\mathbf{F}_{BB}^*} f(\mathbf{F}_{BB}^{(t)})] \tag{17}$$

the gradient needed in equation 17 for the expression $\mathbf{F}_{BB}^{(t+1)}$ can be obtained via:

$$\begin{aligned} \nabla_{\mathbf{F}_{BB}^*} f(\mathbf{F}_{BB}^{(t)}) = \frac{\partial f}{\partial \mathbf{F}_{BB}^*} &= -\frac{\rho}{P_N}\widetilde{\mathbf{H}}^H\widetilde{\mathbf{H}}\mathbf{F}_{BB}^{(t)}(\mathbf{I}_{Ns} + \frac{\rho}{\rho_N}\mathbf{F}_{BB}^{(t)^H}\widetilde{\mathbf{H}}^H\widetilde{\mathbf{H}}\mathbf{F}_{BB}{}^{(t)})^{-1} \\ &= -\frac{\rho}{P_N}\mathbf{F}_{RF}^H\mathbf{H}^{total^H}\mathbf{H}^{total}\mathbf{F}_{RF}\mathbf{F}_{BB}^{(t)}(\mathbf{I}_{Ns} + \frac{\rho}{P_N}\mathbf{F}_{BB}^{(t)^H}\mathbf{F}_{RF}^H\mathbf{H}^{total^H}\mathbf{H}^{total}\mathbf{F}_{RF}\mathbf{F}_{BB}^{(t)})^{-1} \end{aligned} \tag{18}$$

The equation 18 enables the problem to be optimized, following the previous methodology and allowing the baseband matrix to be obtained, through the calculation of the proximal operator in equation 17 by normalizing the matrix $\mathbf{F}_{BB}$. As a result, the minimization expression with fixed $\mathbf{F}_{BB}$ is expressed as

$$\begin{aligned} &\min_{\mathbf{F}_{RF},\Phi} - \ln\det(\mathbf{I}_{N_{Rx}} + \frac{\rho}{P_N}\mathbf{H}^{total}\mathbf{F}_{RF}\mathbf{F}_{BB}\mathbf{F}_{BB}^H\mathbf{F}_{RF}^H\mathbf{H}^{total^H}) = \\ &= - \ln\det(\mathbf{I}_{Ns} + \frac{\rho}{P_N}\mathbf{F}_{BB}^H\mathbf{F}_{RF}^H\mathbf{H}^{total^H}\mathbf{H}^{total}\mathbf{F}_{RF}\mathbf{F}_{BB}) \end{aligned} \tag{19}$$

$$\text{subject to} \begin{cases} \left\| \mathbf{F}_{RF} \mathbf{F}_{BB} \right\|_F^2 \leq P_{Tx} \\ \mathbf{F}_{RF} \in C^{N_{Tx} \times N_{RF}} \\ |\Phi(k)| = 1 \end{cases} \tag{20}$$

The problem formulated on 19 and20 allows to apply the proximal gradient to the phase shifting matrix, Φ, and the RF precoder ,$\mathbf{F}_{RF}$, for $t+1$ iteration in conjunction

$$\begin{cases} \Phi^{(t+1)} = prox_{\mu I_{(.)=1}}(\Phi^{(t)} - \lambda \nabla_{\Phi^*} f(\Phi^{(t)}) \\ \mathbf{F}_{RF}^{(t+1)} = prox_{\mu I_{\left\| . \right\|_F^2 \leq P_{Tx}}}(\mathbf{F}_{RF}^{(t)} - \lambda \nabla_{\mathbf{F}_{RF}^*} f(\mathbf{F}_{RF}{}^{(t)}) \end{cases} \tag{21}$$

the proximal operator in the expression $\Phi^{(t+1)}$ in 21 is calculated by normalizing each element in the vector, whereas the proximal operator for the expression $\mathbf{F}_{RF}^{(t+1)}$ is obtained through the projection of the $\mathbf{F}_{RF}$ matrix. The calculation of the RF precoder depends on the architecture in use. The RF constraint and the implementation of the RF precoder will be followed according to [25]. Algorithm 1 shows all steps of the hybrid precoder implemented.

Hybrid Precoder Algorithm
FOR $t = 0, ...T-1$
Compute baseband precoder, $\mathbf{F}_{BB}$, using equation 17
Compute RIS matrix, Φ using equation 21
Compute the precoder matrix $\mathbf{F}_{RF}$ using equation 21
ENDFOR
Generate output precoder matrix $\mathbf{F} = \mathbf{F}_{RF}\mathbf{F}_{BB}$

Table 1. Proposed hybrid precoder algorithm.

3.2. Fully and Partially Connected Hybrid Design

The fully connected (FC) hybrid design divides the signal coming from each RF chain into various phase shifters. Subsequently, the signal conveyed from each phase shifter from different RF chains is combined before its transmission in each antenna. The architecture with a fully connected design has an elevated hardware complexity in comparison with the partially connected structure.

The partially connected (PC) design, also denominated as Array of subarrays design (AoSA), divides the signal from each RF chain towards the phase shifters in use. Each phase shifter is connected directly towards the transmission antenna.

3.3. Unquantized Phase Shifters (UPS)

The architecture that uses unquantized phase shifters can be considered a reference benchmark when comparing it to the structure that employs quantized phase shifters, since UPS employs phase shifters with an infinite resolution. As a result, unquantized phase shifters provide a solution considered to be ideal and closer to the fully digital RIS architecture, applying a phase between $[0, 2\pi)$.

3.4. Quantized Phase Shifters (QPS)

Whilst UPS demonstrates an ideal solution, quantized phase shifters demonstrate a more real-life case since the number of phase shifts that can be implemented is finite. The phase shifters have N_b bits in use, each with 2^{N_b} phases available.

3.5. Switches

The switches will determinate which antenna the signal will pass through. This case is more extreme in relation to the RF precoder with phase shifters, since not all antennas will be connected, thus affecting the efficiency of the transmitted signal.

3.6. Antenna Selection

The hybrid architecture that employs antenna selection in the RF precoder presents a lower complexity than the RF precoder that uses phase shifters. Amongst all the antennas connected per RF chain, the RF precoder will select only one antenna. This structure presents an extreme case in comparison with the design that employs phase shifters due to the fact that only one antenna will be in use per RF chain. Even though the complexity is drastically reduced for employing only one antenna in each RF chain, the overall performance will be impacted significantly.

3.7. Array of Subarrays (AoSA)

The RF precoder that employs Array of subarray (AoSA) divides per the number of active RF chains a group of antennas, denominated as subarrays. The number of subarrays, N_{SA}, is set as $N_{SA} = N_{RF}$, the size of each subarray is given as $N_{SA,Tx} = \frac{N_{Tx}}{N_{SA}}$, thus it divides the number of transmitter antennas equally per each subset [25].

The complexity of AoSA architecture depends on the number of subarrays connected in each RF chain. In order to improve performance as well as have a manageable complexity, the number of subarrays is limited in each connection, denominated as L_{max}. When there is 1 subarray for each RF chain, the AoSA architecture in study corresponds to the partially connected structure.

3.8. Dynamic Array of Subarrays (DAoSA)

Dynamic array of subarray is based on the AoSA design. Whereas in the structure utilizing AoSA each RF is directly connected to a subset of antennas via phase shifters or other method described above, the DAoSA structure links the RF chain to a switch, allowing the option of choosing which subset of antennas the RF chain connects to. The existent transmitted antennas are divided per the existent RF chains, represented as L_t, therefore the number of switches is obtained through $\alpha_s = L_t^2$. Moreover, DAoSA also allows choosing the number of subarrays that are connected in each RF chains, allowing different chains to have different numbers of transmit antennas, whilst AoSA divided the number of antennas equally per RF chain.

A dynamic AoSA design implemented in hybrid precoding allows a free and dynamic control since it does not have a fixed circuit, seen in AoSA and FC structure, thus offering better power consumption and higher spectral efficiency [26].

4. Numerical Results

The results obtained in this paper were acquired through the development of a simulator in Matlab based on the Monte Carlo method to mimic an indoor environment scenario in order to evaluate the performance of the algorithm that opmitizes the hybrid precoder and the RIS, derived in the previous section, using a THz frequency band in order to enable communications in 6G. Besides that, it will be analysed and evaluated the impact of the different hybrid architectures, such as phase shifters, AoSA or DAoSA.

The scenario in use has the frequency set to $f = 300$ GHz, and will only have the indirect path active, Transmitter-RIS-Receiver. Path loss exponent between Tx and RIS is equal to the path loss between RIS and Rx, equaling $n_{Tx-RIS} = n_{RIS-Rx} = 2.05$, the rice factor is set to $K_{rice} = 10$ and the bandwidth $B = 8$ GHz, retrieved from [27]. The distance between adjacent antenna elements in the transmitter, d_{Tx}, in the RIS, d_{RIS}, and in the receiver, d_{Rx} were assumed to be $d_{Tx} = d_{Rx} = d_{RIS} = 0.0054$ m. Thus the area of each RIS element is $A_{RIS} = d_{RIS}^2$. The coordinates of the BS, RIS array and the user are defined as (0,0), (2 m,2 m), and (d,0), respectively, where d represents the distance between Tx-Rx.

The number of NLoS signal paths is set to 3, with $N_{Rx} = 36$ receiver antennas, $N_{RIS} = 512$ RIS elements, $N_s = 2$ symbols per transmission and $N_{Tx} = 512$ transmit antennas, with no direct path between the transceiver and receiver.

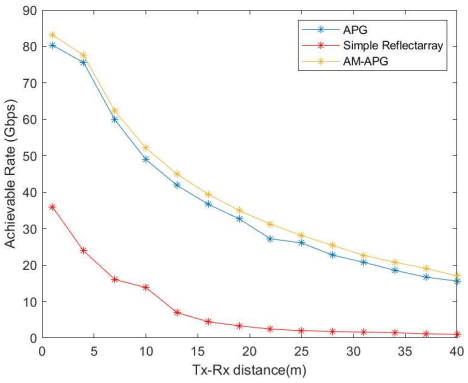

Figure 3. Achievable rate versus distance between Transmitter and Receiver for various schemes.

Figure 3 compares the achievable rate (Gbps) whilst increasing the distance between the transmitter and receiver using Alternating Minimization with non monotone Accelerated Proximal Gradient for Precoder and RIS (AM-APG), APG [16] and simple reflectarray algorithms.

The simple reflectarray structure models the worst-case scenario due to the fact that even though this algorithm uses a fully digital SVD precoder, it also employs a fixed RIS that functions as simple mirror since it will only blindly reflect the carrier signal.

The AM-APG algorithm, based on the proposed accelerated proximal gradient (APG) jointly to all RIS matrices, is a version of the algorithm presented in chapter 3 where it will automatically compute the digital precoder matrix $\mathbf{F}$, since there is no $\mathbf{F}_{RF}$ matrix. The AM-APG will provide the best case scenario, since the algorithm employs fully digital precoder and RIS structure.

Whilst the AM-APG algorithm represents a fully digital RIS scenario since it employs a digital precoder, thus has a better achievable rate than hybrid scenarios that use analog precoders, the various simulations that were completed aim to find the most suitable hybrid precoder so that its implementation is physically feasible, in regards to its complexity level and material costs. In order to find the optimal hybrid architecture for this scenario, all the different configurations that were mentioned above will be tested in detail.

4.1. Phase Shifters - RIS Quantization Bits:

The following figures 4 and 5 depict the achievable rate using phase shifters with 3 bit quantization in the RF precoder for $N_{RIS} = 512$ whilst comparing different RIS quantization bits.

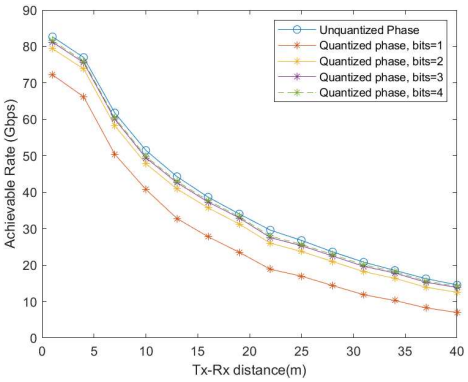

Figure 4. Achievable rate vs distance between Tx-Rx for fully connected precoders using quantized phase shifters, in comparison with UPS, using $N_{RIS} = 512$.

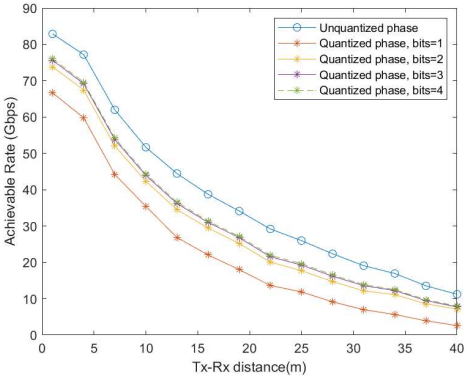

Figure 5. Achievable rate vs distance between Tx-Rx for partially connected precoders using quantized phase shifters, in comparison with UPS, considering $N_{RIS} = 512$.

Figure 4 demonstrates the curves obtained using different quantization bits in the RIS. The curves for the quantized phase shifters in a fully connected architecture are being compared towards the unquantized phase shifters structure. Figure 5 also employs differing quantization bits in the RIS and 3 bit quantization in the RF precoder for quantized phase shifters in a partially connected structure.

The use of 2 quantization bits on the reconfigurable intelligent surface emulates significantly close the achievable rate recorded using the unquantized phase shifter, seen in figure 4. The use of 3 bits is almost identical to the result obtained with higher quantization bits, thus 3 bits are suitable to achieve the ideal optimization on the phase shifter. The only case that worsens significantly the achievable rate is with 1 bit quantization.

Figure 5 demonstrates lower achievable rates in comparison with the values for the same RIS quantization bits used in figure 4 as a result of the current antennas not being connected to all existing subarrays. The 1 bit quantization at 1 meter of distance has an achievable rate of 67 Gbps. Upping the quantization bits to 3 or 4 at 1 meter of distance the achievable rate is 76 Gbps. This type of precoder benefits from using 3 bit quantization in order to achieve the best results without jeopardizing the quality of the communication between the transmitter and receiver.

4.2. Phase Shifter - Precoder Quantization Bits:

The RF precoder that implements phase shifters in its structure also quantizes its phases in the precoder, thus in the following figures 6 and 7 the RIS use a 3 bit quantization and the quantization in the RF precoder will vary.

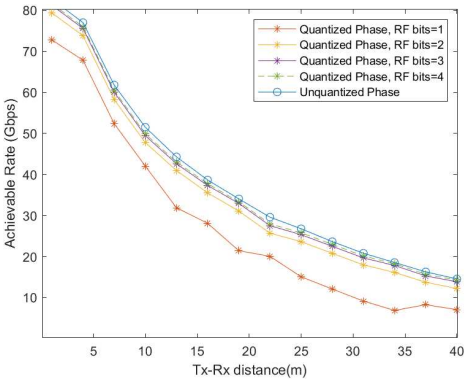

Figure 6. Achievable rate versus distance between Tx-Rx for fully connected quantized RF precoders, in comparison with unquantized phase shifter, considering $N_{RIS} = 512$.

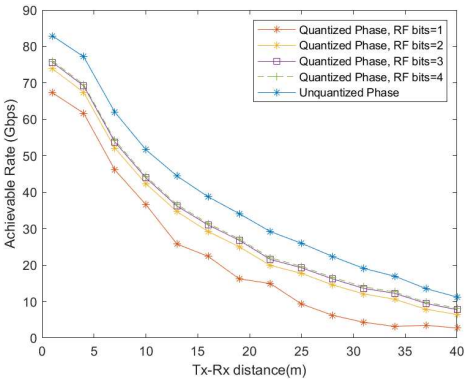

Figure 7. Achievable rate versus distance between Tx-Rx for partially connected quantized RF precoders, in comparison with unquantized phase shifter, considering $N_{RIS} = 512$.

Figures 6 and 7 represent different quantization bits in the RF precoder for fully and partially connected RF chains, respectively. In both figures, the use of 3 bit quantization presents the best result for implementation, since the curves for 3 and 4 bit quantization are virtually identical.

Therefore, in both cases the most beneficial quantization bits to be implemented in the RF precoder as well as in the RIS is 3 bits. It presents a near ideal solution without compromising the complexity of the hardware for not requiring the deployment of costly phase-shifters in RIS and in the precoder that uses phases shifters on its structure.

4.3. Dynamic Array of Subarrays

The hybrid precoder design using DAoSA architecture uses free dynamic array of subarrays, as represented in figure 8. Using AM-APG curve as reference, all the curves have similar rates from 1 up to 16 meters of distance between Tx-Rx, going from 83 Gbps

downwards to 39 Gbps. After the distance surpasses 16 meters, the differences are viewable in figure 8. The greater the number of subarrays connected in each RF chain, the higher the achievable rate.

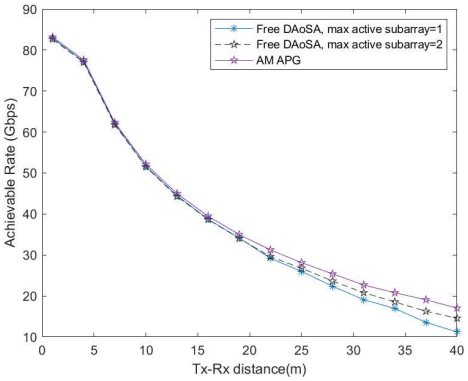

Figure 8. Study of Achievable rate (Gbps) using free dynamic array of subarrays whilst increasing the distance between Tx and Rx.

4.4. All Hybrid architectures

Combining all hybrid architectures for $N_{RIS} = 512$, represented in figure 9, and considering fully connected structures, the designs that manage to obtain the rates closer to those obtained with AM-APG design are quantized and unquantized phase shifters.

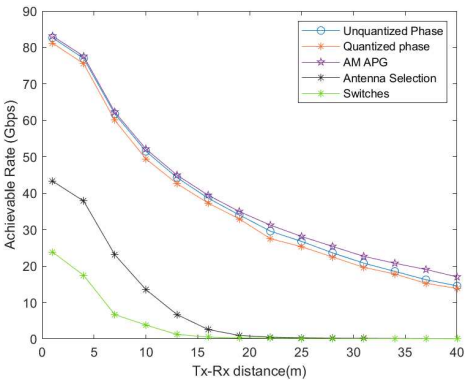

Figure 9. Study of Achievable rate (Gbps) on all fully connected hybrid designs with $N_{RIS} = 512$, whilst increasing the distance between Tx and Rx.

The scenarios that do not use phase shifters present the worst rates whilst increasing the distance between the transmitter and the receiver. This is the case of the hybrid design that employs antenna selection or switches where the coverage range is severely limited.

In figure 10, it is demonstrated all the partially connected hybrid designs for $N_{RIS} = 512$ and using 3 quantization bits.

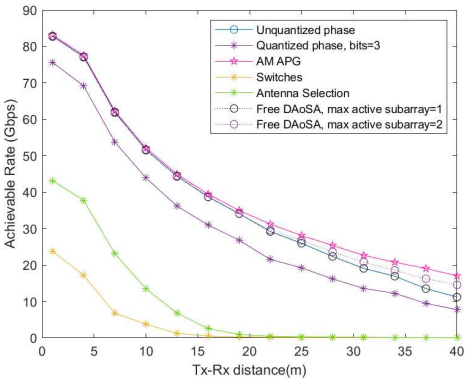

Figure 10. Study of Achievable rate (Gbps) for partially connected hybrid designs with $N_{RIS} = 512$, whilst increasing the distance between Tx-Rx.

The design that employs unquantized phase shifters achieves exactly the same rates as the architecture that uses dynamic array of subarrays with one subarray per RF chain. When there is more than one subarray per RF chain free dynamic AoSA offers higher rates when the distance increases .

Switches and antenna selection present the same behaviour in both figures 9 and 10. However, quantized phase shifters, for the same quantization bits in use, have lower achievable rates using partially connected hybrid precoders in comparison with their counterpart shown in figure 9 that employ fully connected hybrid precoders.

5. Conclusion

In this article it was examined and studied a RIS-supported UM-MIMO scheme aimed at improving the communication system for THz frequencies in order to support 6G communications. The system was designed to test several distinct hybrid precoders which were evaluated to determine the most adequate for implementation that would return an achievable rate similar to an all-digital precoder, while also reducing the overall implementation complexity and cost. In addition, the analysis of the quantization bits in each RIS element was also conducted in order to assess the impact on the received signal and the effect on the output signal generated towards the end user.

The simulations for the THz frequency using 300 GHz illustrate the impact of the high absorption losses along the wave path, thereby making it required to deploy a greater number of RIS elements, transmitter and receiver antennas, to overcome and allow the forwarding of the inbound signal. The performance of the hybrid precoder is the same, and in addition, the phase shift that is quantized using 3 bits in the RF precoder and in the RIS delivers the most achievable rate. Nevertheless, the RIS with lower resolution using only 2 bits of quantization may suffice to achieve comparable unquantized phase shift rates, therefore decreasing its implementation cost.

The optimal hybrid precoder designs quantized phase shifter and free dynamic array of subarray present the best achievable rates for the THz band. Both frameworks are similar to each other since the RF precoder employs phase shifts, however the capability of the free DAoSA to modify its structure by allowing differing RF subarrays to be connected per antenna will drastically improve the performance of the Tx-Rx link.

In conclusion, the results obtained provide information about the importance of implementing RIS in order to improve the quality of communication systems in future wireless networks when the LoS is obstructed, as was documented in the literature that implemented RIS-empowered UM-MIMO systems. However, the existing limitations in the phase resolution of RIS elements and its implementation cost in a realistic environment still pose a number of concerns. While theoretically the analysis conducted demonstrates

a potential for success, the elevated expense of installing RIS and the overall energy consumption still require further studies.

The work presented in this article can be further extended by focusing on and broadening the RIS-assisted UM-MIMO communication system for THz frequencies while using a hybrid precoder that has been devised over the course of this dissertation through the design of a framework to handle multiple end users. In the present study only a single user equipment was devised to be in use towards the scheme planned. The RIS-supported UM-MIMO structure could be developed in order to have multiple UEs on the same network. An additional framework to be implemented would allow multiple RIS panels, thus creating a larger and larger network interconnected via a BS to multiple RIS, and in return route the signal to the multiusers available on the same network.

References

1. Akyildiz, I.F.; Han, C.; Nie, S. Combating the Distance Problem in the Millimeter Wave and Terahertz Frequency Bands. *IEEE Communications Magazine* **2018**, *56*, 102–108. https://doi.org/10.1109/MCOM.2018.1700928.
2. BR. Recommendation ITU-R M.2083-0 IMT Vision-Framework and overall objectives of the future development of IMT for 2020 and beyond M Series Mobile, radiodetermination, amateur and related satellite services. Technical report, Internation Telecommunication Union, 2015.
3. The Next Hyper Connected Experience for All. Technical report, Samsung, 2020.
4. Spectrum Expanding the Frontier 6G. Technical report, Samsung, 2022.
5. Dash, S.; Psomas, C.; Krikidis, I.; Akyildiz, I.F.; Pitsillides, A. Active Control of THz Waves in Wireless Environments using Graphene-based RIS. *IEEE Transactions on Antennas and Propagation* **2022**, pp. 1–3. https://doi.org/10.1109/TAP.2022.3142272.
6. Han, C.; Wu, Y.; Chen, Z.; Wang, X. Terahertz Communications (TeraCom): Challenges and Impact on 6G Wireless Systems, 2019. https://doi.org/10.48550/ARXIV.1912.06040.
7. Björnson, E.; Özdogan, Ö.; Larsson, E.G. Reconfigurable Intelligent Surfaces: Three Myths and Two Critical Questions. *IEEE Communications Magazine*.
8. Gong, S.; Lu, X.; Hoang, D.T.; Niyato, D.; Shu, L.; Kim, D.I.; Liang, Y.C. Toward Smart Wireless Communications via Intelligent Reflecting Surfaces: A Contemporary Survey. *IEEE Communications Surveys &amp Tutorials* **2020**, *22*, 2283–2314. https://doi.org/10.1109/comst.2020.3004197.
9. Wu, Q.; Zhang, R. Towards Smart and Reconfigurable Environment: Intelligent Reflecting Surface Aided Wireless Network. *IEEE Communications Magazine* **2020**, *58*, 106–112. https://doi.org/10.1109/MCOM.001.1900107.
10. Basar, E.; Yildirim, I. Reconfigurable Intelligent Surfaces for Future Wireless Networks: A Channel Modeling Perspective. *IEEE Wireless Communications* **2021**, *28*, 108–114. https://doi.org/10.1109/MWC.001.2000338.
11. Basar, E.; Yildirim, I.; Kilinc, F. Indoor and Outdoor Physical Channel Modeling and Efficient Positioning for Reconfigurable Intelligent Surfaces in mmWave Bands. *IEEE Transactions on Communications* **2021**, *69*, 8600–8611. https://doi.org/10.1109/TCOMM.2021.3113954.
12. Dash, S.; Psomas, C.; Krikidis, I.; Akyildiz, I.F.; Pitsillides, A. Active Control of THz Waves in Wireless Environments using Graphene-based RIS. *IEEE Transactions on Antennas and Propagation* **2022**, pp. 1–1. https://doi.org/10.1109/tap.2022.3142272.
13. Di, B.; Zhang, H.; Song, L.; Li, Y.; Han, Z.; Poor, H.V. Hybrid Beamforming for Reconfigurable Intelligent Surface based Multi-User Communications: Achievable Rates with Limited Discrete Phase Shifts. *IEEE Journal on Selected Areas in Communications* **2020**, *38*, 1809–1822. https://doi.org/10.1109/JSAC.2020.3000813.
14. Larsson, E.G.; Edfors, O.; Tufvesson, F.; Marzetta, T.L. Massive MIMO for next generation wireless systems. *IEEE Communications Magazine* **2014**, *52*, 186–195. https://doi.org/10.1109/MCOM.2014.6736761.
15. Chataut, R.; Akl, R. Massive MIMO Systems for 5G and Beyond Networks—Overview, Recent Trends, Challenges, and Future Research Direction. *Sensors* **2020**, *20*, 2753. https://doi.org/10.3390/s20102753.
16. Praia, J.; Pavia, J.P.; Souto, N.; Ribeiro, M. Phase Shift Optimization Algorithm for Achievable Rate Maximization in Reconfigurable Intelligent Surface-Assisted THz Communications. *Electronics* **2021**, *11*, 18. https://doi.org/10.3390/electronics11010018.
17. Jayaweera, S.; Poor, H. Capacity of multiple-antenna systems with both receiver and transmitter channel state information. *IEEE Transactions on Information Theory* **2003**, *49*, 2697–2709. https://doi.org/10.1109/TIT.2003.817479.
18. Saleh, A.; Valenzuela, R. A Statistical Model for Indoor Multipath Propagation. *IEEE Journal on Selected Areas in Communications* **1987**, *5*, 128–137. https://doi.org/10.1109/JSAC.1987.1146527.
19. Ayach, O.E.; Rajagopal, S.; Abu-Surra, S.; Pi, Z.; Heath, R.W. Spatially Sparse Precoding in Millimeter Wave MIMO Systems. *IEEE Transactions on Wireless Communications* **2014**, *13*, 1499–1513. https://doi.org/10.1109/TWC.2014.011714.130846.
20. Dovelos, K.; Assimonis, S.D.; Ngo, H.Q.; Bellalta, B.; Matthaiou, M. Intelligent Reflecting Surfaces at Terahertz Bands: Channel Modeling and Analysis. *2021 IEEE International Conference on Communications Workshops, ICC Workshops 2021 - Proceedings* **2021**. https://doi.org/10.1109/ICCWorkshops50388.2021.9473890.
21. Ren, J.; Vaughan, R.G. Rice Factor Estimation from the Channel Phase. *IEEE Transactions on Wireless Communications* **2012**, *11*, 1976–1980. https://doi.org/10.1109/TWC.2012.040412.091208.

22. Lin, Y.P. On the Quantization of Phase Shifters for Hybrid Precoding Systems. *IEEE Transactions on Signal Processing* **2017**, *65*, 2237–2246. https://doi.org/10.1109/TSP.2016.2646659.
23. Méndez-Rial, R.; Rusu, C.; González-Prelcic, N.; Alkhateeb, A.; Heath, R.W. Hybrid MIMO Architectures for Millimeter Wave Communications: Phase Shifters or Switches? *IEEE Access* **2016**, *4*, 247–267. https://doi.org/10.1109/ACCESS.2015.2514261.
24. Miguel, J.; Praia, R. Um projeto de sistema de comunicações com reconhecimento de contexto para a banda THz. Master's thesis, Iscte - Instituto Universitário de Lisboa, 2021. https://doi.org/10071/24172.
25. Pavia, J.P.; Velez, V.; Ferreira, R.; Souto, N.; Ribeiro, M.; Silva, J.; Dinis, R. Low Complexity Hybrid Precoding Designs for Multiuser mmWave/THz Ultra Massive MIMO Systems. arXiv, 2021. https://doi.org/10.48550/ARXIV.2107.11499.
26. Yan, L.; Han, C.; Yuan, J. A Dynamic Array-of-Subarrays Architecture and Hybrid Precoding Algorithms for Terahertz Wireless Communications. *IEEE Journal on Selected Areas in Communications* **2020**, *38*, 2041–2056. https://doi.org/10.1109/JSAC.2020.3000876.
27. Xing, Y.; Rappaport, T.S.; Ghosh, A. Millimeter Wave and Sub-THz Indoor Radio Propagation Channel Measurements, Models, and Comparisons in an Office Environment. *IEEE Communications Letters* **2021**, *25*, 3151–3155. https://doi.org/10.1109/lcomm.2021.3088264.

APPENDIX B

28 GHz Scenario

B.1. Simple Reflectarray

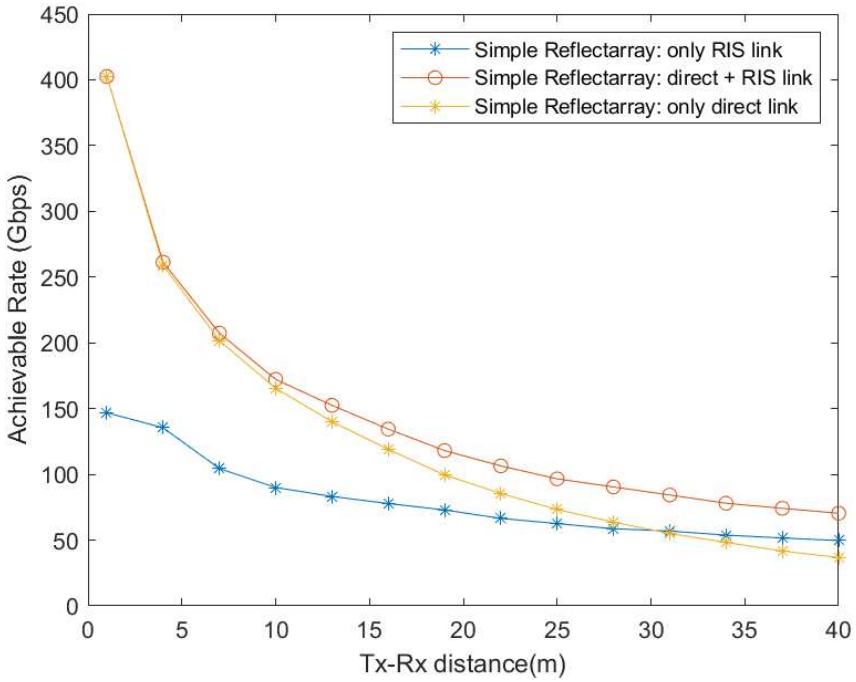

FIGURE B.1. Study of Achievable rate (Gbps) using simple reflectarrays for $N_{RIS} = 256$, whilst increasing the distance between Tx and Rx.

B.2. Hybrid Precoder - Phase Shifter

Figure B.5 compares the results obtained in figure B.4 and shows the different curves gathered using unquantized phase shifters, either fully or partially connected, and how the channel propagation varies depending on the link that are in use. Either both the RIS and the direct link are activated, or only the RIS or the direct link. As was expected, the connection that uses both links presents the best coverage overall.

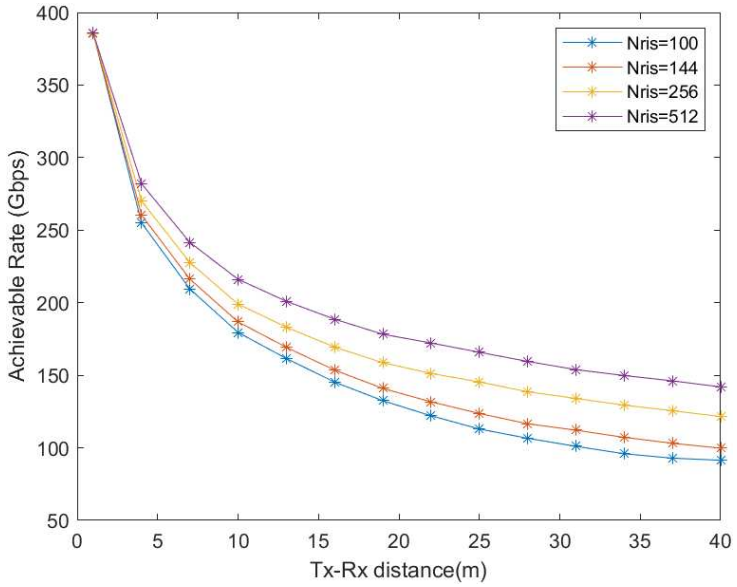

FIGURE B.2. Study of Achievable rate (Gbps) for different RIS elements using unquantized phase shifters partially connected, whilst increasing the distance between Tx and Rx,with RIS and direct link in use.

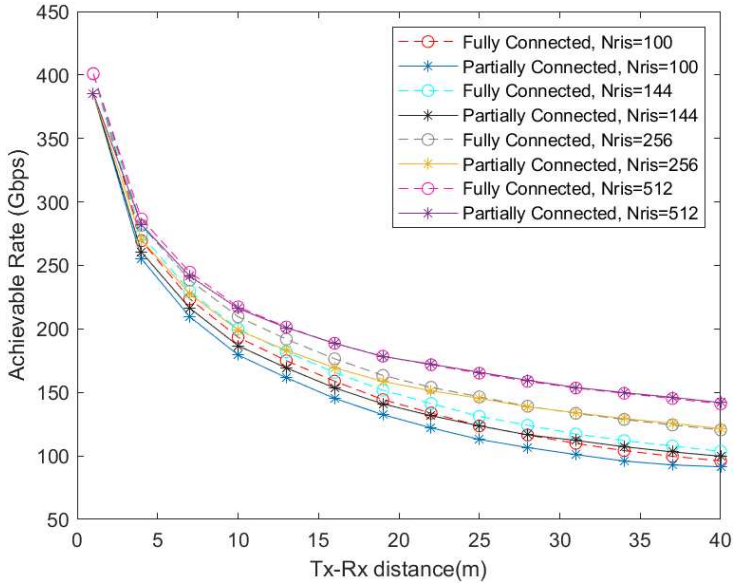

FIGURE B.3. Study of Achievable rate (Gbps) for different RIS elements comparing unquantized phase shifters partially and fully connected, whilst increasing the distance between Tx and Rx, with RIS and direct link in use.

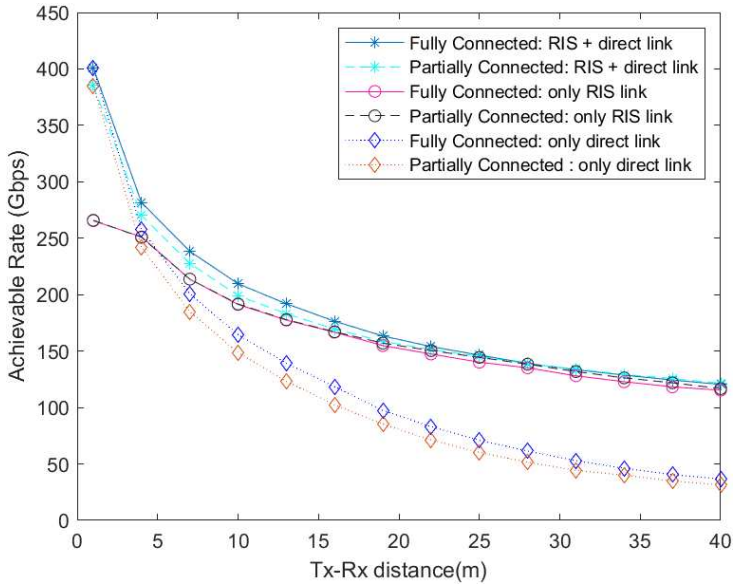

FIGURE B.4. Study of Achievable rate (Gbps) for unquantized phase shifters partially and fully connected with $N_{RIS} = 256$, whilst increasing the distance between Tx and Rx.

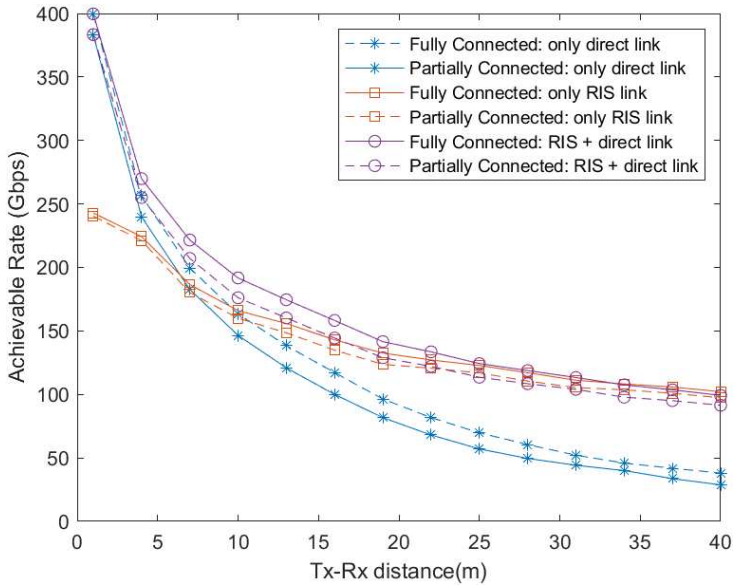

FIGURE B.5. Study of Achievable rate (Gbps) for quantized phase shifters partially and fully connected with $N_{RIS} = 256$, whilst increasing the distance between Tx and Rx.

B.3. Hybrid Precoder - DAoSA

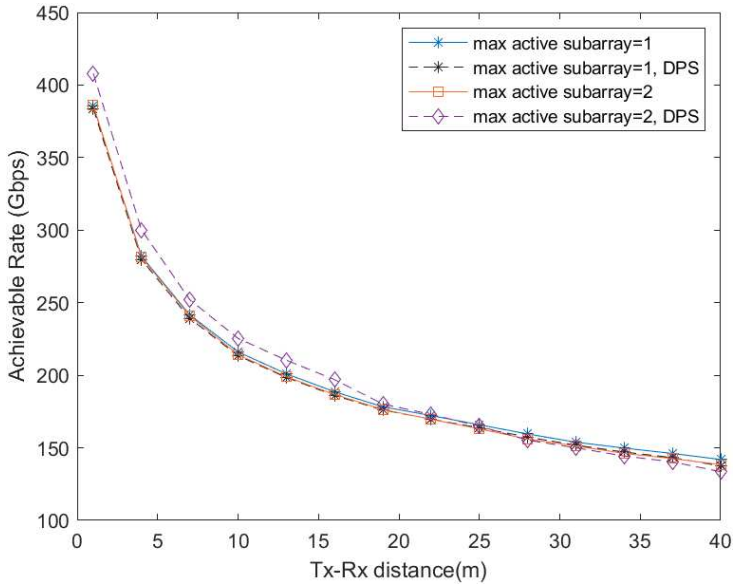

FIGURE B.6. Study of Achievable rate (Gbps) for adjacent dynamic array of subarrays for $N_{RIS} = 512$, whilst increasing the distance between Tx and Rx.

Figure B.6 demonstrates the curves obtained with adjacent dynamic AoSA with max active subarrays 1 and 2 ,as well as single or double phase shifters in use. The use of DPS provides better coverage when there are 2 subarrays per RF chain, thus it achieves rates of 408 when the distance is only 1 meter from Tx-Rx. When the distance increases to 28 meters, it records 155.9 Gbps, whereas the adjacent DAoSA with one single phase shifter achieves 155 Gbps. Thus, the bigger the distance, the deployment of DPS will not be advantageous.

B.4. Hybrid Architectures - Only RIS activated

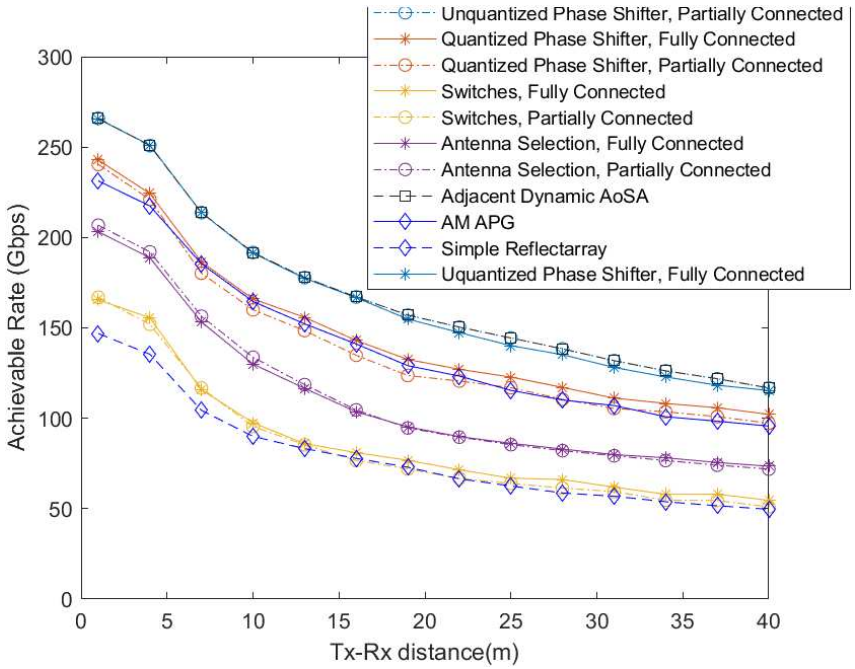

FIGURE B.7. Study of Achievable rate (Gbps) for different hybrid precoders for $N_{RIS} = 256$, whilst increasing the distance between Tx and Rx, with only RIS link in use.

APPENDIX C

Transmitter Power

C.1. Unquantized Phase Shifter

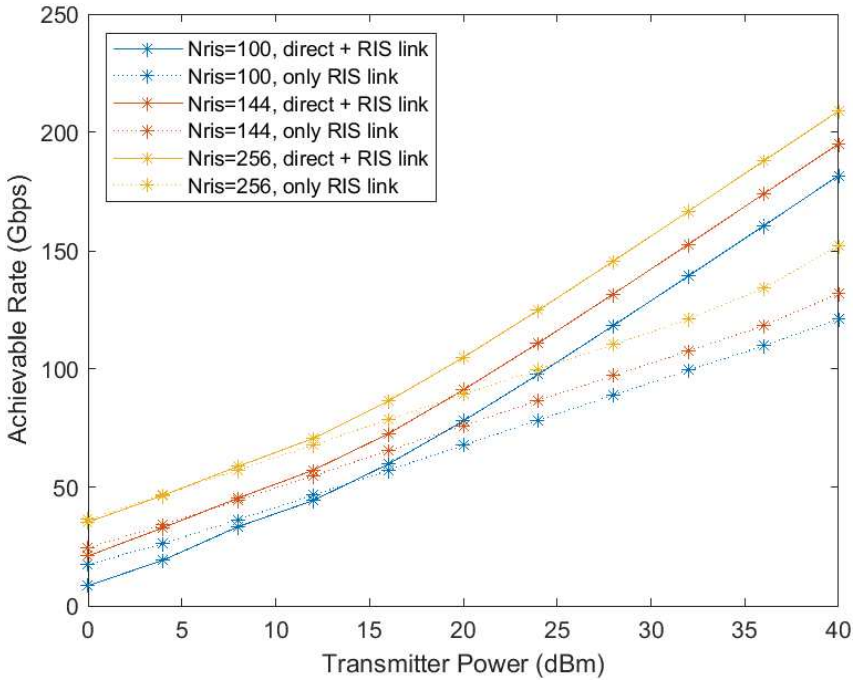

FIGURE C.1. Study of Achievable rate (Gbps) for Unquantized Phase Shifters fully connected, whilst increasing the transmitter power between Tx and Rx, for Tx-Rx=10 m and RIS 5 meters from Tx, direct + RIS link activated.

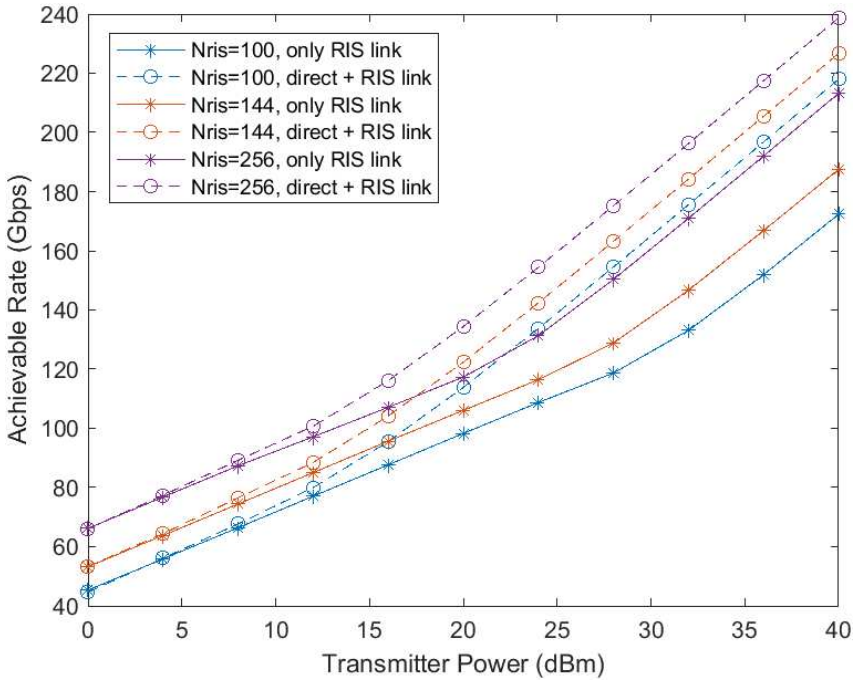

FIGURE C.2. Study of Achievable rate (Gbps) for Unquantized Phase Shifters fully connected, whilst increasing the transmitter power between Tx and Rx, for Tx-Rx=10 m and RIS 1 meter from Rx, direct + RIS link activated.

C.2. Free Dynamic Array of Subarrays

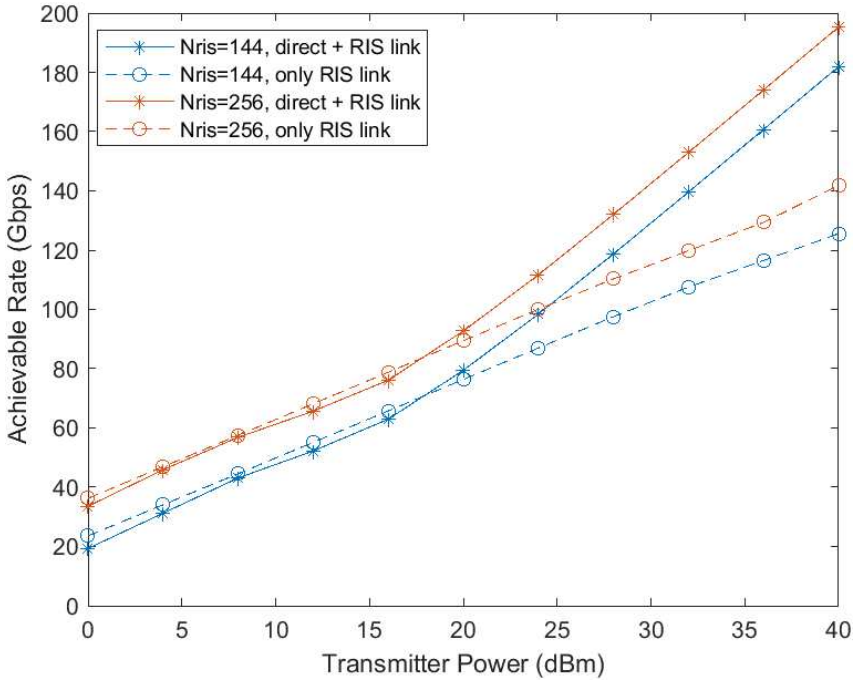

FIGURE C.3. Study of Achievable rate (Gbps) for free dynamic AoSA with 1 subaray per RF chain whilst increasing the transmitter power between Tx and Rx, for Tx-Rx=10 m and RIS 5 meters from Tx, direct + RIS link activated.

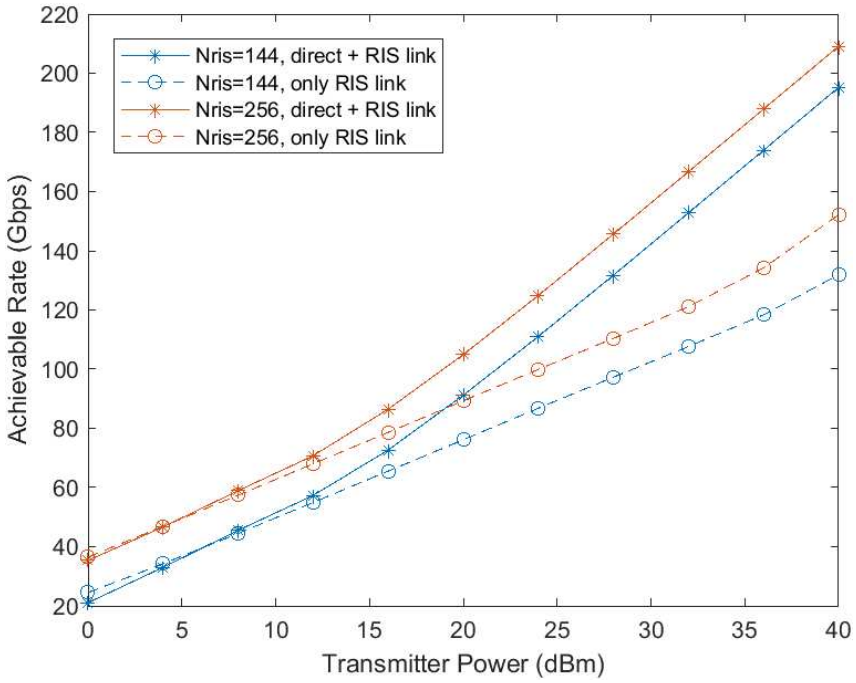

FIGURE C.4. Study of Achievable rate (Gbps) for free dynamic AoSA with 2 subarrays per RF chain whilst increasing the transmitter power between Tx and Rx, for Tx-Rx=10 m and RIS 5 meters from Tx, direct + RIS link activated.

APPENDIX D

300 GHz Scenario

Study of different algorithms for the scenario in use with $f = 300$ GHz.

D.1. Simple Reflectarrays

The figure D.1 demonstrates how the use of the blind RIS affects the achievable rate depending on the number of RIS being deployed.

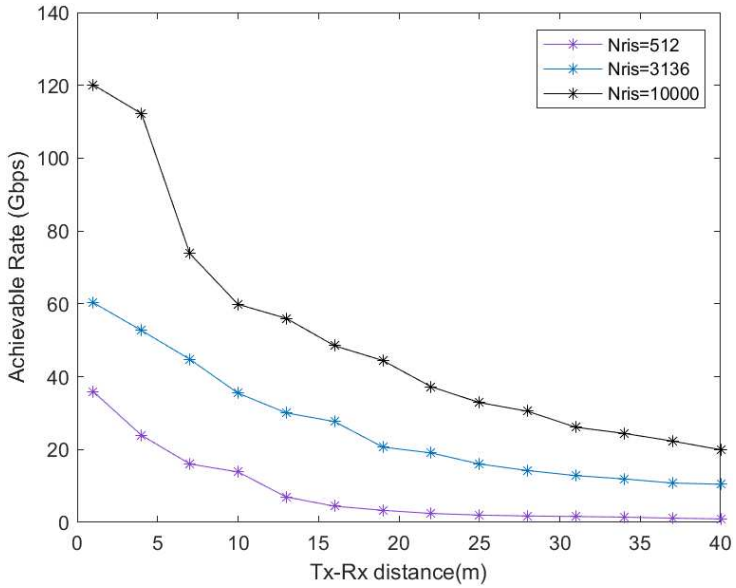

FIGURE D.1. Achievable rate (Gbps) vs distance between Tx-Rx using Simple Reflectors for different RIS elements.

D.2. AM-APG

The fully digital RIS in figure D.2 shows how different RIS elements afect the curves obtained that represent the rates whilst increasing the distance between Tx-RX.

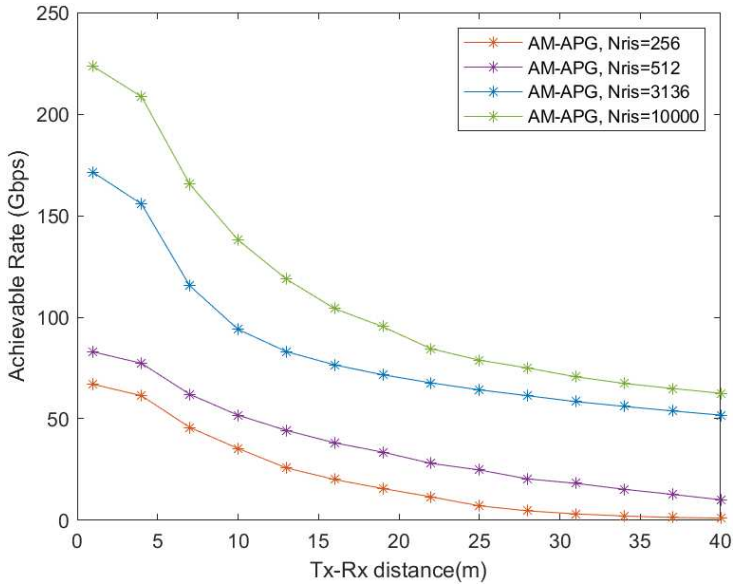

FIGURE D.2. Study of Achievable rate (Gbps) for fully digital RIS algorithm, AM-APG, for different RIS elements whilst increasing the distance between Tx and Rx.

D.3. Hybrid Achitectures

D.3.1. Switches

Figure D.3 represents in detail the hybrid precoder that employs fully connected switches for different RIS elements.

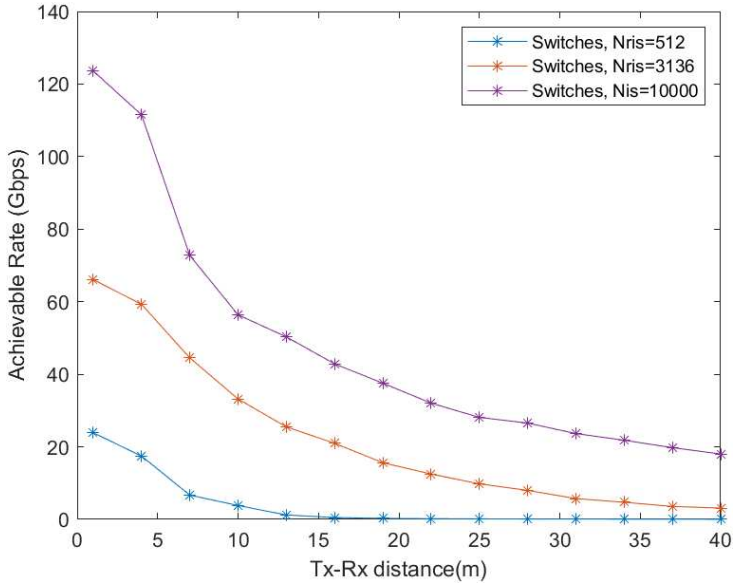

FIGURE D.3. Study of Achievable rate (Gbps) using fully connected switches, for different RIS elements whilst increasing the distance between Tx and Rx.

Figure D.4 demonstrates the curves obtained through the usage of the the hybrid precoder that employs partially connected switches for different RIS elements.

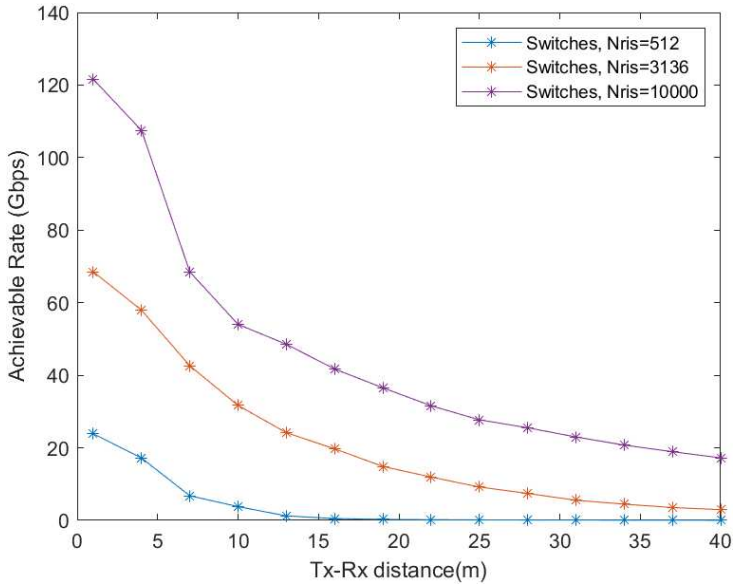

FIGURE D.4. Study of Achievable rate (Gbps) using partially connected switches, for different RIS elements whilst increasing the distance between Tx and Rx.

D.3.2. Antenna Selection

Figure D.5 uses partially connected antenna selection for different RIS elements.

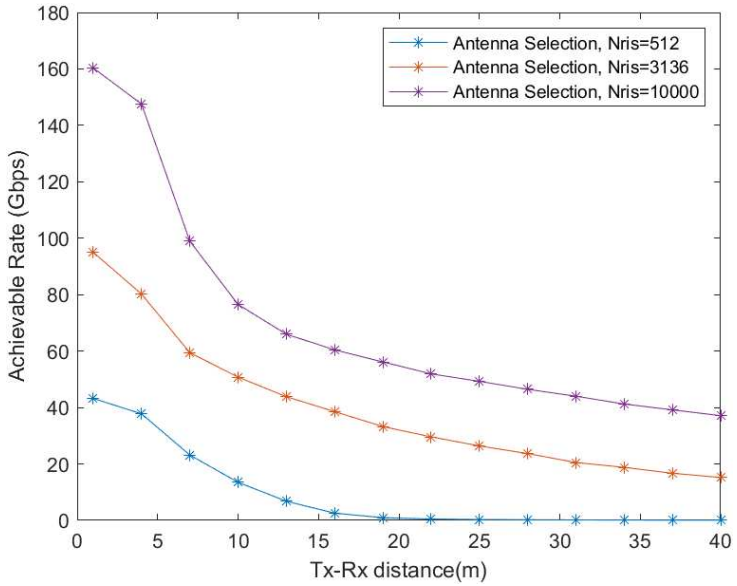

FIGURE D.5. Study of Achievable rate (Gbps) using antenna selection partially connected, for different RIS elements whilst increasing the distance between Tx and Rx.